EXPERIMENTAL STUDY OF DEGRADABLE FIBERS AS A PROPPANT

TRANSPORT AGENT

A Dissertation

by

JUNG YONG KIM

Submitted to the Office of Graduate and Professional Studies of
Texas A&M University
in partial fulfillment of the requirements for the degree of

DOCTOR OF PHILOSOPHY

Chair of Committee,	Nobuo Morita
Committee Members,	Zhengdong Cheng
	Alfred Daniel Hill
	Kan Wu
Head of Department,	Jeff Spath

May 2021

Major Subject: Petroleum Engineering

ABSTRACT

Hydraulic fracturing with slickwater is a common practice in developing unconventional resources in North America. The proppant placement in the fractures largely determine the productivity of the well as it affects the conductivity of fractures. Despite the wide use of the slickwater fracturing and the importance of the proppant placement, the proppant transport is still not fully understood and the efficiency of the proppant placement is mostly bound to the changes to proppant properties, friction reducers, and guar technology. The trend is that the industry will continue using a large amount of proppants per fracture operation as long as the transport mechanics is not fully understood, which is the motivation for pursuing research related to the proppant transport.

Although the degradable fiber is currently used in some cases to enhance the proppant transport, it has not been well investigated in a large-scale experimental set up. In this experimental study, we constructed three types of proppant transport slot equipment to conduct proppant transport experiment using different fluid composition of fiber and guar gum to test the proppant transport in the presence of fibers. Specifically, the proppant fall behavior and the horizontal transport behavior are studied. The experiments showed the distinct difference in transport mechanism in presence of fiber. The results indicate that the use of degradable fibers with or without the guar gum as viscosifiers can produce fracture slurry applicable in helping proppant placement in the reservoir for conventional and unconventional reservoir.

Lastly, the fracture simulation study is performed with a 3D hydraulic fracture commercial software, StimPlan™ by NSI Technologies. The simulation study focuses on the effect of fiber on fracture geometry and the proppant transport using fibers. The simulation is carried out with the experimental data on the degradable fiber that is used for the experiment. The numerical simulation study shows that the inclusion of fiber would yield different result compared to the base fracture fluids commonly used for the slickwater fracturing.

DEDICATION

This dissertation is dedicated to my wife and my daughter who have shown unconditional love.

ACKNOWLEDGEMENTS

CONTRIBUTORS AND FUNDING SOURCES

Contributors

This work was supported by a dissertation committee consisting of Professor Nobuo Morita from Petroleum Engineering Department, Dr. Daniel Hill and Dr. Kan Wu from Petroleum Engineering Department, and Dr. Zhengdong Cheng from Chemical Engineering Department. Experimental work for the dissertation was completed in collaboration with Tan Nhat Tran.

All work for the dissertation was completed independently by the student.

Part of the work are published in 2018 (Tan), and 2019 (Kim et al) in articles listed in reference.

Funding Sources

n' Flow behavior index

μ Viscosity

$\dot{\gamma}$ Shear rate

K Flow consistency index

$f(V_{prop})$ Function related to the amount of proppant in the slurry

V_f Local fracture volume (fracture width times fracture face area)

q_x, q_z Clear fluid and proppant volumetric flow rate through horizontal

length(x) and vertical length(z)

q_p Pump rate at the fracture face

q_l Clear fluid loss rate at the fracture face

C_D Drag coefficient

ρ_l Fluid density

v_r Relative velocity between the fluid and particle

A_p Frontal Area of the particle

α_p Proppant volume fraction

v_t Terminal settling velocity, m/s

g Acceleration of gravity, 9.81 m/s

ρ_p Proppant density, kg/m

μ_a Apparent viscosity, Pa·s

d_p Particle diameter, m

N_{Re}	Reynolds number
ρ_f	Fluid density, kg/m
D	Distance sand bed extends from wellbore, ft
Q	Injection rate, bpm
W	Fracture width, in
v_g	Sand Settling rate, ft/min

TABLE OF CONTENTS

LIST OF FIGURES

LIST OF TABLES

CHAPTER I

INTRODUCTION

Since the introduction of the hydraulic fracturing technology, using gasoline-based napalm gel, by J.B. Clark in 1948, the technique has improved extensively over the last several decades. The development in this technology coupled with the horizontal drilling unlocked the hydrocarbon production potentials from the shale source rock which were thought to be uneconomical. According to Energy Information Administration (EIA), the hydrocarbon production from the hydraulically fractured horizontal wells account for the most of the new oil and gas wells, that is, about 69 % of the total oil and gas wells drilled in 2016 (EIA, 2020) in the United States.

Unlike the conventional oil & gas well development where the target is the reservoir rock which stores the hydrocarbon that migrated from the source rock, the hydrocarbon production comes directly from the source rock in the case of the unconventional oil & gas wells that implement hydraulic fracturing technology.

Fracturing fluid plays a vital role in hydraulic fracturing treatment because it creates desired fracture geometry and controls the efficiencies of carrying proppant. Patel (Patel et al. 2014) provided a comprehensive analysis of hydraulic fracturing fluid systems and proppant trends across major shale plays in the United States between 2011 and the first half of 2013. Al-Muntasheri (Al-Muntasheri 2014) presented a review of the available water-based fracturing fluids over the last ten years for hydraulic fracturing reservoirs with low permeability. Safari (Safari et al. 2017) also presented a review of fracturing fluid systems used for hydraulic fracturing. In recent years, service companies often use a low viscous, fiber-laden fracturing fluid. The added fibers not only assist in the transport of proppant but also prevent proppant settling during fracture closure.

Fluid viscosity is particularly important because it not only provides resistance to gravitational settling, and help transport the proppant through the fracture, but also affects fracture geometry. Usually, viscous hydraulic fracturing fluids are required to have better proppant transport characteristics. This is accomplished by including polymers, typically guar or guar derivative, into the fracturing fluid to increase the viscosity. However, the proppant-carrying capability of the fracturing fluids is still a subject of debate among industry experts (Barati et al. 2014). The viscosity should be controlled in a range suitable for the treatment.

The proppant placement in the fractures largely determines the productivity of the well as it affects the conductivity of fractures. The purpose of proppant is to keep the fracture's surfaces open after pumping operation stops. Proppant transport is a very complicated multi-physics process, where the effective transport of proppant in fractures has a dominant effect on well productivity. Several simulation studies have been conducted to investigate the proppant transport with fluid flow in the hydraulic fracture (Blyton et al. 2018; Wu et al. 2014). The mechanism of proppant transport is different in slickwater fracturing in shale reservoirs (Mack et al. 2014), since slickwater does not have high viscosity to keep the proppant in suspension. It has been reported that fibers can enhance proppant transport while reducing the amount of polymer required for the fracturing fluid. Degradable fibers are considered for proppant transport, proppant suspension, and proppant placement in fiber-based hydraulic fracturing.

Fiber materials have been used in a variety of applications in drilling and completion fluids during the past few decades. One of the earliest uses during stimulation appears to be controlling proppant flowback, which relies on fiber reinforcement to increase the resistance of the pack to flowback during production of oil and gas (Card, R. J. et al. 1995). In recent years, fibers have been used to support proppant transport in hydraulic fracturing (Bivins et al. 2005). Collins

(Collins et al. 2018) studied the effect of degradable fiber composition and shape on proppant suspension, where the ability of degradable fibers to reduce the settling rate of ceramic proppant in a guar-based solution was studied as a function of fiber composition and shape.

Channel fracturing is an effective proppant delivery method, where the channel fracturing with degradable fibers has been proven to provide much higher conductive fracture networks by placing proppant islands inside fracture packs. Medvedev (Medvedev et al. 2013) gave a broad introduction on the mechanisms of channel fracturing, where they investigated channel fracturing and found that the fiber reduces proppant use significantly. Johnson (Johnson et al. 2011) summarized a comprehensive field study of channel fracturing in an ultra-low permeability tight gas formation, where the results indicate that channel fracturing technique increase gas production.

In this study, two different fibers, PGA (Polyglycolic Acid) and PLA (Polylactic Acid) were tested as proppant transport agent. The fundamental properties of PGA and PLA materials, such as melting temperature, glass-transition temperature, thermal-expansion coefficient, thermal conductivity, and strength, were introduced in detail by Yoshimura (Yoshimura et al. 2015). There is no literature on the use of PGA fibers in slickwater frac operation in the past explicitly mentioning on the composition or the concentration of the fibers used. The purpose of this work is to investigate the proppant transport mechanism in fiber-laden fluid with the use of two different degradable fibers.

CHAPTER II

LITERATURE REVIEW ON PROPPANT TRANSPORT AND FIBERS

This chapter contains three subsections that can help to understand the research work presented throughout the dissertation.

Proppant Selection and Transport Mechanisms

Proppant selection

The proppant selection in hydraulic fracturing application mainly considers three aspects: (1) density of the proppant for the transport ability, (2) strength of the proppant for the closure stress and the proppant pack conductivity, (3) and the proppant availability to the wellsite in masses in a competitive price (Cary, 2018). With the above consideration, appropriate proppant type, mesh size, shape, density and amount are chosen for the hydraulic fracture operation.

Based on the above considerations, type, shape, and the size of the proppant is chosen. There are mainly three types of proppants; uncoated sand, resin coated sand and ceramics as shown in **Fig. 1** (Gallagher, 2011).
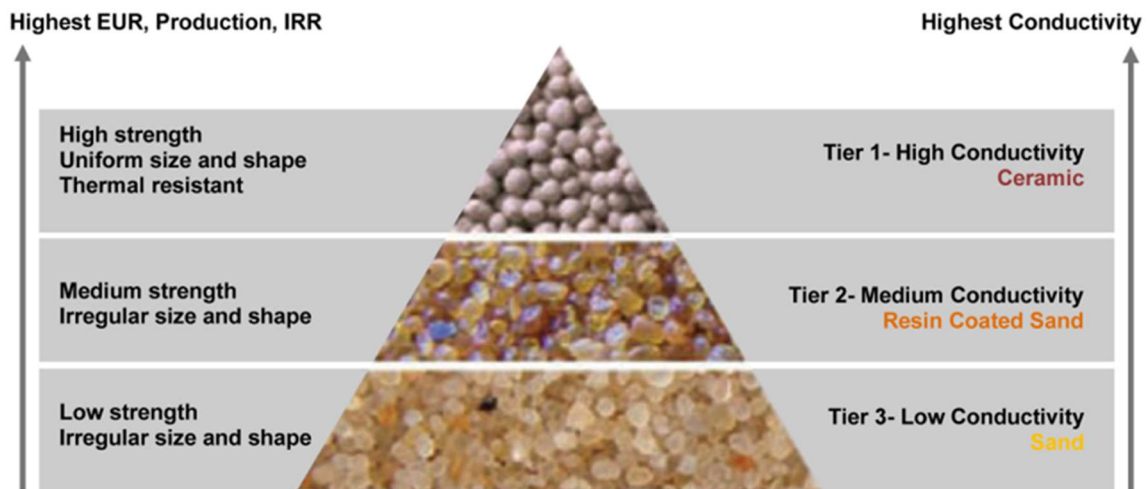
Figure 1. The proppant type hierarchy showing the conductivity and strength relationship. Reprinted from Gallagher, 2011.

Fig. 1 shows that ceramic proppant has the highest strength and the highest conductivity. Usually, the ceramic proppants are used in deeper reservoirs with high closure stresses. The ceramic proppants are manufactured and have higher sphericity, roundness, size uniformity, and strength compared to the other proppants. Depending on the alumina contents in the ceramic proppant, the density, and its performance differs for the ceramic proppants (Palisch, et al. 2015).

As more proppants are used per fracture operation, economic consideration has become the main factor in proppant selection in the North America. The cost of using locally sourced sand can be 10 times cheaper than using premium proppants. In many instances, the advantages of using premium proppants, such as low density and ability to withstand higher closure stress for a longer period of time, do not outweigh the cost benefits of using locally sourced sands leading to less use of ceramic proppants and resin coated sands (Liang et al. 2015).

Transport Mechanisms

Understanding the proppant transport mechanisms is essential for a successful hydraulic fracture design, and the productivity of the reservoir. The proppant transport is mainly defined by four main mechanisms: rolling, suspension, saltation, and settling (Alotaibi 2015).

The rolling or gliding occurs when the hydrodynamic force is greater than the frictional force holding the proppant in place. Once the proppant gains momentum, it moves in direction of the fluid flow. Unless the lifting force is greater than the gravitational force of the proppant particle, the proppant continues to travel by rolling or sliding until the fluid force is less than the drag force opposing the proppant movement. The rolling and gliding mechanism affects the proppant travel distance the least out of four transport mechanisms (Dey 1999). The rolling and gliding mechanism along with saltation only occurs on the topmost layer of the proppant dune.

5

The proppant saltation follows the rolling and gliding when the lift force from the fluid exceeds the frictional drag force and gravitational force on the proppant. The proppant grain would first be lifted, and travel in suspense until the gravity exceed the force suspending the proppant (Southard, 2006).

The main proppant transport mechanism is suspension and settling. When the fracture fluid laden with proppant is pumped into the formation, the proppant travels through the fractured formation in suspension and then settles. The physical property of the fluid and the proppants largely determines the forces that affect the physical behavior of suspension and settling. The density difference between the fluid and the proppant along with the viscosity of the fluid and proppant diameter determines the terminal settling velocity of the proppant following the Stokes' law as shown in **Eq. 1** through **Eq. 3** below for the three different flow regions (Stokes, 1851; Novotny, 1977; Valko, 1997). The horizontal distance traveled by a proppant particle then determined by the velocity of the fluid coupled with the settling velocity of the proppant.

$$v_t = \frac{g(\rho_p - \rho_f)d_p^2}{18\mu_a}, \text{ for } N_{Re} \leq 2 \text{ (Stokes-law region)} \tag{1}$$

$$v_t = \frac{20.34(\rho_p - \rho_f)^{0.71}d_p^{1.14}}{\rho_f^{0.29}\mu_a^{0.43}}, \text{ for } 2 < N_{Re} \leq 500 \text{ (Intermediate region)} \tag{2}$$

$$v_t = 1.74\sqrt{\frac{g(\rho_p - \rho_f)d_p}{\rho_f}}, \text{ for } 2 < N_{Re} \leq 500 \text{ (Newton's-law region)} \tag{3}$$

The early experimental work in the proppant transport hydraulic fracture done by Kern et al. (1959) defines the equilibrium velocity, which defines the slurry velocity that corresponds to the equilibrium proppant bed height; stable proppant bed height. According to the experimental

work, the authors defined the equilibrium velocity which is a function of the sand and fluid

density, amount of sand injected per minutes and the fluid velocity. The local fluid flow rate

changes as the flow cross sectional area changes due to the height of the sand dune; sand

accumulation in fixed width leads to decrease in flow area leading to higher local fluid velocity.

Furthermore, the authors defined the extension of the settled proppant bed from the wellbore with

Eq. 4 (Kern et al. 1959) as shown below.

$$D = \frac{34}{W v_g} \qquad\qquad (4)$$

where D is a distance covered by sand dunes from the wellbore in feet, and Q is slurry injection

rate in barrels per minute, and W is the panel width in inch, and v_g is settling rate of the sand

particle in ft per minute. Although, the experiment was very primitive; using only sand and water

in a clear parallel plate cell, the study tells the main proppant transport mechanism in the slick

water fracturing operation.

In the low viscous fluid, proppants that are injected at the beginning of the treatment settle

near the wellbore and the proppants that are injected later settle further away from the wellbore

(Kern 1959). The injection sequence matters when multiple proppant sizes are used, and injection

of larger sized proppant is recommended.

For an accurate determination of the proppant transport mechanism, movement of the

proppant slurry with particle interactions needs to be considered along with the single particle

settlement, especially in highly viscous fluid. For this, density driven flow, particle velocity

profiles, resistance of the slurry flow and single particle hindered settlement need to be considered

when describing the proppant transport. The density driven flow and convection flow dominate the

proppant transport in highly viscous fluid, whereas the particle suspension and settlement are more important in non-viscous fluid (Barree and Conway 1995).

Fracturing Fluids on Proppant Transport

The main functions of the fracture fluids are to create desired fracture network covering the payzone and deliver proppants without damaging the target reservoir in environmentally conscience manner at the lowest cost available. Largely, there are 3 fracturing fluid system and combination of any three-fluid system used in hydraulic fracturing operation: slickwater, gel, foam, and hybrid.

The slickwater frac, also called water frac, is the most used fracturing fluid system for the shale and tight gas sand reservoir with low permeability. As the water frac became more popular, the total proppant mass used per year for the hydraulic fracturing increased by 40 folds over the last 15 years (Weijers, et al. 2019). The slickwater frac uses only water or very low concentration of linear gel and friction reducer such as polyacrylamide (Woodworth, 2007; Schein, 2005).

The main advantage of using low viscous slickwater fluid system is that there is a minimal damage to the reservoir compare to the crosslinked gel system (Palisch, 2010). This advantage is critical for the shale or tight gas reservoir as the gel damage can lead to blockage of already low permeable reservoir.

Another advantage of the slickwater frac is that it uses less chemicals leading to a possible cost saving, and less environmental concerns. The hydraulic fracturing operation uses a lot of water, and the water recycling and deposition of wastewater are a serious concern especially in the area where there is limited access to the water source (Palisch, 2010). By using less chemicals, the flow back water from the fracking operation can be treated and recycled.

Lastly, the use of high injection rate coupled with low viscous fluid may create more complex, longer fractures than a crosslinked gel system which is preferable for shale or tight gas reservoir. In shale or tight gas reservoir, the total stimulated reservoir volume directly affects the production; larger area of stimulated reservoir leads to a better production. While crosslinked gel system experiences a difficulty in limiting the fracture height growth to the target pay zone, the height control with slickwater frac is more manageable (Palisch, 2010).

The main disadvantage of using the slickwater frac is its inefficiency in proppant transport. Due to the density difference, gravitational force, and the lack of viscosity, proppants settle near the inlet unless the flow rate increases or the flow area decreases for the saltation and rolling to be effective (Woodworth, 2006) To offset this issue, large amount of water, proppant, and a bigger pump are used in the slickwater frac leading to additional cost (Alotaibi and Miskimins, 2015). Pumping more proppants to offset the early proppant settlement can lead to early screenout problems near the wellbore (Woodworth et al. 2007). It is also suggested that to account for the proppant settlement, fracture should be designed to place the payzone at the bottom of the fracture geometry (Cary, 2018).

Fig. 2 shows how proppants are transported within the fracture when the slickwater frac is used. The understanding of proppant dune development is important in slickwater frac. As it can be seen from **Fig. 2**, low viscosity, density difference between the proppant and fluid, and low fluid velocity leads to the settlement of proppants near the wellbore. According to Kern et al. (1959), the first injected sand settles to the bottom until a dune height is reached leading to a certain equilibrium fluid velocity. The proppant travels further as the fluid velocity increases extending the proppant dunes. The process continues until the establishment of the equilibrium dune height where the proppant does not roll or saltate anymore.
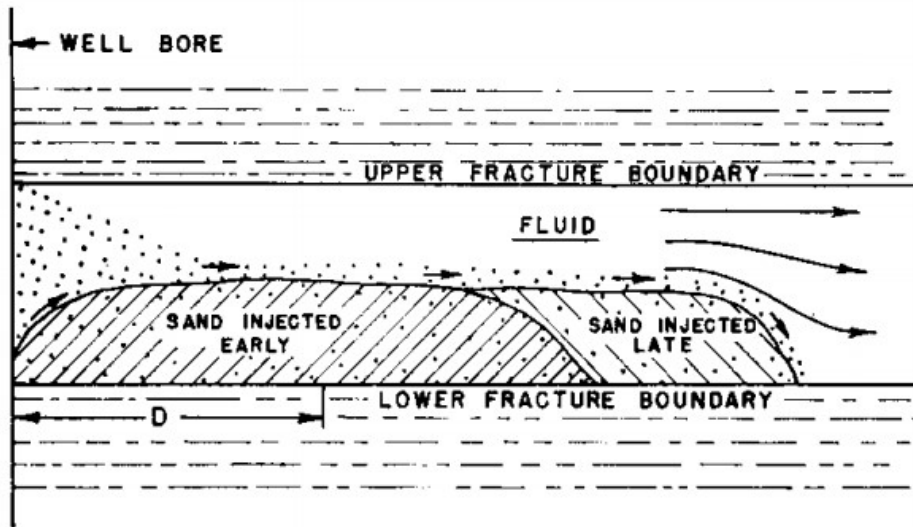
Figure 2. Proppant transport using slickwater frac system showing progressive dune formation near the wellbore to the fracture tip. Reprinted from Kern, 1959.

As the proppant rolls and saltates, they get sorted according to the size, density, and its shape: sphericity and angularity. According to Alotaibi and Miskimins (2015), the sorting of proppant is an important in design consideration as it directly affects the proppant conductivity. Using 40/70 mesh sand, their flow experimental study found the following: (1) The proppants settle as soon as the slurry flow decreases due to the increase in the cross-sectional flow area, (2) the grains get sorted according to the grain size in decreasing order from the top layer leading to the high to low conductivity layer from top to bottom layer, (3) the wall friction leads to increase in proppant settlement by decreasing the flow rate leading to increase in the dune height, and (4) the grains travel to the secondary and tertiary panel slots as the equilibrium dune level (EDL) develops in the primary fracture slot.
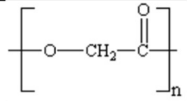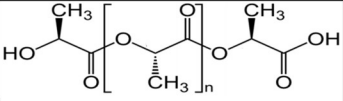
<center>**Review of Fibers Used in the Oilfield**</center>

PLA and PGA Fiber Application

Fibers have been used in different applications in the oilfield, such as in drilling as a lost

circulation material (LCM), cementing operation as strengthening material, and in hydraulic

fracturing operation. This sub chapter will review the fiber applications in the past, especially the

use of degradable fibers that are used for this research work.

The polyglycolic acid (PGA) and polylactic acid (PLA) are polymers that hydrolyze in the

water solution with the properties shown in **Table 1.** They have been used in many industries as

they can be manufactured as powder, granular, and fibrous materials in addition to their high

tensile strength and the degradability in water solution. The PGA is widely used as degradable

sutures in the medical applications, whereas the PLA is commonly used as degradable cups and tea

bags (Okura et al. 2015; Tan et al. 2017).

Table 1. Property of the PGA and PLA used for the experiment (modified from Yoshimura et al. 2015)

Property	PGA	PLA
Chemical Structure		
Density	1.5 ~ 1.6 g/cc	1.21 ~ 1.25 g/cc
Young's Modulus	7.0 GPa (1015 Kpsi)	2.5 GPA (360 Kpsi)
Tensile Strength	1534.1 MPa (222.5 Kpsi)	153.1 Mpa (22.2 Kpsi)
Max Elongation	2.10%	3 ~ 4 %
Melting Temperature	220°C (428°F)	180°C (356°F)
Glass Transition Temperature	40°C (104°F)	55 ~ 60° C (131 ~ 140°F)
Thermal Expansion Coefficient	$5.4 \times 10^{-5}\ K^{-1}$	$9.0 \times 10^{-5}\ K^{-1}$
Thermal Conductivity	$0.35\ W \cdot m^{-1} \cdot K^{-1}$	$0.04\ W \cdot m^{-1} \cdot K^{-1}$

The proppant flowback can be as large as 20% of the pumped proppant in some cases. The

advantage of the fiber application to strengthen the proppant pack comes from giving the

<center>11</center>

operational freedom; the reinforcement of the proppant pack comes from physical mechanism, not from chemical mechanism leading to rapid well turnaround (Card, et al. 1995). The field application done by Ramones, et al. (2015) states that the adhesive fiber can be used to mitigate the proppant flowback problem. In the Oriente basin located in Amazon region of the Ecuador, operators used hydraulic fracturing to remove near wellbore formation damage with gel-based fracturing fluid. In large, the hydraulic fracturing proved to be successful by increasing the productivity of the wells, however maintaining proppant packs in the fracture had been a big issue. Due to the proppant flowback, proppant pack is compromised leading to reduced fracture conductivity. The research team found that implementing their Fiber Based Proppant Flowback Control (FBPFC) method that uses adhesive fiber worked to maintain a better proppant pack in place and reduce the proppant flowback problem leading to forecasted saving of $500,000 USD per well.

According to Sitdikov, et al. (2009), degradable fibers used in hydraulic fracturing helped in proppant transport and ease the early proppant screenout problems. Another advantage of using the degradable fibers is found in controlling the fracture geometries. Many wells that needed hydraulic fracturing stimulation in the Siberian oilfield had water bearing layer that required a well strengthening treatment with Height Growth Control (HGC) material to prevent fracture geometry from break into the water bearing layer. Another solution was to reduce the fracturing treatment size or reduce the treatment pressure by reducing the apparent viscosity of the fracturing fluid to prevent the breakage into water bearing layer. These solutions were either very costly or insufficient to stimulate the reservoir. The authors tested and verified that using low apparent viscosity fracturing fluids with degradable fibers successfully increased the propped fracture half-length up to 15% while reducing the fracture height up to 30%.

Degradable PLA fiber's ability to suspend the ceramic proppants in guar-based solution is studied by Collins, et al. (2018) by comparing it to various cellulose ester fibers. The authors specifically investigated the cross-sectional shape of PLA fiber to the suspension capability and concluded the following: (1) more fiber helps in proppant suspension regardless of the fiber's shape or type, (2) smaller fiber diameter reduces proppant settlement, (3) fiber's that are crimped helps in proppant suspension, and (4) proppant suspension can be helped by choosing fiber with trilobal cross-section when compared to the octagonal and x shaped cross-section. In this research, the authors focus only on proppant suspension in the absence of fluid flow.

The use of short fibers in seven test wells in the Lost Hills field, California showed that fibers can be used with low viscous fracturing fluid to successfully contain the geometry to the desired height and width while transporting the proppants. The diatomite formation in the study area is characterized as low permeability, high porosity oil reservoir with low Young's modulus and only few barriers that could contain the fracture growth. And the goal was to minimize the fracture height to the target payzone while reducing the fracture width for longer fracture length. The use of tiltmeter surveys showed that the test wells with fibers had increased fracture length. The early production comparison also showed that the wells that were treated with fibers showed increased production per proppants pumped.

The PLA and PGA fibers are tested for its hydrolysis rate and the application as a fluid loss controlling material (Yoshimura, et al. 2015). The study found temperature dependent hydrolysis rates and concluded that the PLA and PGA fibers can replace silica flour as an effective fluid loss controlling material. The advantage of using these fibers over the conventional silica flour comes from their degradability in the water solution; both PLA and PGA fiber fully degrade by hydrolysis

in the water solution within 24 hours when the fluid is heated. The authors also state that PGA hydrolyze quicker than the PLA as a fluid loss control agent.

The field study done by Engels, et al. (2004) discuss about the benefit of using fibers for hydraulic fracturing operation by keeping the fluid viscosity low compare to the crosslinked polymer fluids. The inclusion of fibers in the fluid enabled the use of the fracture fluid with 6 to 8 times lower viscosity when compared to the crosslinked polymer fluids without compromising the suspension ability of the fluids. From the field study of over 7 wells using the fiber technology, following conclusions were made: (1) there is a significant influence on the relationship between the fracture width and fluid viscosity on the proppant placement when fiber is used leading to the recommendation on keeping the fluid viscosity between 50 to 150 cp in tight rock formation, such as the East Texas Cotton Valley Sand Formation, (2) the proppant pack conductivity increased by 11% while keeping the polymer concentration to one-half when fiber is used compared to the conventional polymer laden slurry, (3) the fracture height confinement is observed with the tracer log data when fiber-laden fluids is used while maintaining the proppant transport, and (3) the early production data indicates increase in the gas production on 5 wells that are treated with fiber-laden slurry compared to the conventional crosslinked fluid and slickwater fluid without fiber.

The PGA has been widely used as a degradable material in multi-stage hydraulic fracturing operation. There are several advantages of using PGA as a frac ball and frac plug in plug-and-perf operation: (1) Unlike typical frac plugs, the milling out with coil tubing operation can be skipped, leading to cost saving and risk mitigation from avoiding the milling operation, (2) Unlike typical degradable materials requiring acids or salts for degradation process, the PGA frac ball degrades through hydrolysis with only water at the typical shale reservoir temperatures, (3) PGA and PLA

both has high tensile strength which is required in tools used in hydraulic fracture (Takahashi et al. 2015; Okura et al. 2015).

The PGA polymer is tested in drilling operation as an effective lost circulation materials (LCM) in a form of powder. According to Hodge et al. 1995, the PGA powder acted as an effective LCM without affecting the hydrocarbon production due to its hydrolysis after preventing the leak off of drilling fluids in the presence of natural fractures. The research conducted by Matsui et al. 2012 compared the PLA and PGA fibers as LCM materials. They concluded that the PGA can be used as an effective LCM material whereas the PLA is not suitable to be used as LCM as it loses the sealing capability by softening with temperature.

CHAPTER III

EXPERIMENTAL SETUP AND PROCEDURE

In this chapter, the experimental setup and procedures are described in detail. The chapter is largely divided into two sub-chapters, small-scale and large-scale setups. In each chapter, different apparatus, and chemicals used are discussed. Figures, tables and flowcharts are used to better illustrate the experimental setup and procedures.

Small scale static proppant fall test equipment

Two types of small-scale apparatus are prepared to observe the proppant settlement as shown in **Fig. 3**. The apparatus on the left is a graduated cylinder with the dimension of 2 feet in length and 4-inch in diameter, made out of glass. The rectangular panel on the right has dimension of one foot by 4 feet in width and length, and varying inner thickness ranging from 0.1 to 0.5 inches. The rectangular panel is constructed from Plexiglas sheets.
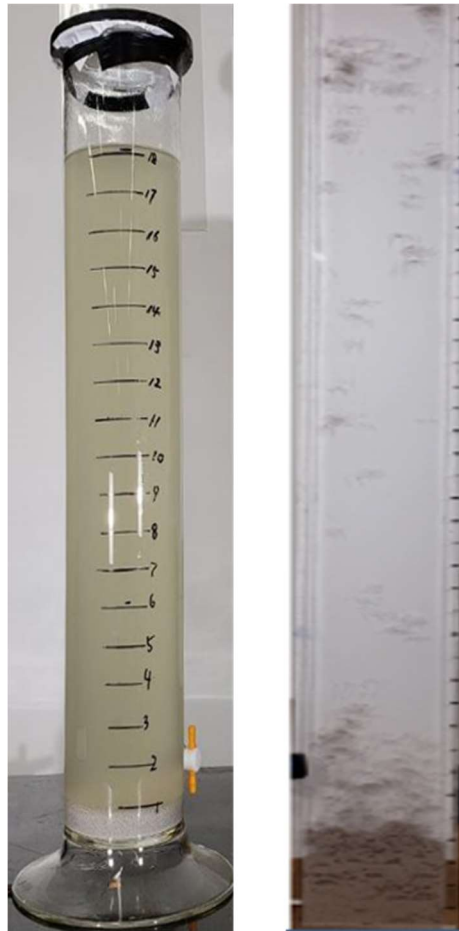
Figure 3. Small scale experimental setup. Cylinder on left and rectangular panel on right.

The cylinder is used to observe proppant settlement without the wall effect. The test fluids are mixed in the cylinder by shaking vigorously in the horizontal position for several minutes until the fluids are all intermingled. Then the proppant precipitation is recorded for ten minutes for the interpretation.

For the rectangular static fall test apparatus, it is flipped upside down for the intermingled test fluid to settle for ten minutes. Then the precipitation of the settled proppants is recorded after flipping the apparatus. The recording is done for ten minutes to interpret the results.

Large scale dynamic proppant transport equipment and procedure

Large scale proppant transport equipment design and setup

The large scale frac slot equipment was constructed with Tan Tran, a former graduate student who worked on the thesis titled "Effect of Scale in Proppant Transport Experiment Using PGA" (Tran, 2018). Therefore, the description of this section is partially duplicating his thesis. The large scale experimental set up is fabricated with the following objectives: (1) ability to handle the hydraulic head pressure of the fluid column and the pressure from the fluid, (2) ability to vary the panel widths to study the relationship between the fracture width and proppant distribution. **Table 2** shows the dimension of the large-scale fracture slot equipment.

Table 2. Dimensions of the large-scale fracture slot equipment

Outer dimension	4' x 16' x 4.5"
Channel Width	0.1" - 0.5"
Inlet Numbers	5
Outlet Numbers	5
Material	Acrylic, Polycarbonate

The panel width, where the fluid flows, can be modified to accommodate between 0.1 to 0.5 inches width. However, the outer width is 4.5 inches due to the high pressure the apparatus needs to withstand, and the high fluid velocity; the outer layers are 2 inches thick on both front and back side. The inner layer, where the fluid travels, is made of polycarbonate material to maintain the panel's clarity from multiple experiment as the fracture fluid is abrasive due to the proppants. The total thickness of inner shell is 1 inch thick with 0.25" polycarbonate and 0.75" acrylic. Other drawings and specifications are presented in the **Appendix A.**
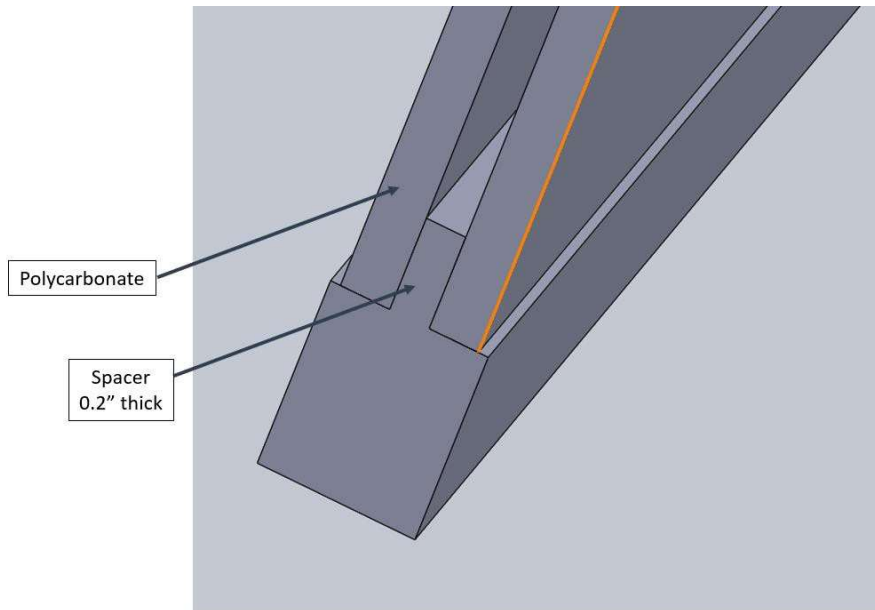
Figure 4. Replaceable Inner spacer to fix the width of the apparatus

The replaceable inner spacers are designed to vary the width as shown in **Fig. 4**. For example, if the test needs to accommodate 0.4" width, the replaceable inner spacers are manufactured to accommodate 0.4" width. To accommodate the width variation, the modular design is chosen. As it can be seen from **Fig. 5**, the gap due to the variation of the width is filled with clear acrylic spacers of varying thickness so that the inner panels would have 2.5" thickness at all time without any gaps between them.
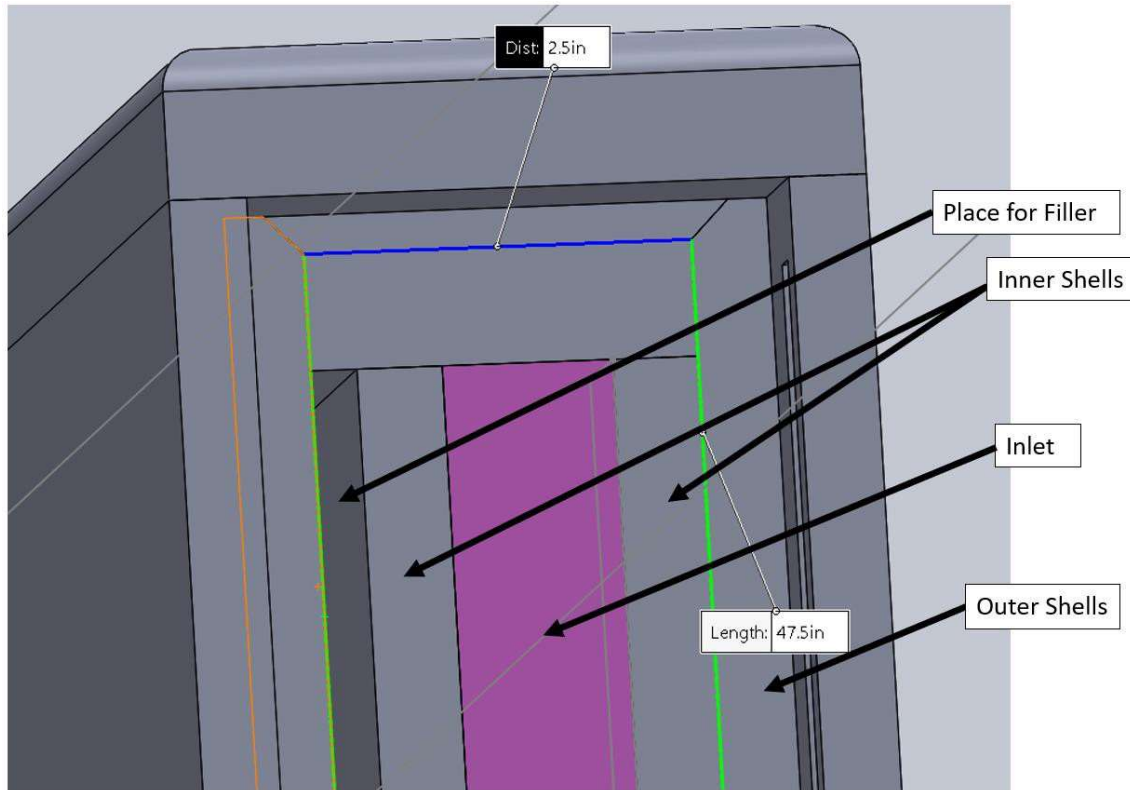
Figure 5. The inner shells with multiple panels to keep the width at 2.5 inch at all time.

The outer shells are designed and manufactured to enclose the inner shell. The outer shell is

1" thick on each side, bringing the total thickness to 4.5 inches. After the clear acrylic panels are

designed, based on the mechanist suggestion, L beams and rectangular steel beams are chosen to

support the large load as shown in **Fig. 6** and **Fig. 7.** The L beam is used to cover and enclose the

entire acrylic panel, while 17 steel beams with bolts on the top and bottom of the rectangular beam

pressurize and hold the modular panels in place. The design is completed in Solidwork and the

assembly is shown as shown in **Fig. 8**.
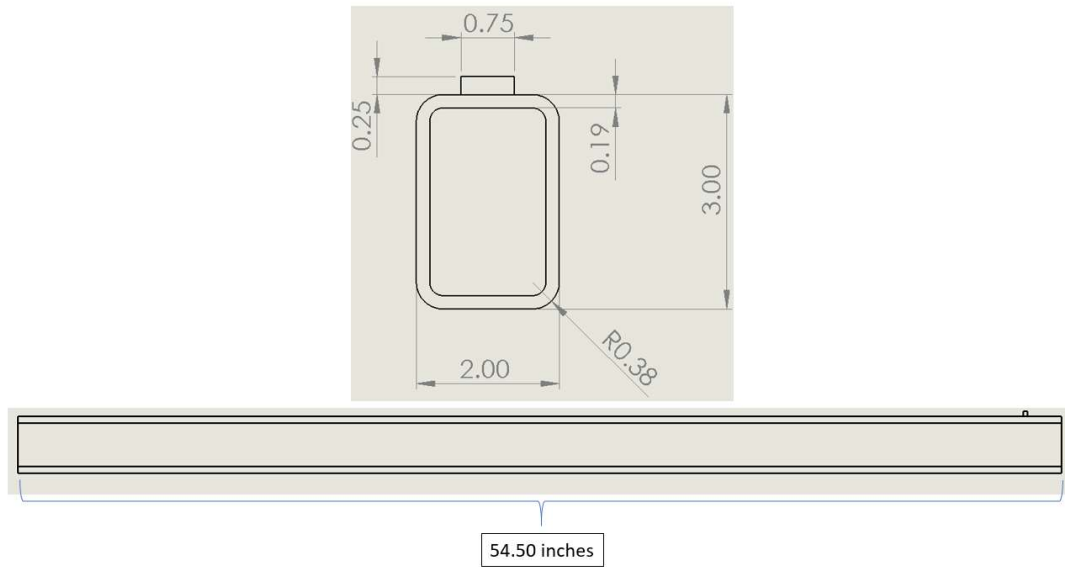
Figure 6. The rectangular steel bar used to provide the closure force for the acrylic panels.
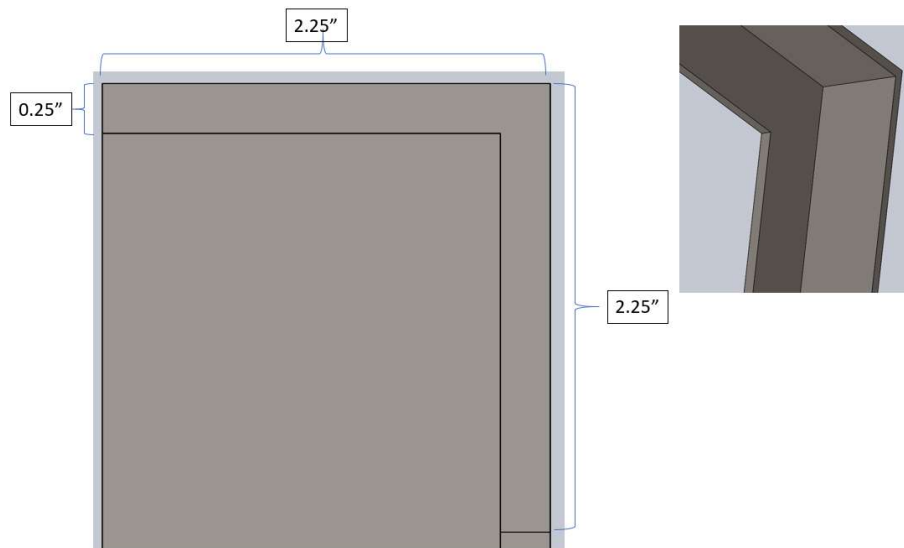
Figure 7. Dimension of the L Beam Frame to enclose the acrylic panel.

Figure 8. Large apparatus assembly with crane to hold the frame upright.

Fig. 9 shows the inlet side of the large-scale apparatus. The inlet has five pipes that branch off from one vertical flow line that is connected to the mixing tank with a pump. The pipes are connected with valves which can be used to restrict the flow or to choose the number of open inlets from 1 to 5. The flow inlet diameter is 0.5" although the panel width limits the effective size of the fluid flow area. One pressure sensor and the pressure relief valve are installed at the bottom of the panel. One valve is installed at the top of the panel to safely relieve the pressure and bleed the air from the panel.

Figure 9. Inlet pipe setup showing five inlets with valves, pressure sensor on bottom and fluid bleeding valve at the top.

The outlet side is equipped with 5 independent outlets with valves, as shown in **Fig. 10.** One relief valve with pressure sensor is located on the bottom, and one bleed valve is located on the top. Unlike the inlet valves that branch off from one vertical pipe, the outlet valves are all individually connected to the panel to prevent the pressure buildup inside the apparatus as quick as possible. As it can be seen from **Fig. 10**, each outlet is connected to the tube which acts as a conduit for the fluid to flow to the container that catches the proppants. During the experiment, valves are controlled so the pressure reading from the bottom of the outlet does not spike up. The relief valve on the top is used to bleed out any air that are trapped in the panel before the experiment begins.
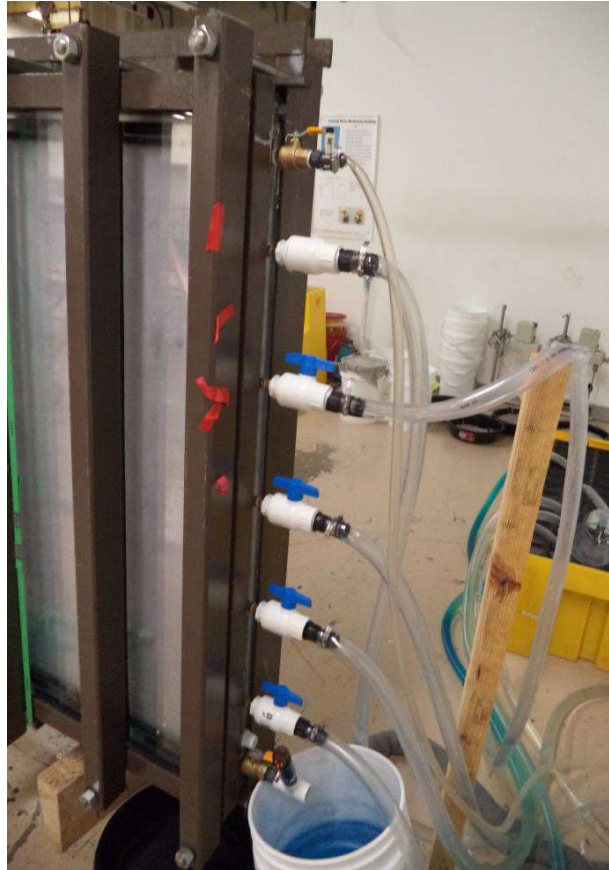
Figure 10. The Outlet Side of the Panel shows 5 flow outlets with valves, one pressure sensor on bottom, and one bleed valve on top with the proppant catcher shown in the right.

The pump is selected as shown in **Fig. 11**. It is ¾ horsepower AC electric pump that can pump the fluid at the maximum rate of 21 gallons per minutes with 1725 maximum motor RPM. This pump is chosen so that the experiment can be carried out at 20 gallons per minute pump rate and handle the hydrostatic head pressures, and the back pressures without any trouble. The pump can pump fluid with up to 10 % solid and the pump rate can be controlled with a VFD (Variable Frequency Drive). The VFD is used to control the flow rate in our experiment as shown in **Fig 12.**

Figure 11. WEB brand general motor with ¾ hp that can pump at 21 gpm with 10 % solid contents

Figure 12. The variable frequency drive used to control the flow rate of the pump

Fig. 13 shows the flow meter, model SA6010 from ifm efector, used to monitor and record the fluid flow during the experiment. We choose the flow meter that can measure the flow rate with solid contents as the proppants can interfere with the accurate reading. Also, the meter needed to

record the reading for the later time interpretation. The reading in real-time is displayed on the meter for tracking and keeping a constant flow rate during the experiment with the VFD.

Figure 13. Flow meter to measure the flow rate in real-time and post experiment.

Fig. 14 shows the pressure sensor, model PN2697 from ifm efector, used to monitor and record the pressure during the experiment. This pressure sensor can also make accurate reading with the solid contents, ranging from 0 to 14.5 psi in 0.02 psi increment. Also, the meter records the reading for the later time interpretation. Two pressure sensors located at the bottom of the inlet panel and the bottom of the outlet panel are used to closely monitor and control the pressure buildup inside the panel to prevent any damage to the apparatus. We choose the flow meter that can measure the flow rate with solid contents as the proppants can interfere with the accurate reading. Also, the meter needed to record the reading for the later time interpretation. The reading in real-time is displayed on the meter for tracking and keeping a constant flow rate during the experiment with the VFD.

Figure 14. PN2697 Flow Sensor

Fig. 15 shows the mixing tank, 110-gallon capacity, on the custom-made frame with pump motor, VFD, and diverting pipe. The cone-shaped bottom tank is chosen so the apparatus can be easily drained and cleaned after each experiment. The flow diverting line is connected right after the flow outlet from the pump and right before the flow meter. This line serves to better mix the fluid and divert the flow when it is necessary to adjust the flow rate in conjunction with VFD. It should be also noted that the frame is equipped with wheels for mobility.

Figure 15. The custom-made frame that hold 110-gallon mixing tank, flow pump, VFD, flow sensor, and flow diverting line on the wheels.

Fig. 16 shows mixing motor with propeller to agitate the fluid mixture while the experiment is run. Two propellers are installed at the bottom of the long shaft so that it can keep a homogeneous fluid mixture throughout the experiment.

Figure 16. Mixing motor with two propellers installed on bottom to agitate fluids.

Fig. 17 shows the mixer, CARFRAMO RZR50, used to mix the test fluids. Due to the tendency of the guar to make fisheye clumps as it is mixed in water, the guar mixture is mixed with mixer in small batches.

Figure 17. CARFRAMO RZR50 Fluid Mixer used to mix the guar with water.

Fig. 18 is used to measure the viscosity of the fluids. As the fluids are prepared, we evaluated how would fiber effect on the viscosity, which is an important parameter in hydraulic fracturing operation.

Figure 18. FANN Viscometer used to measure viscosity of the test fluids.

Fig. 19 shows the data acquisition module, DATAQ model DI 1120, used to record the pressure and the flow rate during the experiment. Since two pressures and one flow rate data are recorded, three channels are used to log the experimental data. Channel 1 is used for the flow rate, and Channel 2 and 3 are used for inlet and outlet pressure recording.
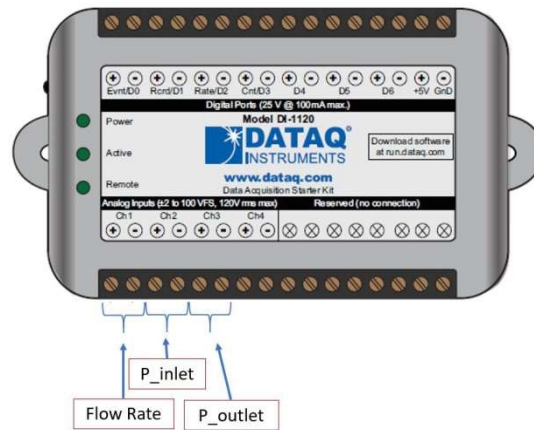
Figure 19. Data acquisition module used to record flow rate, and two pressure data.

Experimental Fluid Sample Composite

For the experiment, guar gum, proppant, PGA and PLA fiber, and tap water are used. **Fig. 20** shows the guar gum used for the experiment. The guar gum is purchased from ingredi.com in bulk, and stored to prevent moistures affecting the guar.

Figure 20. Guar gum used for experiment.

Fig. 21 shows the proppants used for the experiment. Instead of using the local sands, the experiments are carried out with ceramic proppants provided by CARBO. The mesh sizes used for the experiment are 20/40, 30/50, and 40/70.

Figure 21. The 20/40 mesh ceramic proppant with 2.69 g/cc density used for experiment.

Fig. 22 shows the fibers provided by the sponsor company. Both PGA and PLA fibers are used in the experiments.

Figure 22. The fibers used for experiment (PGA fiber on left and PLA fiber on right).

Large Scale Fluid Mixing Procedure

Fig. 23 shows the schematic diagram of the large-scale experimental setup. Except the guar gum that is mixed with the mixer in small batch to prevent fisheyes, the fibers are mixed within the mixing tank prior to each experiment. Since the fibers used for experiment can tangle up, and the bubbles can be trapped while mixing the fluids, it was crucial not to have the agitator motor for too long prior to conducting the experiment.
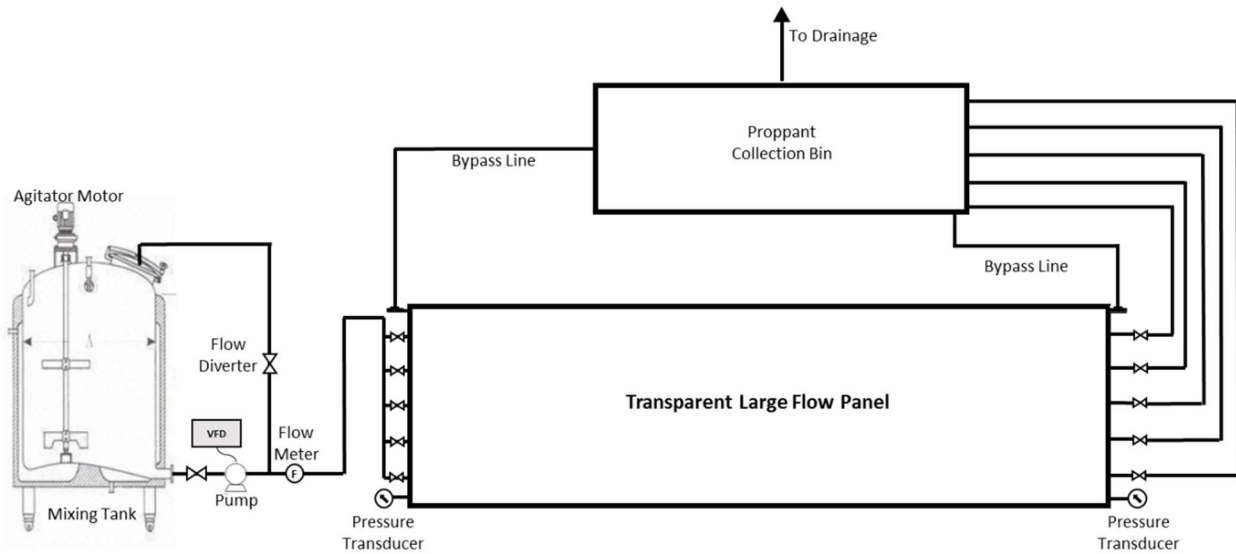
Figure 23 Schematic diagram showing the large-scale experimental setup.

Table. 3 shows the fracturing fluid composition used for 60 gallons of water. The composition is based on limited amount of proppant, approximately 50 lbs of proppants were available. As mentioned, the guar gum is not added directly to the mixing tank as it can form fish-eye lumps. Thus, the guar gums are gradually mixed in small quantity using a small spoon using the fluid mixer.

Table 3. Fracturing Fluid Composition used for 60 Gallons.

Fluid	60 gal (227.13 L)
Proppant	49.56 lbm (22,480.04 g)
PGA fiber	0 - 0.300 lbm (0 - 136 g)
Guar	0 - 0.300 lbm (136 g)

The viscosity measurement procedures

The test to measure the viscosity is done by taking the sample fluid out of the mixing tank right before carrying out the experiment. Two sample fluids are taken out of the mixing tank before adding fibers and after adding fibers. The viscosities are measured using the FANN rheometer as shown in **Fig. 18**.

Large panel fill up procedure

Before the proppant laden fluids are pumped, the panel is filled with the fluid sample without the proppants. This is done slowly by filling up the panel while bleeding the air from the bleeding valves located at the top of inlet and outlet. Extra caution is taken as the pressure can build up rapidly leading panel to rupture.
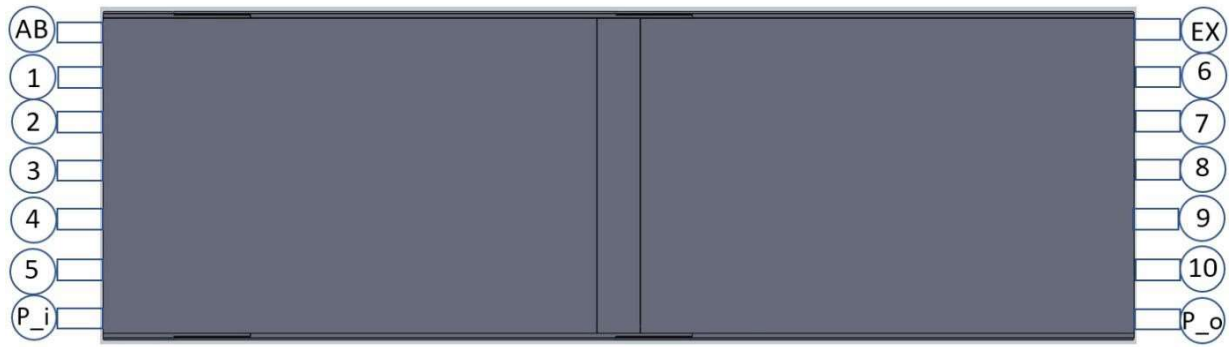
- 1 – 5: Inlet Valves
- 6 – 10: Outlet Valves
- AB: Air Bleeding Valve
- EX: Extra Valve, No Significant Usage
- P_i: Inlet Side Pressure Sensor and Pressure Relief Valve
- P_o: Outlet Side Pressure Sensor

Figure 24. Large panel showing the location of valves and sensors.

Fig. 24 shows the large panel with the sensors and valves. The panel is filled with the test fluids without proppant using the inlets 1 to 5. As the panel is filled, the outlet valves from 6 to 10 are closed consecutively; as the water is filled up, valve 10 is closed first, and this continued up to the valve 6. During the fill up process, the pressure is monitored from the inlet side of the pressure valve, and the pump flow rate is kept below 5 gpm. The extra valve is closed during this process, and the air that is trapped in the panel is bleed out with the air bleeding valve located on the inlet side of the panel. Once the panel is filled with no visible air, all the outlet valves and air bleeding valve are closed. The pressure is monitored until the proppant laden slurry is pumped to make sure the fluid does not leak from the panel from any valves.

Slurry Pumping Procedure

After the panel is filled, proppants are added to the mixing tank. Using the agitator motor, the proppant is mixed well before the slurry is pumped into the panel. As the pump is

ramped up to pump at 20 gpm, the valve 6 to 10 are open to maintain constant pressure. This process needs to be done, just with any other process mentioned above, by at least two people. One person needs to adjust the flow while the other person controls the outlet flow valves to maintain the appropriate pressure; pressure not exceeding 10 psig.

Cleaning Procedure

The large-scale experimental panel is cleaned after each experiment. Due to the size of the experimental apparatus, it would have taken too much time to disassemble and clean parts after each experiment, thus relatively quick method to clean out the panel is employed. The panel is first drained while the water is being flown from the inlet. Continuously flowing the fluids lead to removal of most of the proppants and fibers as the fluid would wash them out to the outlet and to the proppant collection bins. Although majority of the proppants and fibers are drained, there are some fibers and proppants that need to be manually removed. This is done by using a thin steel wire. The steel wire is used while fluids are being run to disturb the proppants and fibers that are stuck in the panel through the outlet and inlet valves. By following the above steps, the panel is cleaned after each experiment.

CHAPTER IV

SMALL SCALE AND LARGE-SCALE EXPERIMENTAL RESULTS

Small scale Test Results

Static fall rate tests (using 4-inch cylindrical container)

Static settlement tests were performed to measure the free settling velocities of proppant with 0.1 m-ID cylindrical containers. This experiment is intended to measure the proppant free fall rate without the wall effect. In addition, the large diameter circular cylinder allows uniform mixing with proppant and fiber before settlement tests are initiated so that the accuracy of the fall rate is better than slot tests with narrow square slots. The difficulty of proppant fall tests is to maintain the homogenous proppant slurry throughout the experiments. The properties of proppant such as the grain size distribution, shape and density are slightly different from different batches so that one series of tests must be performed using the proppant from the same container (22.7 kg (50 lb) container). The slight difference in the proppant properties significantly affect the proppant fall rate. For example, 20/40 mesh proppant particles have as much as 4 times fall velocity difference if the size changes from 40 to 20 mesh. Therefore, when experiments are conducted from a different batch, the grain size and single fall velocities need to be recorded to show the variation.

The fall rate (terminal or free settling velocity) for proppant may be calculated for the low Reynold's number using the Stokes' law given by **Eq. 5**:

$$v = \frac{cD^2(\rho_{prop} - \rho_f)}{\mu} \qquad (5)$$

where

- $\dfrac{D_p \rho_f u}{\mu}$ = Reynold's number

- $c = 8.3 \times 10^5$ for ideal spherical proppant

- $c = 2.0 \times 10^5$ for empirical velocity of spherical proppant (Fig.5-80, Perry's Chemical Engineers' Handbook)

- D = proppant diameter (inch)

- u = relative velocity between particle and main body of fluid

- μ = apparent viscosity of the fluid (cp)

- ρ_{prop}, ρ_f = proppant and fluid densities (sg)

According to **Eq. 5,** the terminal fall rate for 0.0728 cm (0.0287 inches) proppant with 2.71 SG should be 0.495 m/sec (1169 inches/min). Note that the Reynold's number for the proppant fall in water is within the laminar flow (Re=0.00001-0.00005). The empirical terminal velocities for the proppant settling (single proppant) in water are 4.1 times slower as shown in **Tables 4.** They agree with the empirical terminal velocity given by Fig.5-80 in Perry's Chemical Engineer's handbook. As **Table 4** shows, the 20/40 mesh ceramic proppant has a wide particle size range and the fall rate are 0.12-0.02<0.12(average) <0.12+0.025 m/sec (283-50< 283(average) <283+58 in/min). The table also shows that other properties such as the shape and the density variations also cause the variation of the fall rates.

Table 5 shows the effect of the slot width on the proppant fall rate. The fall rates should be different when the slot width is varied. However, the table shows that the effect of the slot width on the fall rate is very small compared with the effect of particle size and shape-irregularity as long as the slot width is larger than 0.00254 m (0.1 inches). The wall effect is completely masked by the effects of the non-uniformity of the grain size, grain shape irregularity and density variation. The single particle is so small with respect to the slot width that the wall does not significantly affect the fall speed if the wall is more than 0.00254 m (0.1 inches) wide.

Table 4. Proppant fall rate for 20/40 mesh (single proppant, for 4 inch ID cylinder tests).

Particle No	Particle diameter	Fall Velocity
	mm	inch/minute
1	0.85	233.3
2	0.86	256.2
3	0.92	344.5
4	0.83	243.7
5	0.85	333.5
6	0.77	251.8
7	0.81	248.3
8	0.74	330.0
9	0.76	341.3
10	0.73	245.7
11	0.74	251.9
12	0.86	320.6
Average	0.81	284

Table 5. Proppant fall rate for 20/40, 30/50 and 40/70 mesh proppant (single proppant, average value with more than 10 fall rate tests with the same condition).

slot width	20-40 mesh	30-50 mesh	40-70 mesh
0.1" slot	267	216	164
0.4" slot	263	187	153
4" Cylinder tests	283	217	147

Table 6 and **Fig. 25** shows the proppant fall velocities in water if the proppant concentration is varied between a single particle to multiple particles up to 479 kg/m³ (4 lb/gal). The proppant settling velocities are reduced with higher concentration of proppant. Note that the grain size for this series of experiments is larger than the previous experiments (**Table 4** compared with **Table 5**).

Table 6. 20/40 mesh proppant size used for fall velocity experiment

Particle No	Particle diameter	Fall Velocity
	mm	inch/minute
1	0.88	358.2
2	0.85	345.6
3	0.8	349.2
4	0.89	358.2
5	0.81	259.8
6	0.83	351
7	0.82	349.2
8	0.84	347.4
9	0.84	356.4
10	0.73	262.8
Average	0.829	333.8
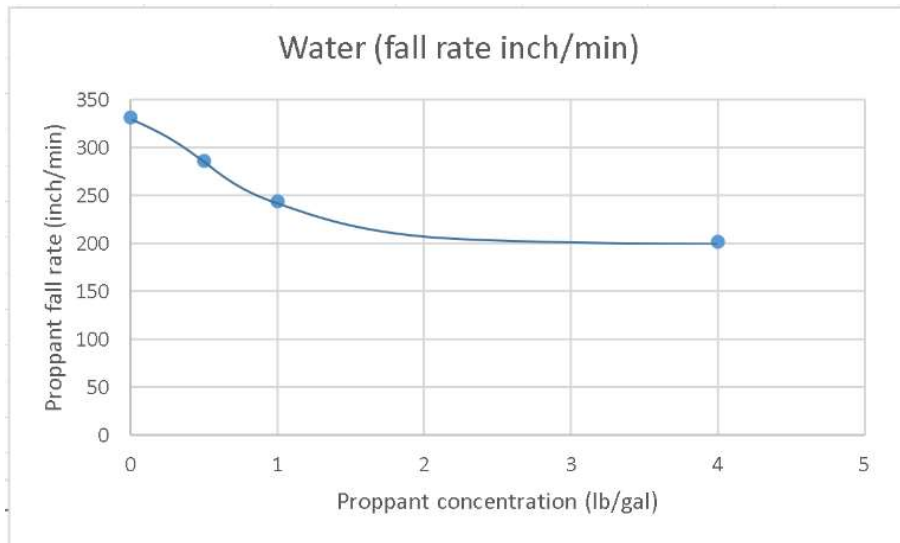
Figure 25. Effect of the proppant concentration on the fall rate test in water (20/40 mesh, water without guar).

Table 7 to Table 9 show the proppant fall rates for 60, 120, 479 kg/m³ (0.5, 1, and 4 lb/gal) of proppant with guar and fiber. The proppant fall rate becomes smaller as the proppant concentration is increased. However, occasionally, clusters of proppants were formed. Then, the fall rate of the cluster significantly increases comparing with the surrounding particles.

Fig. 26 and Fig. 27 shows the proppant fall rates with respect to proppant concentration and fluid viscosity. The proppant fall rate is slightly reduced with the proppant concentration. The fall rate shows inverse relationship with fluid viscosity.
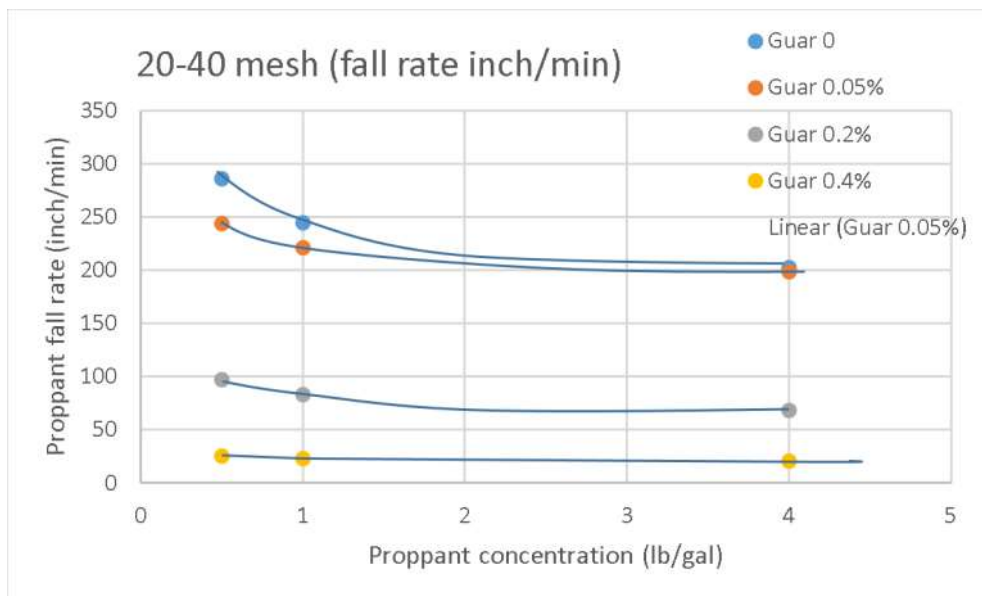
Figure 26. Proppant fall rates for different proppant and guar concentrations (20/40 mesh ceramic proppant)
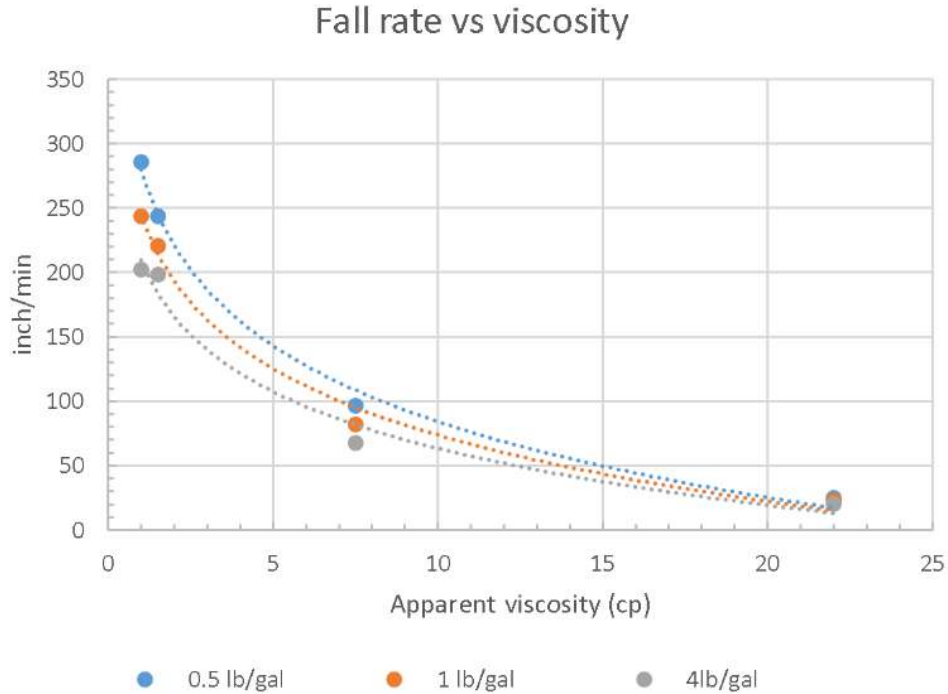
Figure 27. Proppant fall rates for different fluid viscosity and proppant concentrations (20/40 mesh ceramic proppant)

Fibers prevent proppant from falling and they work differently than the viscosifier by mechanically hindering/blocking the proppant from falling. **Fig. 28** to **30** show the proppant fall rates vs fiber concentration for 60, 120, 479 kg/m³ (0.5, 1 and 4 lb/gal) proppant. Note that the proppant fall tests with proppant concentration less than 60 kg/m³ (0.5 lb/gal) are not recorded since all the proppant particles are trapped within the fiber-water mixture and the fall rate becomes zero after some fiber-water column shrinkage if the proppant concentration is small. If the fiber concentration exceeds 1%, the proppant fall rate becomes zero with 60 to 479 kg/m³ (0.5-4 lb/gal) proppant concentration. The fall rate declines rapidly with fiber concentration if the proppant concentration is small. However, as the proppant concentration becomes higher, the amount of fiber required to reduce the proppant fall rate becomes larger.

Figure 28. Proppant fall rates for different fiber and guar concentration (0.5 lb/gal)

Figure 29. Proppant fall rates for different fiber and guar concentration (1 lb/gal).

43
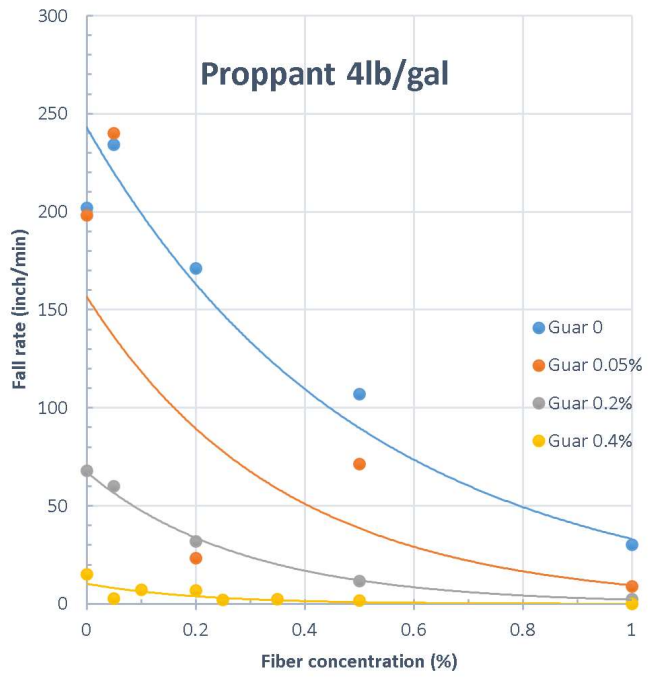
Figure 30. Proppant fall rates for different fiber and guar concentration (4 lb/gal).

Table 7. Proppant fall rate for 20/40 mesh proppant, 0.5 lb/gal.

20/40 mes		Proppant(lb/gal)	Fiber (%)	Guar(%)	Time0(sec)	Top0(inch)	Time1(sec)	Top1(inch)	Ave1(inch)	Bottom1(inch)	FallRate1(inch/min)	FallRate2(inch/min)	FallRate3(inch/min)
23	1	0.5	0	0	13.8	19.97	13.86667	1.6	1	0.9	275.55	284.55	286.05
	2	0.5	0.05	0	26.66667	15	26.73333	2	1.6	1	195.00	201.00	210.00
	3	0.5	0.2	0	5.45	18.5	6.083333	7	6	5.5	18.16	19.74	20.53
	4	0.5	0.5	0	30.21667	17	30.56667	11	10	10	17.14	20.00	20.00
	5	0.5	1	0	52.08333	18.5	62.56667	18.5	18.5	18.5	0.00	0.00	0.00
21		0.5	0	0.05	26.68333	17.23	26.75	1	1	1	243.45	243.45	243.45
		0.5	0.05	0.05	36.83333	18	36.93333	1.2	1.2	1.2	168.00	168.00	168.00
		0.5	0.2	0.05	52.46667	18	52.7	5.5	5	4.5	53.57	55.71	57.86
		0.5	0.5	0.05	14.1	18	16.11667	13.2	13	13	2.38	2.48	2.48
		0.5	1	0.05	34.08333	17.5	36.88333	16.5	16	16	0.36	0.54	0.54
17		0.5	0	0.2	43.08333	17.68	43.18333	10	8.5	8	76.80	91.80	96.80
		0.5	0.05	0.2	0.966667	15	1.083333	10	8	7	42.86	60.00	68.57
		0.5	0.2	0.2	22.06667	18	22.35	16	11	8	7.06	24.71	35.29
		0.5	0.5	0.2	49.08333	18	52.03333	16	15	15	0.68	1.02	1.02
		0.5	1	0.2	11.73333	18.2	17.58333	17	17	17	0.21	0.21	0.21
13		0.5	0	0.4	11.5	23	12.18333	12	11	9.5	16.10	17.56	19.76
		0.5	0.05	0.4	23.8	18.3	24.56667	13	4	2	6.91	18.65	21.28
		0.5	0.1	0.4	50.96667	18	52.5	3	1.5	1.1	9.78	10.76	11.02
10		0.5	0.2	0.4	29.35	18	30.4	11	6	4	6.67	11.43	13.33
		0.5	0.25	0.4	57.83333	18	61.38333	12.5	12	12	1.55	1.69	1.69
		0.5	0.35	0.4	46.5	18	53.8	16	15.5	15	0.27	0.34	0.41
		0.5	0.5	0.4	25.58333	18	30.61667	17.3	17.3	17.3	0.14	0.14	0.14
		0.5	1	0.4	13.81667	18.5	22.5	18	18	18	0.06	0.06	0.06

Table 8. Proppant fall rate for 20/40 mesh proppant, 1 lb/gal.

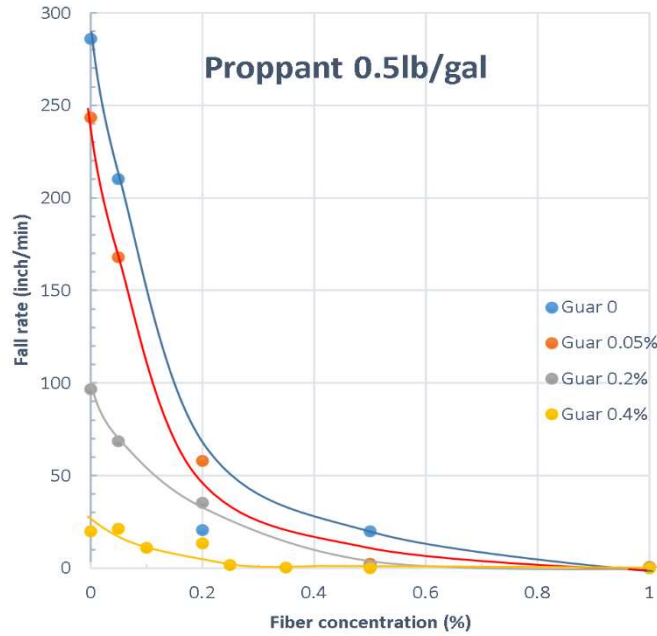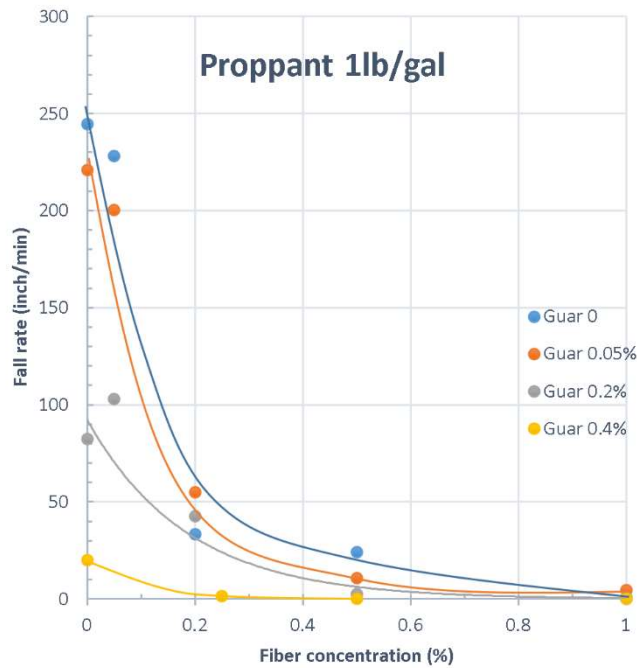|		Proppant(lb/gal)	Fiber (%)	Guar(%)	Time0(sec)	Top0(inch)	Time1(sec)	Top1(inch)	Ave1(inch)	Bottom1(inch)	FallRate1(inch/min)	FallRate2(inch/min)	FallRate3(inch/min)
		1	0	0	57.26667	18.1	57.33333	1.8	1.8	1.8	244.50	244.50	244.50
		1	0.05	0	12.98333	17	13.05	15	1.9	1.8	30.00	226.50	228.00
		1	0.2	0	0.102833	16	0.238	4	4	4	88.78	88.78	88.78
		1	0.5	0	29.28333	18	29.7	9	8	8	21.60	24.00	24.00
		1	1	0	51.91667	18.5	67.68333	17.5	17	17	0.06	0.10	0.10
21		1	0	0.05	23.53333	19.91	23.616	1.5	1.5	1.5	222.70	222.70	222.70
		1	0.05	0.05	40.65	18.5	40.73333	2.2	1.9	1.8	195.60	199.20	200.40
		1	0.2	0.05	1.35	17	1.583333	4.5	4.2	4.2	53.57	54.86	54.86
		1	0.5	0.05	59.31667	17.5	60.01667	10.2	10	10	10.43	10.71	10.71
		1	1	0.05	22.86667	17.5	23.58333	14.7	14.2	14.2	3.91	4.60	4.60
20		1	0	0.2	0.403333	17.2	0.5675	1.4	1.2	1.2	96.24	97.46	97.46
		1	0.05	0.2	29.51667	16	29.63333	10.5	7	4	47.14	77.14	102.86
		1	0.2	0.2	14.66667	17.5	14.98333	10	6	4	23.68	36.32	42.63
		1	0.5	0.2	40.68333	18.5	42.16667	16.2	15	15	1.55	2.36	2.36
		1	1	0.2	3.166667	18.5	6.283333	17	16.5	16.5	0.48	0.64	0.64
10		1	0	0.40	15.1	17	15.5	9	9	9	20.00	20.00	20.00
13		1	0.25	0.40	26.32	18.00	31.95	16.00	11.00	10.00	0.36	1.24	1.42
		1	0.5	0.4	7.066667	18.5	12.53333	17.9	17.9	17.9	0.11	0.11	0.11
		1	1	0.4	30	18.5	40.1	18.3	18.3	18.3	0.02	0.02	0.02

Table 9. Proppant fall rate for 20/40 mesh proppant, 4 lb/gal.

	Proppant(lb/gal)	Fiber(%)	Guar(%)	Time0(sec)	Top0(inch)	Time1(sec)	Top1(inch)	Ave1(inch)	Bottom1(inch)	FallRate1(inch/min)	FallRate2(inch/min)	FallRate3(inch/min)
24	4	0	0	50.81667	15.6	50.8665	6.2	5.8	5.5	188.64	196.67	202.69
	4	0.05	0	12.26667	17.5	12.31667	6.5	6	5.8	220.00	230.00	234.00
	4	0.2	0	29.18333	17.5	29.25	9	7.5	6.1	127.50	150.00	171.00
	4	0.5	0	0.718333	17.5	0.869333	10.5	10.5	10.5	46.36	46.36	46.36
	4	1	0	37.05333	17.5	37.18333	14	13	13	23.33	30.00	30.00
22	4	0	0.05	2.283333	16.61	2.316667	12	10.5	10	138.30	183.30	198.30
	4	0.05	0.05	18.58333	17.5	18.6	14.5	14	13.5	180.00	210.00	240.00
	4	0.2	0.05	38.78333	15.5	39.15	13	8	7	6.82	20.45	23.18
	4	0.5	0.05	57.61667	20.5	57.75	13	17	11	56.25	26.25	71.25
	4	1	0.05	34.93333	20.5	35.83333	14	13	12.5	7.22	8.33	8.89
20	4	0	0.2	39.96667	19.24	40.15	6.8	6.8	6.8	67.85	67.85	67.85
	4	0.05	0.2	0.433333	19	0.55	14	13	12	42.86	51.43	60.00
	4	0.2	0.2	25.15	20.5	25.41667	14.5	13	12	22.50	28.12	31.87
	4	0.5	0.2	46.73333	20.5	47.3	16	15	14	7.94	9.71	11.47
	4	1	0.2	9.933333	20.5	11.96667	16	16	16	2.21	2.21	2.21
15	4	0	0.4	11.25	20.5	11.88333	19	14	11	2.37	10.26	15.00
	4	0.05	0.4	49	20.5	49.95	19	15	18	1.58	5.79	2.63
	4	0.1	0.4	19.66667	20.5	20.83333	19	14	12	1.29	5.57	7.29
	4	0.2	0.4	48.85	20.5	50.23333	20	13	11	0.36	5.42	6.87
	4	0.25	0.4	17.2	20.5	18.98333	19.5	18	17	0.56	1.40	1.96
	4	0.35	0.4	44.06667	20.5	45.63333	19.5	18	17	0.64	1.60	2.23
	4	0.5	0.4	11.28333	20.5	13.9	19.5	17	16	0.38	1.34	1.72
	4	1	0.4	43	20.5	52.21667	20	20	20	0.05	0.05	0.05

Fig.31 to **34** compare the final proppant settlement at a large time duration when the movement of proppant has ceased. Three layers are formed: fluid, fiber and proppant clusters, and proppant with no fiber. The conglomerate consists of approximately 60-84 kg/m³ (0.5-0.7 lb/gal) proppant with 1% fiber. Therefore, if the frac fluid contains 1% fiber, all the proppants are retained in place without falling.
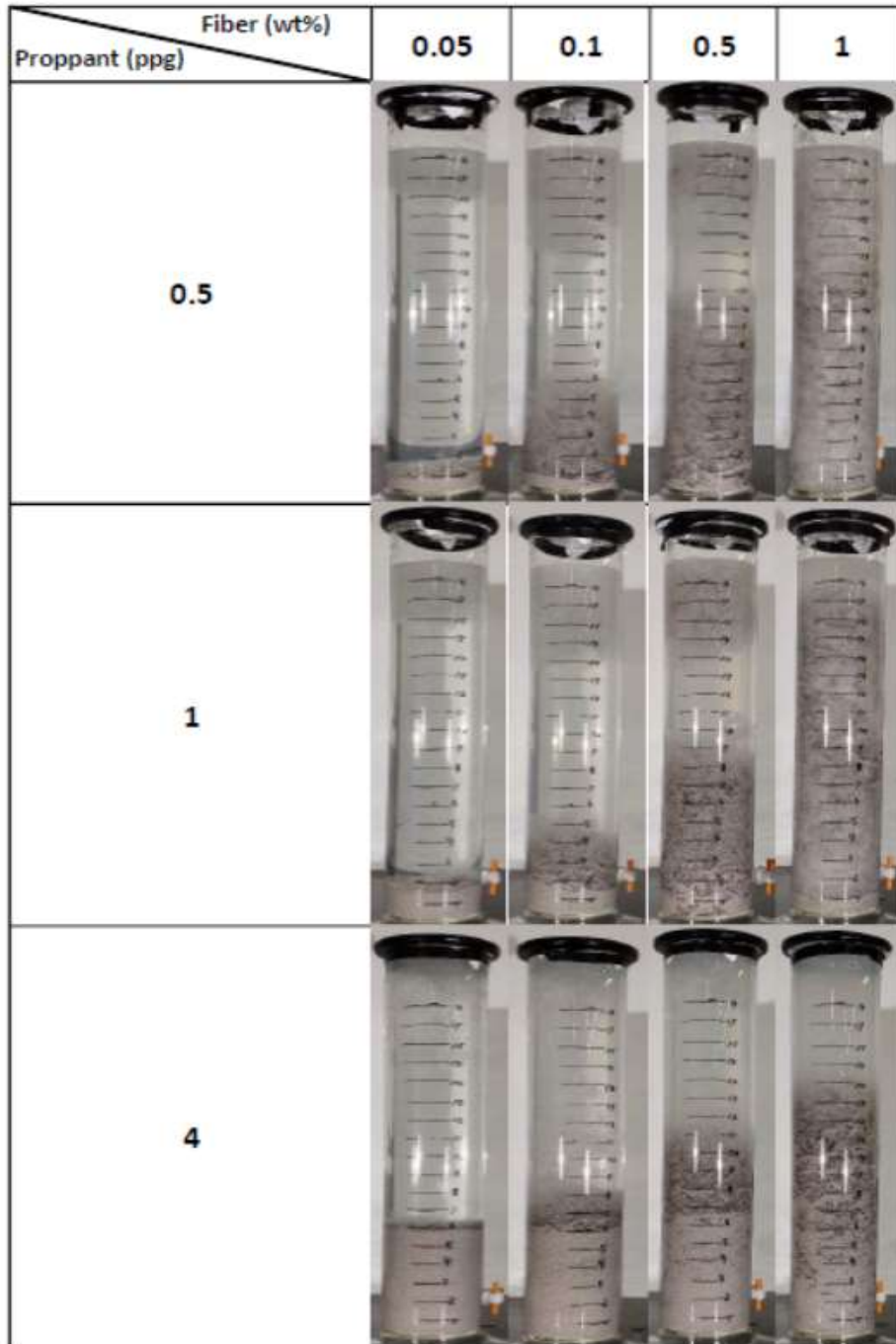
Figure 31. Static fall rate test with 4 inch ID cylindrical container with different fiber concentration (0% Guar).

Figure 32. Static fall rate test with 4 inch ID cylindrical container with different fiber concentration (0.05% Guar).
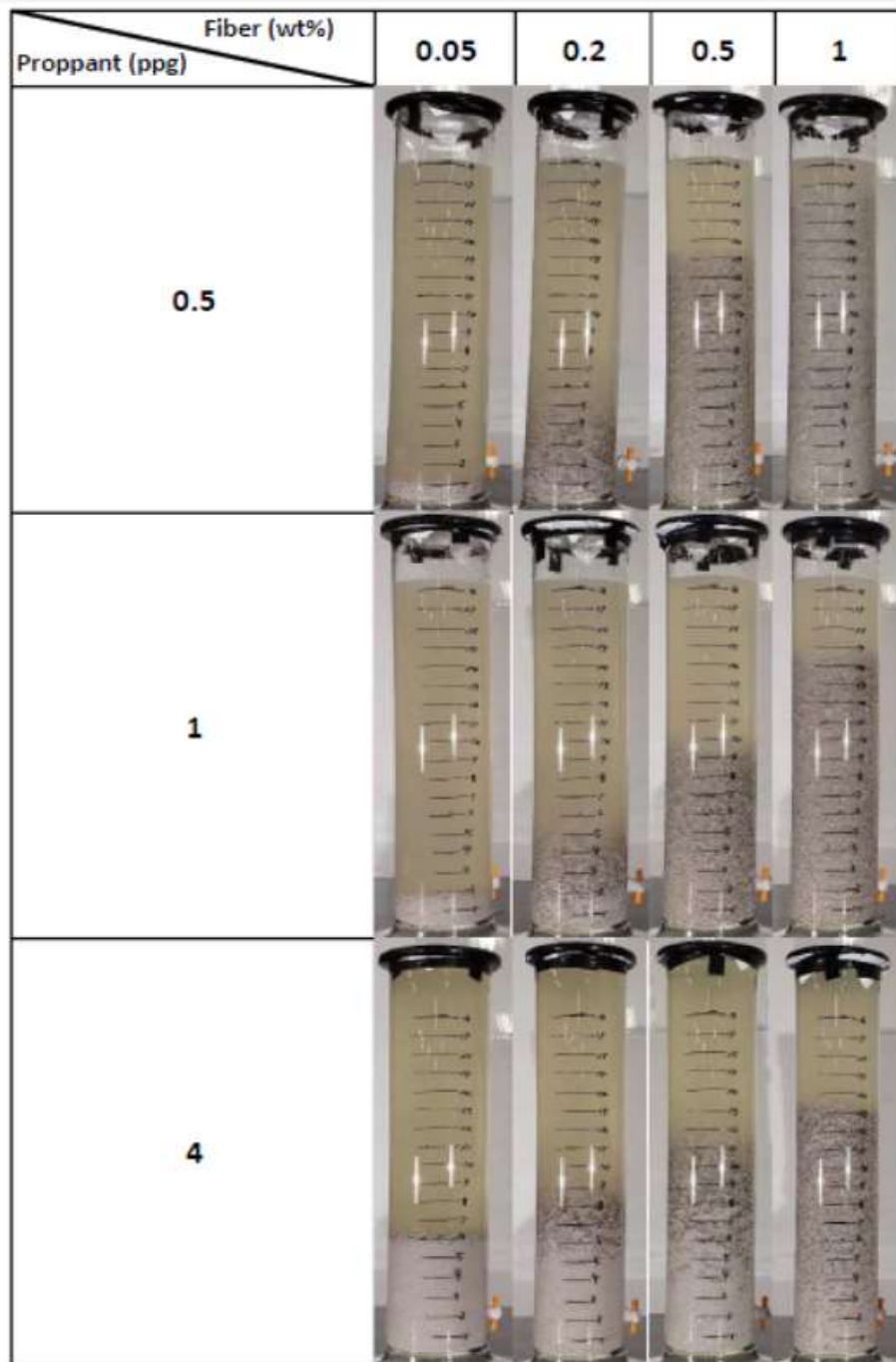
Figure 33. Static fall rate test with 4 inch ID cylindrical container with different fiber concentration (0.2% Guar).
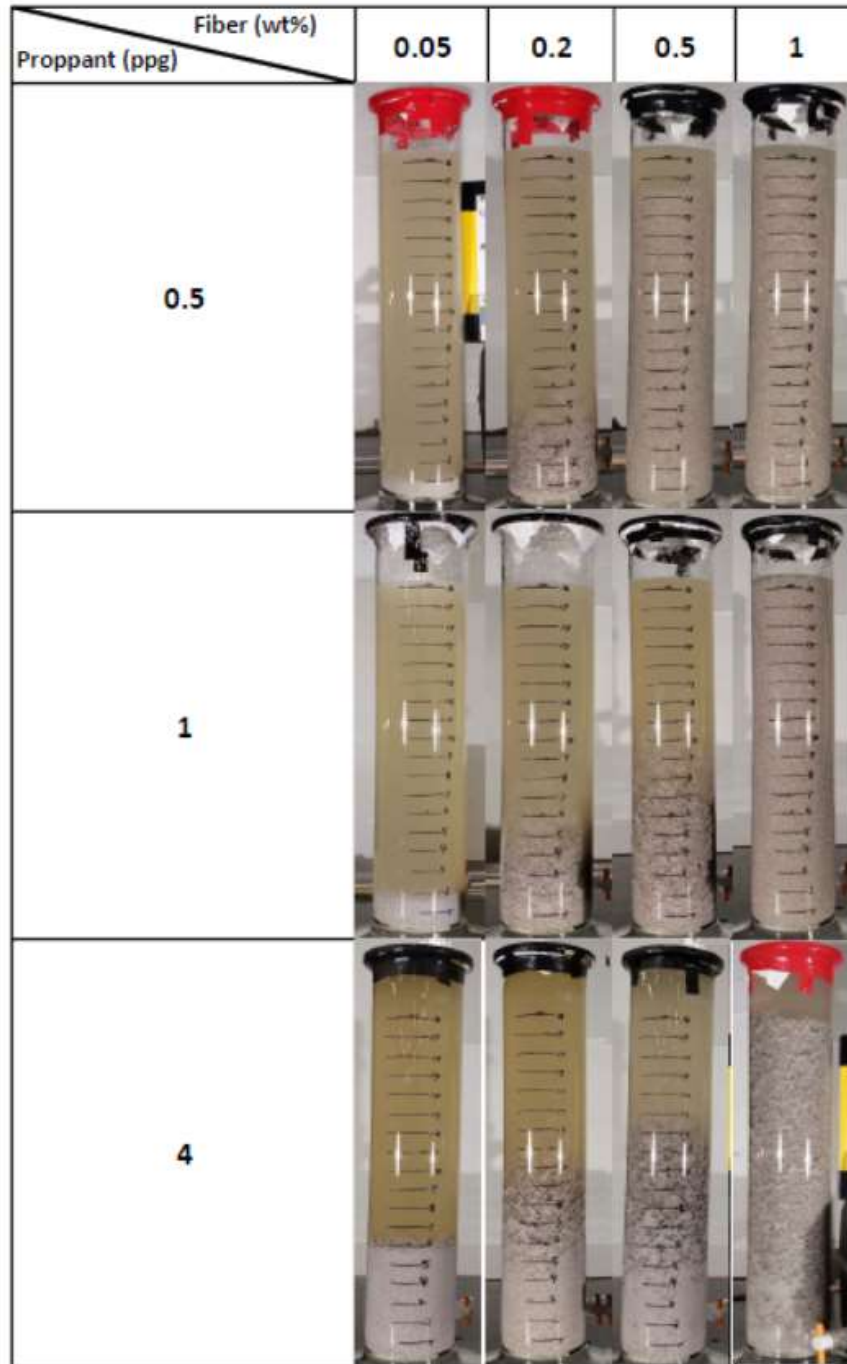
Figure 34. Static fall rate test with 4 inch ID cylindrical container with different fiber concentration (0.4% Guar).

Static proppant settlement test (with 0.2" and 0.4" slots)

Proppant settling rate is not uniform in both lateral and vertical directions. Especially if fiber is mixed, the fiber and proppant form clusters of various sizes. These clusters settle with different velocities depending on the cluster sizes. Therefore, only the average fall rates of the dominant clusters are recorded. **Fig. 35** shows the settling rates for 0.00508 and 0.01 m (0.2 inches and 0.4 inches) slots and cylinder tests. The settling rates significantly fluctuate since some clusters are stuck between the narrow walls. However, overall settling rates are not significantly affected by the slot width as long as the slot width is more than 0.00508 m (0.2 inches). It indicates that the proppant sizes are an order of magnitude smaller so that the settling rate is not affected by the wall. However, if a large cluster of proppant and fiber is formed, it is stuck at the middle of the slot, although the overall settling rate remains unaffected except for the surrounding area of the stuck clusters.

Fig. 36 and **37** compare the final proppant settlement at a large time when the movement of proppant has ceased. Just like the cylinder settling tests, three layers are formed: fluid, fiber and proppant clusters, and proppant. Comparing with **Fig. 36** and **37,** the ratios of the three-layer thicknesses at the final proppant settlement are not significantly different regardless of the slot width. However, one difference is that the probability of cluster suspensions at upper section is high without complete settling at the slot bottom.
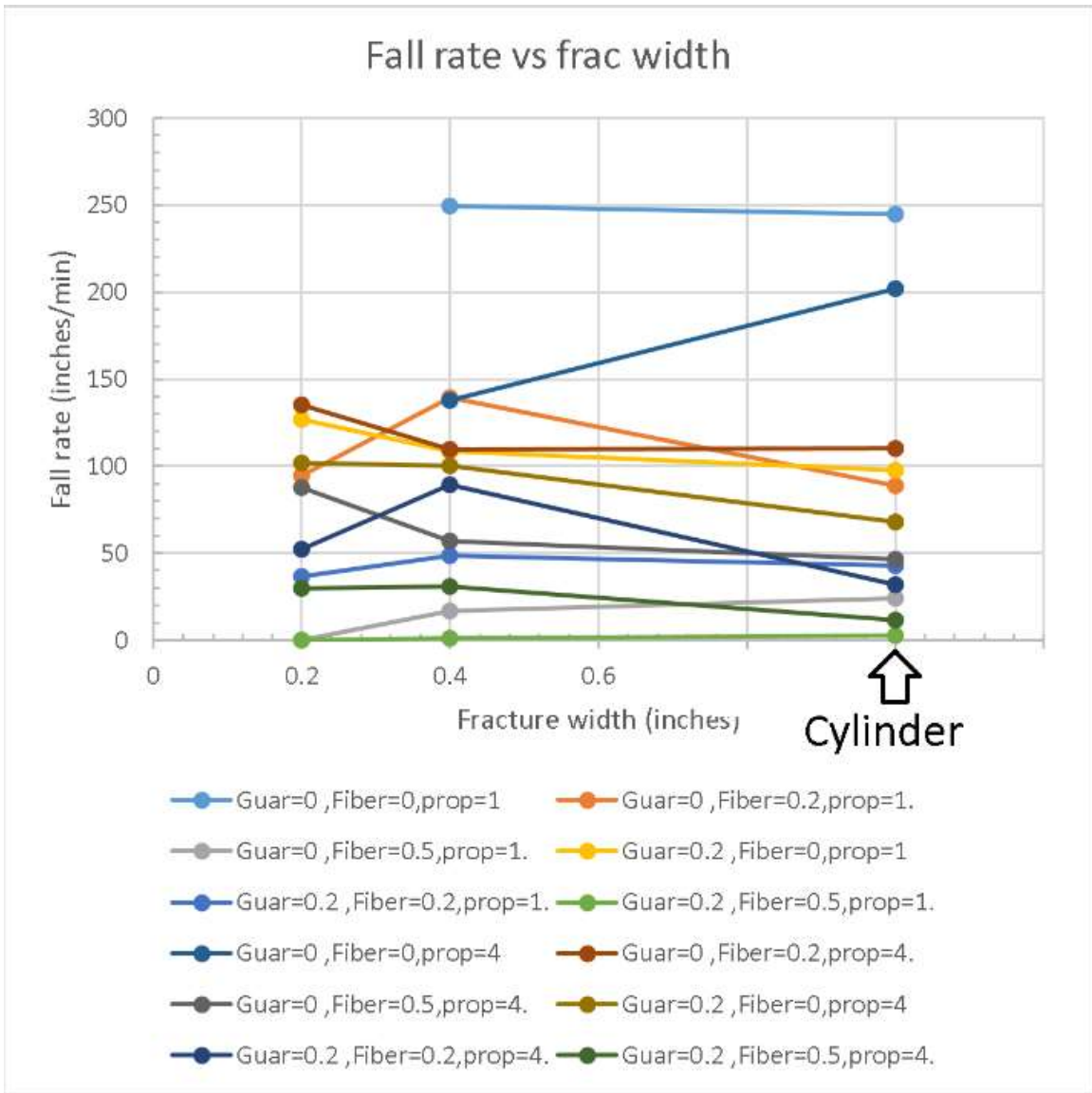
Figure 35. Proppant fall rate comparison for different slot width, guar, fiber, and proppant concentrations.

Figure 36. Static fall rate test with 0.2 inch slot (20/40 mesh ceramic proppant).
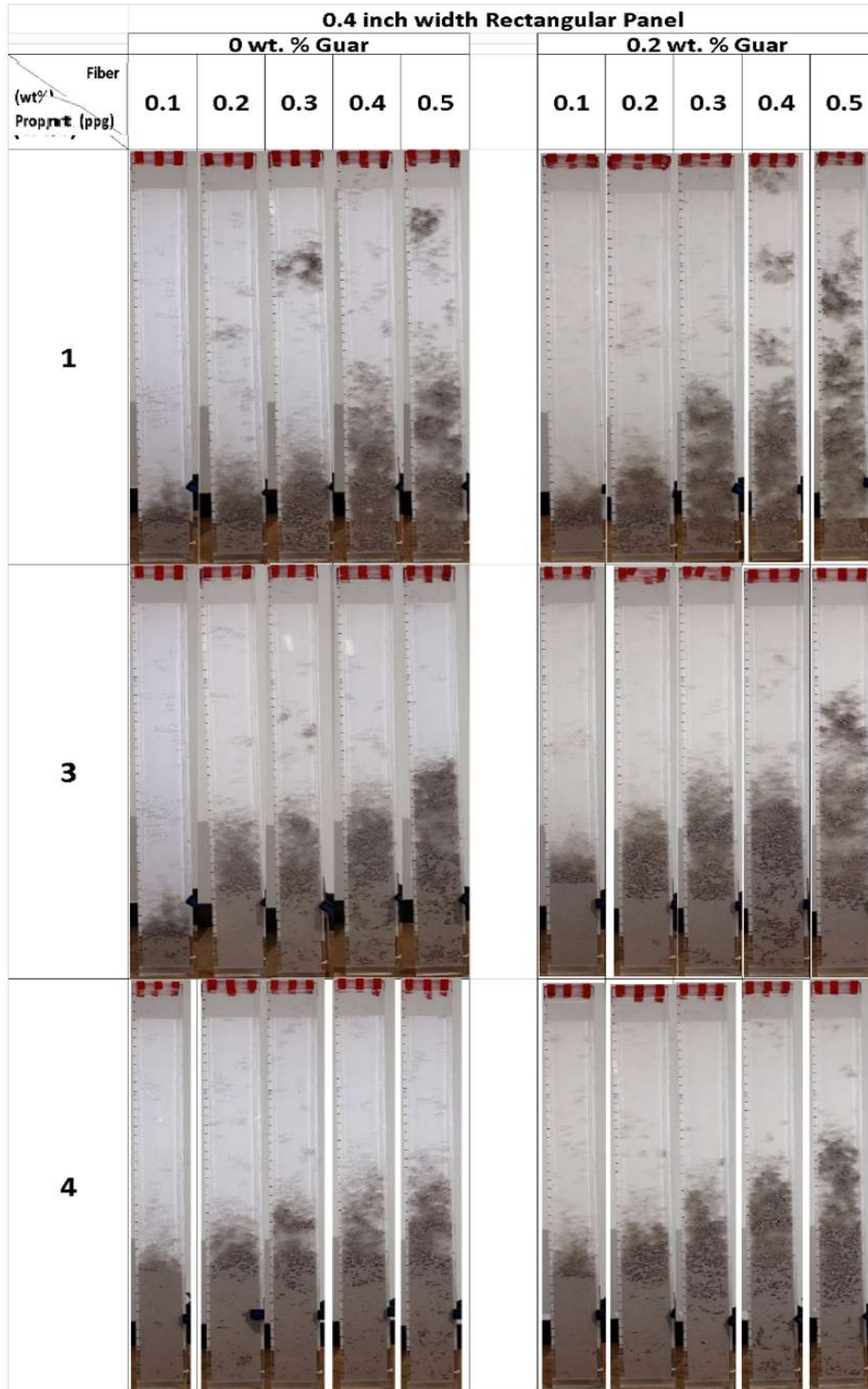
Figure 37. Static fall rate test with 0.4 inch slot (20/40 mesh ceramic proppant).

Large scale dynamic proppant transport test

The experimental result shows that the transport mechanisms with and without the presence of guar are significantly different when fibers are used. **Fig. 38** and **Fig.39** show the proppant transport comparison under the same condition except the presence of guar. The absence of the guar with low hydrodynamic force lead to fibers being concentrated into dense flocculation as shown in **Fig. 39.** The fiber flocculation creates non-uniform fiber network forming flow channels within the previously injected fiber-proppant fluid. The channels lead to higher fluid velocity through the proppant-fiber network. The test fluids with the guar leads to **Fig. 38**. The proppant-fiber-clusters are more dispersed with the guar, and the dense fiber flocculation only occurs on the bottom of the panel due to the cluster settlement. The increase in proppant dune slope toward the outlet indicates excellent horizontal transport capability under the test condition.
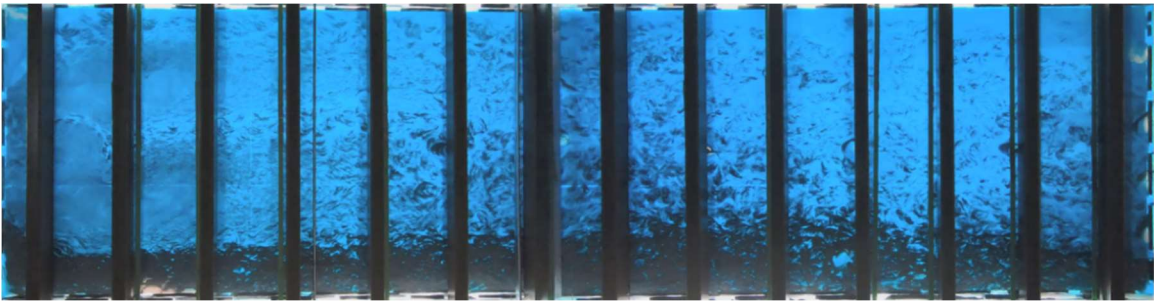
Figure 38. Proppant transport with guar at 2 minutes of pumping the slurry shows a good horizontal transport capability of the test slurry (0.2 wt. % guar, 0.3 wt. % fiber (PGA 13 mm), 30/50 ceramic proppant, 8.5 cp).

Figure 39. Proppant transport without guar at 2 minutes of pumping the slurry shows channel formation acting as a flow conduit for following slurry to flow through (0.3 wt. % fiber (PGA 13 mm), 40/70 ceramic proppant, 1.8 cp).

Effect of fiber concentration (6mm) on proppant transport with guar

Fig. 40 and **41** compare proppant transport with three different PGA fiber (6 mm) concentrations of 0.1, 0.2 and 0.3 wt. %. All three test fluids contain 0.2 wt. % guar with 1 ppg concentration 30/50 mesh ceramic proppant. The formation of the proppant bedding mechanism is similar in all three experiments. In this case, the proppants are transported mainly by the free settling and hindered settling. Rolling and saltation take limited role near the inlet where the local fluid velocity is the highest. It can be observed that the location of the maximum proppant dune height shifted toward the outlet as the fiber concentration increases. Also, the proppant-fiber-clusters are more visible as the fiber concentration is increased.

Figure 40. Quality of the proppant dune comparison with 0.2 wt. % guar at 30, 90, 180 second and 2 minutes after the pump is shut down for different fiber concentrations (0.1, 0.2, and 0.3 wt. % PGA fiber (6 mm), 30/50 mesh proppant).

56
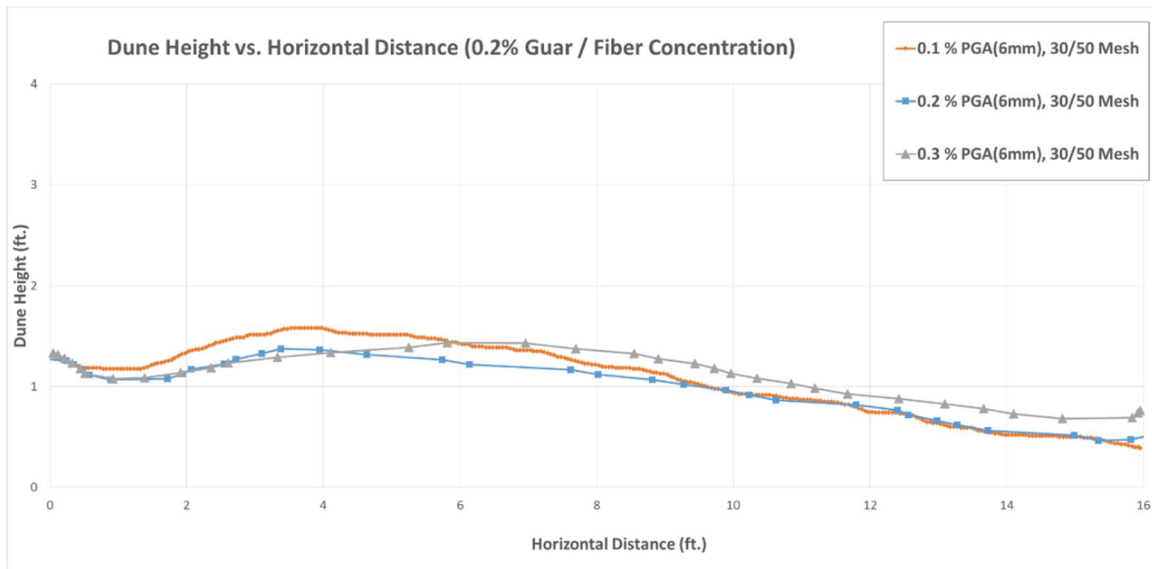
Figure 41. Graphical Proppant dune comparison with 0.2 wt. % guar after the pump is shut down for three different fiber concentration (0.1, 0.2, and 0.3 wt. % PGA fiber (6 mm), 30/50 ceramic proppant).

Effect of fiber concentration with longer fiber (13 mm) on proppant transport

As the 13 mm length PGA fiber concentration increases from 0.2 to 0.3 wt %, formation of the fiber-proppant-clusters is more prominent compared to the 6 mm length PGA fiber as shown in **Fig. 42**, indicating that increasing the fiber length increases the flocculation of the fibers when the cross-sectional area perpendicular to the flow is fixed. Moreover, the maximum height location shifted significantly further toward the outlet side as shown in **Fig.43**. Other observation is the buildup of fiber-proppant-flocculation on the bottom of the panel, and the suspension of the proppant islands. As explained, the proppant islands are formed because the hydrodynamic force is less than the mechanical force that is holding the fibers together. Furthermore, the suspension of the fiber-proppant-islands is due to the fact that the mechanical force from the contact between the panel wall and the fiber-proppant-islands is greater than the gravitational force pulling the islands.

Figure 42. Proppant dune comparison with 0.2 wt. % guar at 30, 90, 180 second and 2 minutes after the pump is shut down for two different fiber concentrations (0.1, and 0.3 wt. % PGA fiber (13 mm), 30/50 ceramic proppant).
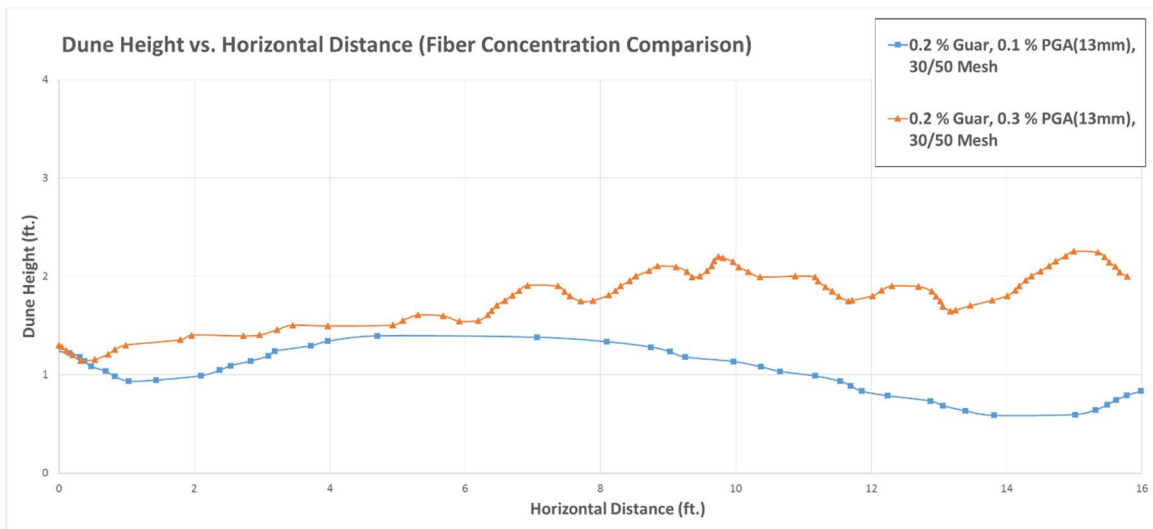
Figure 43 Graphical proppant dune comparison with two different fiber concentration (0.1 and 0.3 wt. % PGA fiber (13 mm), 30/50 ceramic proppant with 0.2 wt. % guar).

Effect of proppant size on proppant transport

Fig. 44 and **Fig. 45** compare proppant dune of the same concentration guar and

same concentration fiber: 0.2 wt. % guar and 0.1 wt. % PGA fiber. The only difference is

the proppant mesh size. The test fluid with 40/70 mesh size has the location of the

maximum proppant height more toward the outlet and the proppant suspension is more prominent as shown in **Fig.45**. This indicates that the smaller diameter of the proppant helps in reducing the fall rate of the proppant leading to further horizontal travel distance of the proppant clusters.
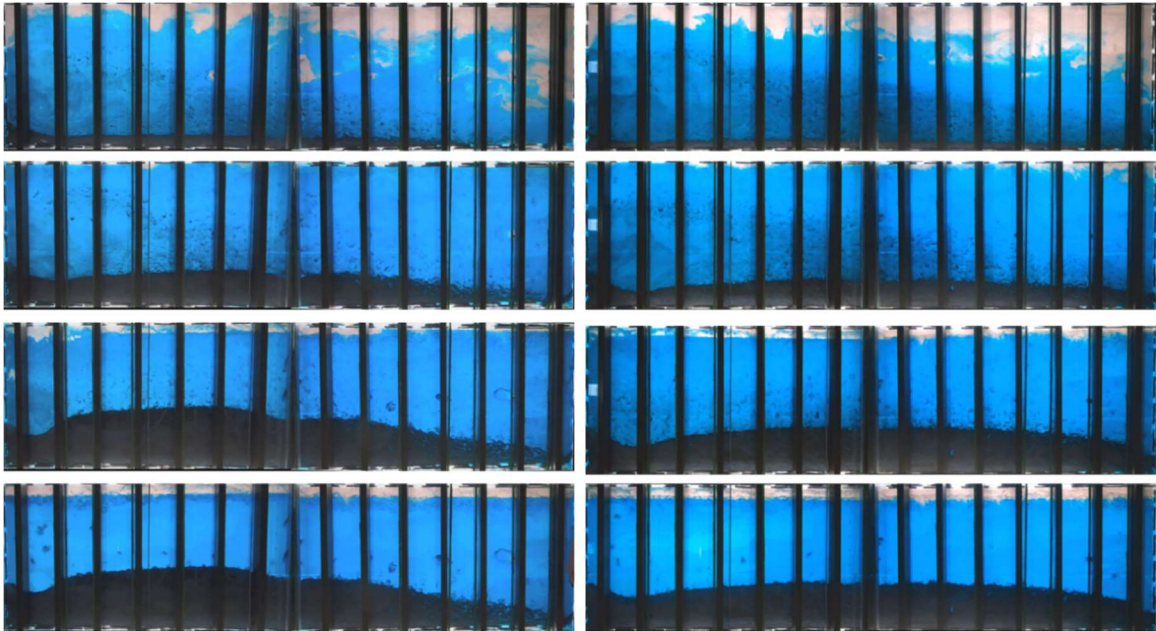
Figure 44. Proppant dune comparison with 0.1 wt. % PGA fiber at 30, 90, 180 second and 2 minutes after the pump is shut down for two different proppant mesh size (0.1wt. % guar, 30/50 left and 40/70 ceramic proppant right).
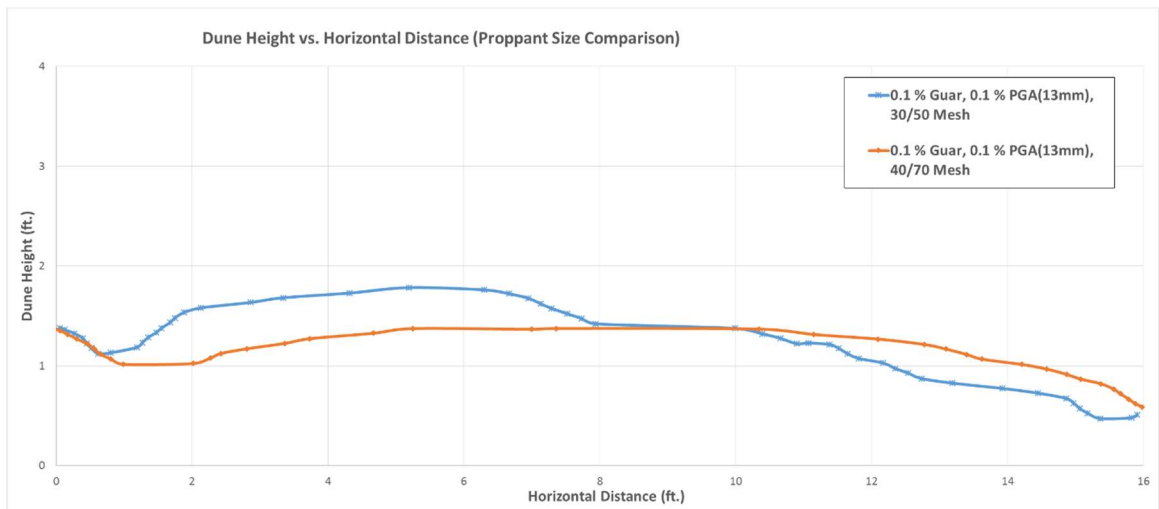
Figure 45. Graphical proppant dune comparison with two different proppant mesh size (0.1 wt. % PGA fiber (13 mm), 30/50 and 40/70 ceramic proppant with 0.1 wt. % guar)

Fig. 46 shows the role of guar concentration in the presence of low concentration 13 mm PGA fiber. The rate of dune formation from the early stage is noticeably different when three figures are compared as early as 30 seconds. The experiment with 0.05 wt. % guar test fluid displays early fiber-proppant-flocculation near the inlet whereas the 0.1 and 0.2 wt. % guar test fluid does not indicate early flocculation of fibers. As the guar concentration increases, the peak of the proppant dune shifts to the outlet with more even dune distribution as shown in **Fig.47**. As explained, the fiber flocculation occurs when the shear stress from the fluid is less than the mechanical force holding the fiber and proppants together. As seen from the 0.05 wt. % guar, the fiber tends to form fiber-proppant-flocculation early and accumulates proppants.
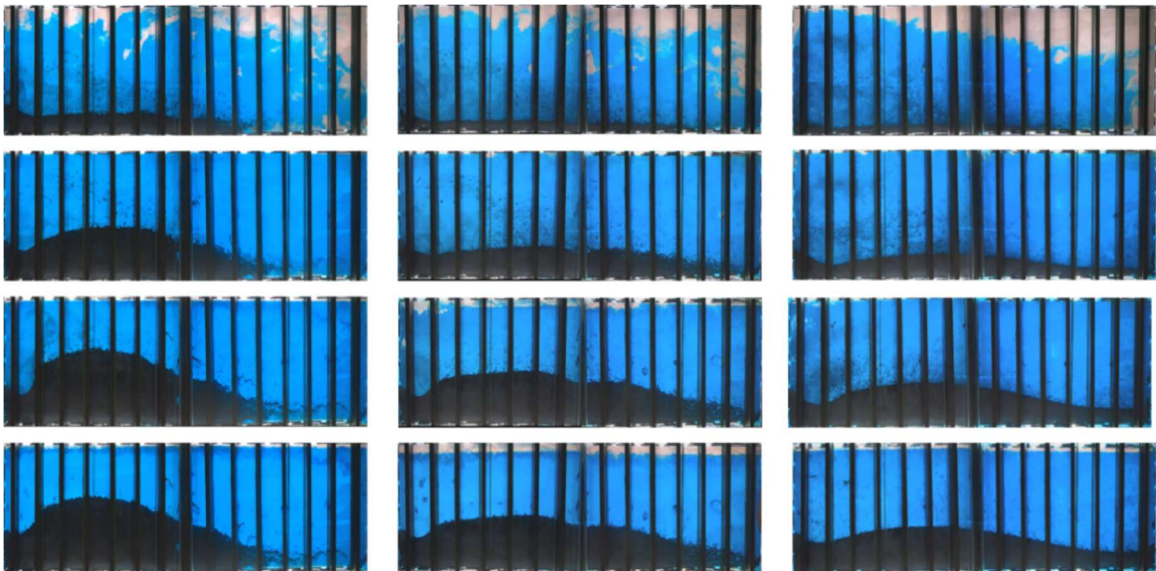
Figure 46. Proppant dune comparison with 0.1 wt % PGA fiber at 30, 90, 180 second and 2 minutes after the pump is shut down for different guar concentration (0.05, 0.1 and 0.2 wt % guar, left, middle and right figures, 30/50 ceramic proppant).
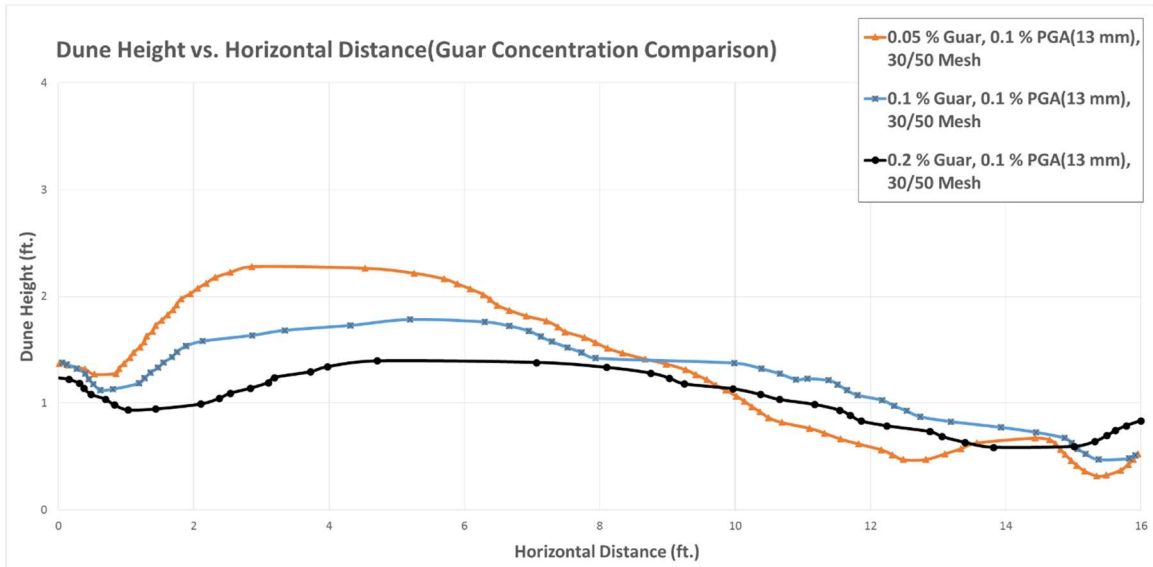
Figure 47. Graphical proppant dune comparison with three different guar concentration (0.1 wt. % PGA fiber (13 mm), 30/50 ceramic proppant with 0.1 wt. % guar).

Fig. 48 and **Fig. 49** show the proppant transport without the presence of any guar. This means the viscosity of the guar is kept very low. **Fig. 48** shows the proppant transport only when the fiber concentration is increased from 0 to 0.2 wt. % with 40/70 mesh. As it can be seen from the screen capture comparisons, the fiber-proppant-flocculation channel begins to form as early as 30 seconds after the pump initiation. The channels are created through the fiber-proppant network as the injected fluid has a higher mobility than previously injected fiber-proppant network. As the channel is created, the cross-sectional flow area is significantly reduced. This leads to higher local fluid flow rates through the created channels. The created channels serve as a conduit to transport the proppants further toward the outlet. The velocity of the fluid suddenly drops in the region where the channels get widen. At this area, loose fiber-proppant flocculation forms and continues to extend the channels.
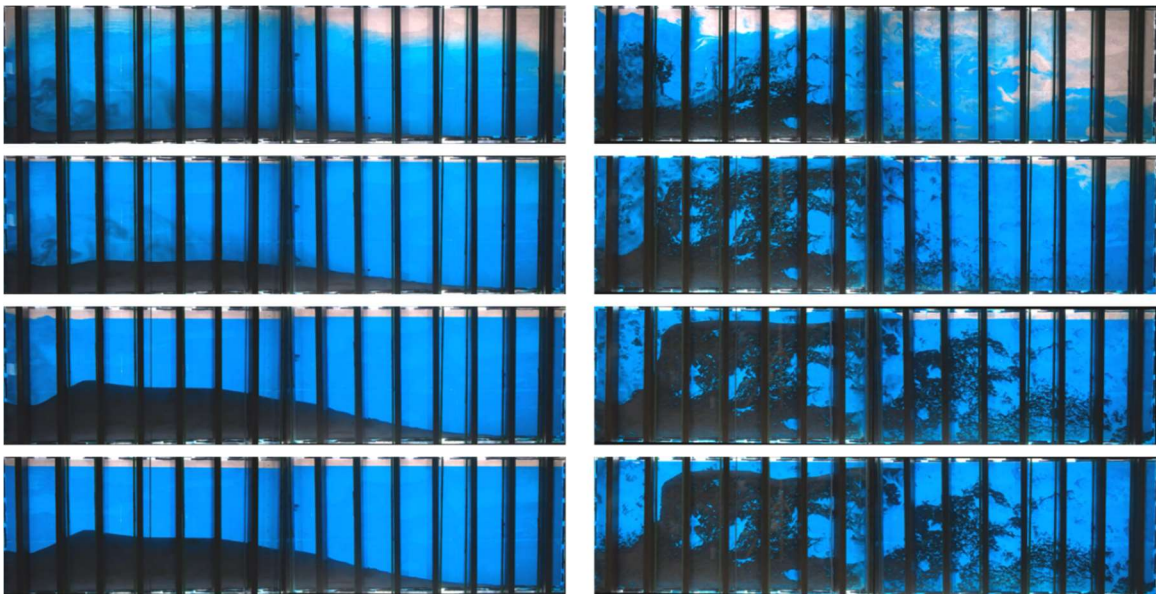
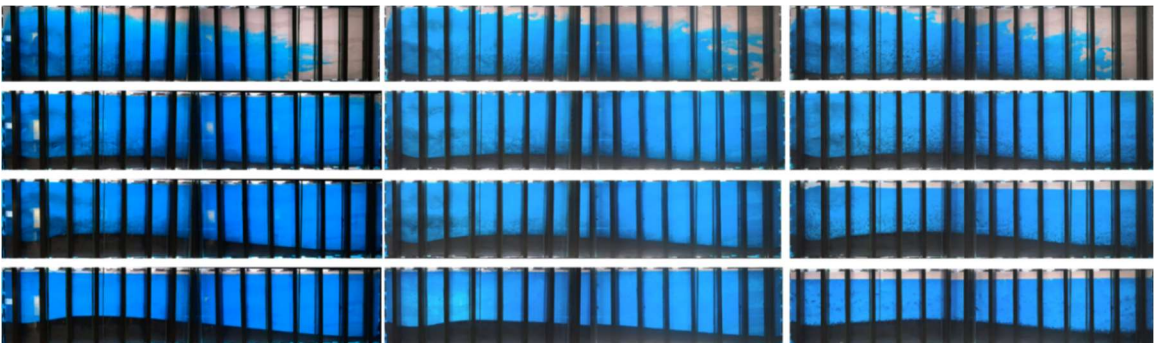**Figure 48. Proppant dune comparison with no guar at 30, 90, 180 second and 2 minutes after the pump is shut down for two different fiber concentration (0 and 0.2 wt. % 13 mm PGA Fiber, 40/70 ceramic proppant).**

Fig. 49 shows the proppant transport comparison for 0.1 and 0.3 wt. % fiber with

30/50 mesh proppant without the presence of guar. The screen capture on the left show

inability of the fiber-proppant-flocculation to suspend. As the fluid flow continues, the

hydrodynamic force breaks the suspended flocculation leading to settlement of the islands.

The 0.1 wt. % of fiber is not sufficient to hold the proppant suspended. In contrast, the 0.3

wt. % of fiber is sufficient to create fiber-proppant-islands which leads to channel

formation as shown on the right side of the figure. The fiber concentration is important in

supporting the weight of the proppants from destroying the created channels.

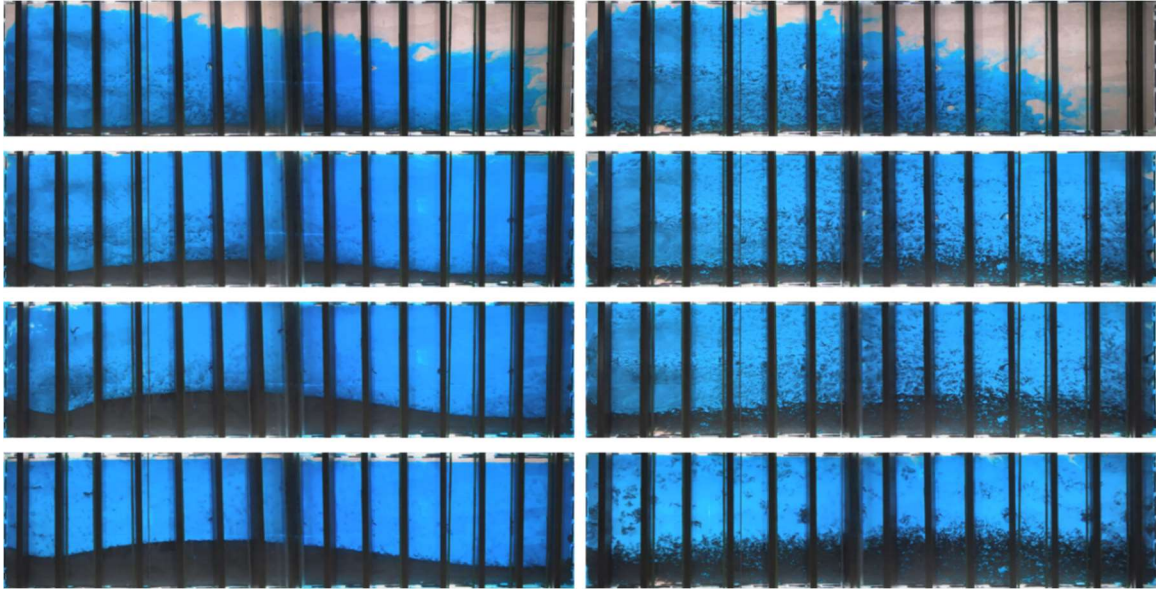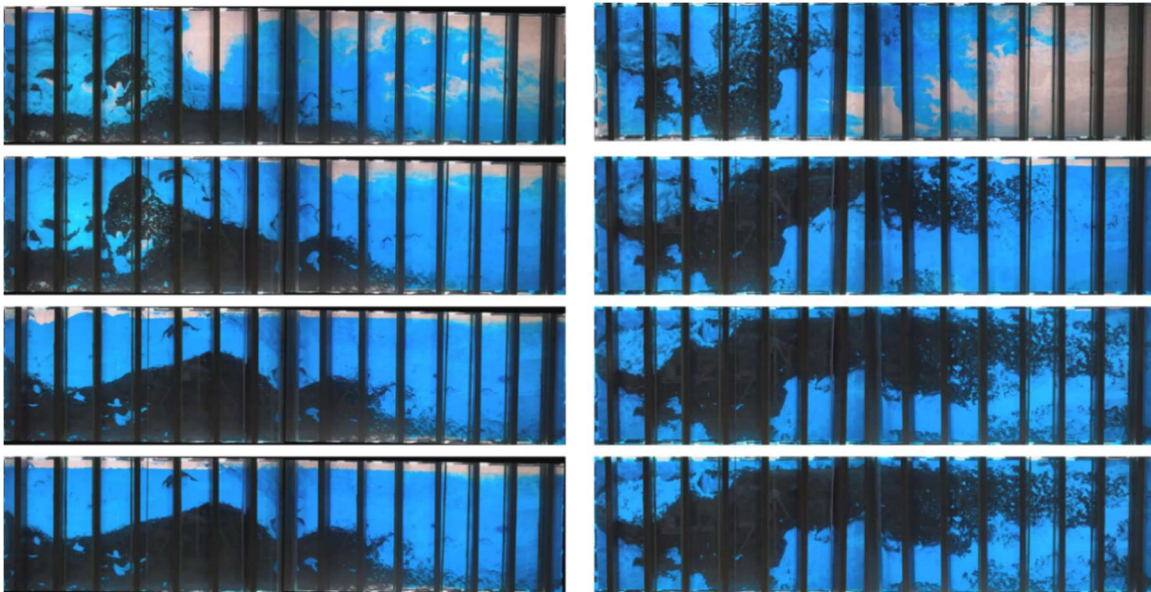**Figure 49. Proppant dune comparison with no guar at 30, 90, 180 second and 2 minutes after the pump is shut down for two different fiber concentration (0.1 and 0.3 wt. % 13 mm PGA Fiber, left (0.1) and right(0.3) figures, 30/50 ceramic proppant).**

Selection of PGA or PLA fibers

The experiments at room temperature showed no difference between PGA and PLA

for the proppant transport capacity if each fiber with approximately 20 μm OD was

untangled (18.5-micron diameter for PGA fiber and 21-micron diameter for PLA fiber in

the current experiments). The efficiency of fiber transport may depend on the separation of each fiber from threads consisting of ten to twenty 20 μm diameter strings as separated fibers would make better fiber clustering. Therefore, chemical surface treatment is needed to effectively separate into the small diameter strings. Previous measurement of the properties of PGA and PLA fibers at high temperature (Yoshimura 2016) showed that a certain degree of strength was maintained for PGA fiber while the PLA fibers were softened so that PGA fibers should be more effective at a standard reservoir temperature, although PGA fibers were turn into liquid acid faster (several hours) than PLA fibers (several days).

Although very small amount of PGA fiber at 0.1 wt. % with 0.1 wt. % guar is used in this case as seen from **Fig. 50**, fiber-proppant lamination can be observed in the settled proppant-fiber agglomerates. The laminated layer will act as a high conductive conduit for the hydrocarbons to flow through after the fiber turn into acid due to hydrolysis. Because the fiber-proppant lamination occupies large volume of the fracture, less of proppants are needed to keep the fracture open when the fracture operation stops, given that the closure stress is less than the proppant strength. It should be also noted that the fibers will degrade with water in the reservoir condition within few hours for PGA and few days for PLA (Tran et al., 2017). This will lead to a better proppant conductivity as the hydrocarbon production continues.
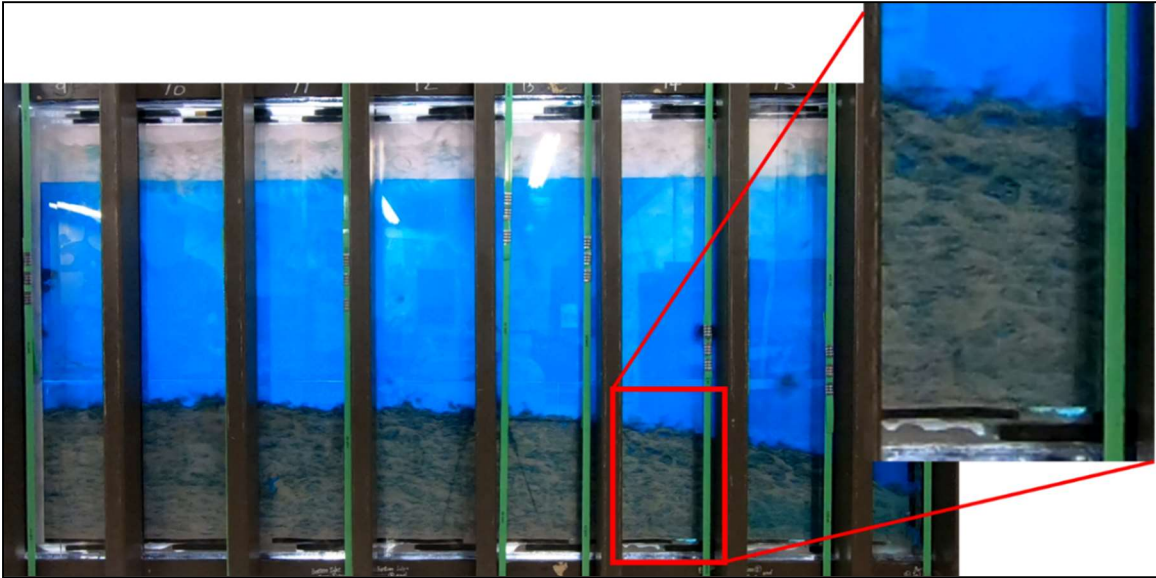
Figure 50. Settled fiber-proppant-agglomerate showing the laminated layers that can act as conduit for the fluid flow. (0.1 wt. % guar, 0.1 wt. % PGA (13 mm), 40/70 ceramic proppant)

Dynamic proppant transport with degradable fibers with less than 0.05 wt. % linear gel

Fig.51 shows the overall bar chart comparison of the fiber-proppant fluid dune characteristics. The below are the conclusions from the comparison study:

- For the test fluid with lower guar concentration, the dune covers from fracture top and bottom forming channels through which proppant-fiber clusters are transported.

- The concentration of fiber required to create high dune is more than 0.1wt. % for 0.4 in. slot while it is several times smaller for 0.2 in. slot.
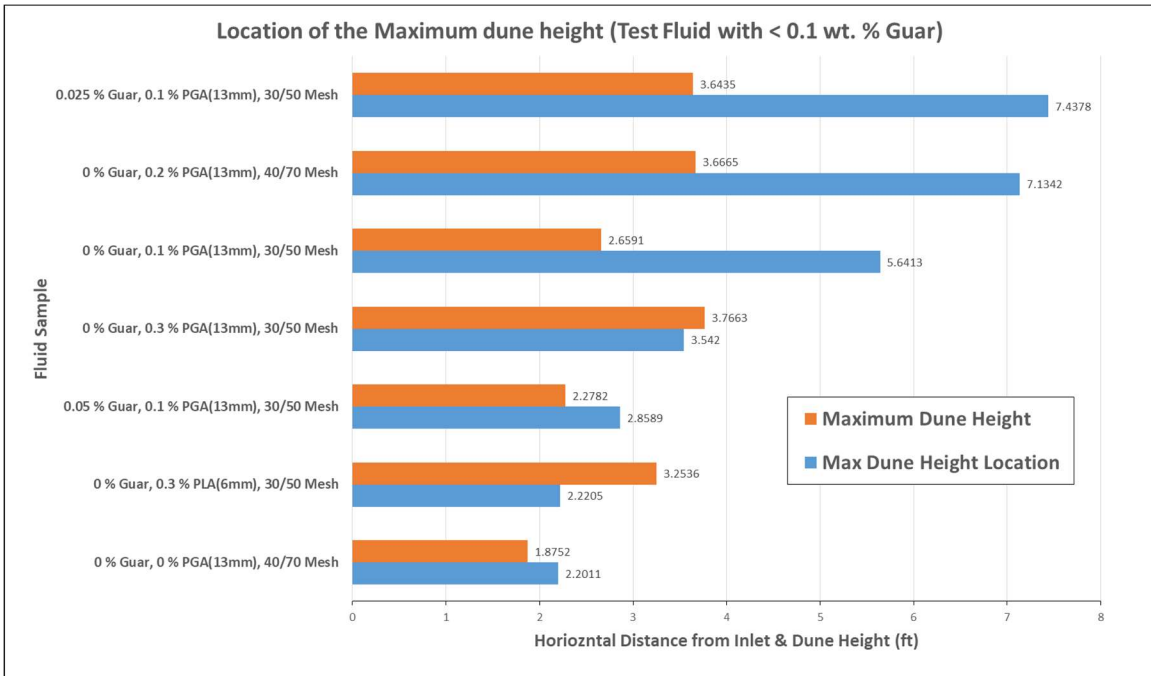
Figure 51. Proppant dune characteristic comparison of the test fluid samples containing less than 0.05 wt. % guar.

Fig. 52 and **53** show the fiber-proppant-flocculation that forms when the test fluid does not contain any guar gum as viscosifier. There are many fiber-proppant islands that are in suspension due to the frictional forces holding these proppant-fiber clusters. Further inspection shows very large void areas between the proppant-fiber packs. These voids will act as a high conductive pathway for the hydrocarbons to flow after the fibers are turned into acid after fracture closure.

Figure 52. Fiber-proppant-flocculation showing the random suspended islands. (0 wt. % guar, 0.3 wt. % PGA (13 mm), 30/50 ceramic proppant).
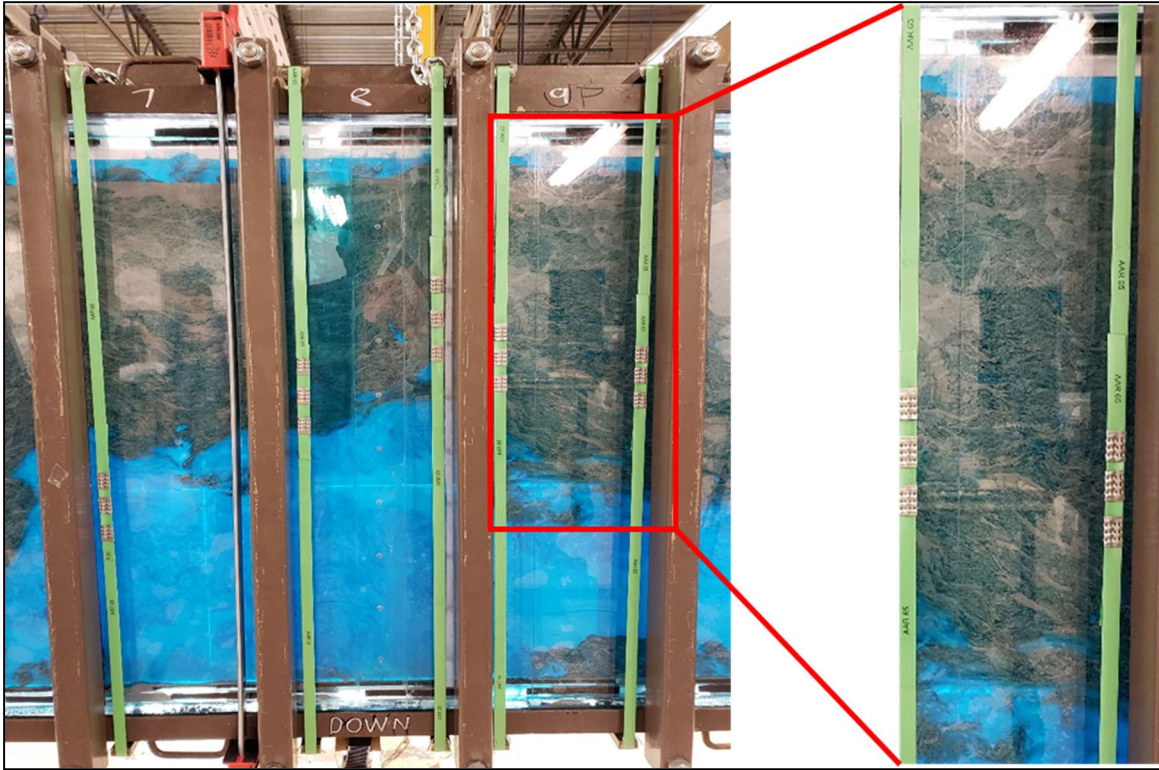
Figure 53. Fiber-proppant-flocculation showing the high conductive suspended proppant pack. (0 wt. % guar, 0.3 wt. % PGA (13 mm), 30/50 ceramic proppant).

CHAPTER V

ANALYIS AND SIMULATION STUDY

Background of StimPlan software

The numerical simulation study is done to verify and analyze the proppant

settlement behavior. For this, a well-established commercial hydraulic fracturing simulator,

StimPlan, is used. The StimPlan simulator has been widely used since 1985 to plan, design,

and evaluate the fracking operation (Kandlakunta, 2016). The StimPlan is a 3D numerical

simulator using Finite Element Method (FEM) provided for commercial use or academic

research by NSI Technologies, Inc. The StimPlan software provides the means to model

the complex hydraulic fracturing operation, such as, fracture height, width, tip screen-out,

proppant transport, multiple fractures, etc. (NSI Technologies, 2020). The ability to predict

the outcome and plan the fracture operation using the simulation is critical for successful

oil & gas extraction in shale reservoir. There are many published works employing the

StimPlan (Reeves, et al. 1993, Warpinski, et al. 1994, Kandlakunta, 2016, Smith, et al.

2001, Britt, et al. 2001, Sherif, 2018).

According to Yue, et al. (2019), the fracture height growth is one of the most

critical aspect in successful fracking operation as the net pay coverage and the fracture

height containment directly affects the hydrocarbon production. In their study, the

importance of the modulus contrast on the fracture growth is studied using the finite

element model. Sherif (2018) used StimPlan to come up with an optimum fracture

operation for the Nubain tight sandstone formation in Libya. In the study, thirteen different

fracture designs are evaluated with actual logs and well configurations. The comparison of

the fracture geometry and the dimensionless fracture conductivity as the results from the

simulation enabled the researcher to figure out which fluid composition and pumping

schedule would yield optimum hydrocarbon production.

In large, the StimPlan solves the following two equations as shown in **Eq. 6** and

Eq.7 simultaneously. **Eq. 6** is a volumetric conservation equation in the fluid and proppant

calculation in relation to the fracture geometry, the equation is solved by a finite difference

method. **Eq. 7** calculates the fracture width related to the stiffness matrix, pressure and the

in-situ stress using finite element method (FEM).

$$\frac{\partial V_f}{\partial t} + \Delta_x q_x + \Delta_z q_z = q_p - q_l \tag{6}$$

$$[K_{ij}][w_{hj}] = [p - \sigma]_i \tag{7}$$

The simulator couples the pressure and the volumetric flow rates through the following

equations (**Eqs. 8, 9, 10**) to define the fluid transport in large.

$$2\left(\frac{4n'+2}{n'}\right)n'\frac{\mu}{w^2}f(V_{prop})q_x = -\frac{\partial p}{\partial x}A_x \tag{8}$$

$$2\left(\frac{4n'+2}{n'}\right)n'\frac{\mu}{w^2}f(V_{prop})q_z = -\frac{\partial p}{\partial x}A_z \tag{9}$$

$$\mu = K\dot{\gamma}^{n'} \tag{10}$$

For the proppant suspension and settlement, the modified Stoke's law is employed

by the simulator as shown in **Eqs. 11, 12, and 13**. The only difference with the general

Stoke's law is the correction factor. The correction factor is included to account for the

hindered settling depending on different fluid system and the variation of the proppant

concentration. For the linear gel and borate cross link gels, the correction factor stays as one (NSI technology,2020). For our experimental study, the normalized correction factor according to the fall rate that is obtained from the experiment is used.

$$v_t = C_{correction} \frac{g(\rho_p - \rho_f)d_p^2}{18\mu_a} \text{, for } N_{Re} \leq 2 \text{ (Stokes-law region)} \tag{11}$$

$$v_t = C_{correction} \frac{20.34(\rho_p - \rho_f)^{0.71} d_p^{1.14}}{\rho_f^{0.29} \mu_a^{0.43}} \text{ for } 2 < N_{Re} \leq 500 \text{ (Intermediate region)} \tag{12}$$

$$v_t = C_{correction} 1.74 \sqrt{\frac{g(\rho_p - \rho_f)d_p}{\rho_f}} \text{ for } 2 < N_{Re} \leq 500 \text{ (Newton's-law region)} \tag{13}$$

In large, the StimPlan tracks the fracture fluid and proppant by accounting the total volumes pumped and the volumes leaked into the reservoir with the volume conservation equation. The interaction between the proppants and the fluids is accounted with the force equation, **Eq. 14,** as shown below along with the Stoke's equation. The force equation is function of the fluid density, ρ_l, relative velocity of the fluid and particle, v_r, and the frontal area of the particle, A_p. The drag coefficient, C_D, is calculated with **Eq. 15**, where gravitational force, g, terminal velocity, v_t, particle diameter, d_s, and the fluid and particle density, ρ_l, ρ_s.

$$F = C_D \frac{1}{2} \rho_l v_r^2 A_p \tag{14}$$

$$C_D = \frac{4}{3} g \frac{d_s}{v_t^2} \frac{\rho_s - \rho_l}{\rho_l} \tag{15}$$

The simulator recognizes that the proppants get transported along the fracture length and settle to create the proppant beds as the fracture fluids travels along the fracture. As the proppant accumulates on the bottom of the fracture, the accumulation is tracked with **Eq. 16** by the StimPlan. The equation tracks the accumulation of the proppant by accounting for the terminal velocity of the proppant, and proppant volume fraction over time with the conservation of volume function. The terminal settling velocity in **Eqs. 11** to **13** are adjusted by the proppant concentration effects; the simulation recognizes that the increase in proppant concentration decreases the terminal settling velocity of the proppants, and the simulation adjusts accordingly following Novotny, 1977. The following Eq. 16 is used to calculate the growth of proppant bed.

$$\frac{dH_{bed}}{dt} = v_t \alpha_p \qquad\qquad (16)$$

In summary, the simulator tracks and accounts the proppant and fluid with the volume conservation equation. And the proppant movement and settling is detailed by the modified Stoke's equation, force equation between the proppants, and the equations to account for the proppant concentration on the settling terminal velocity. When the fiber is introduced, the simulator is limited in its ability to account for the force interactions that comes from the fibers and proppants. There is no published literature that accounts for fibers with proppant interaction in the oil & gas industry applicable to the Stoke's correction factor. Thus, the correction factors derived from the static fall tests using fiber/proppant slurry performed in this work are used in the simulator. In the case of modified Stoke's law, the smaller correction factor represents slowed proppant settlement.

Fig. 54 shows the normalized correction factors from the static settlement experiments. The correction factor is plotted for three different proppant concentrations of 0.5, 1, and 4 lb/gal. Each plot shows the change in the correction factor according to the fiber and guar concentrations. The effect of the guar concentration in the absence of fiber shows that the correction factor decreases as the proppant concentration increases. This is due to the hindered settling; decrease in proppant settling velocity with increase in proppant concentration, which has been studied extensively by McMechan, et al. (1991). In all cases, the correction factor becomes smaller as the fiber concentration increases. It should be noted that when the fibers are introduced at the high proppant concentration of 4 lb/gal, the decrease in the correction factor is not as exponential when compared to the fluids with the lower concentration proppants. Note that the correction factor is 1 if the proppant fall rate obeys the ideal Stoke's law.
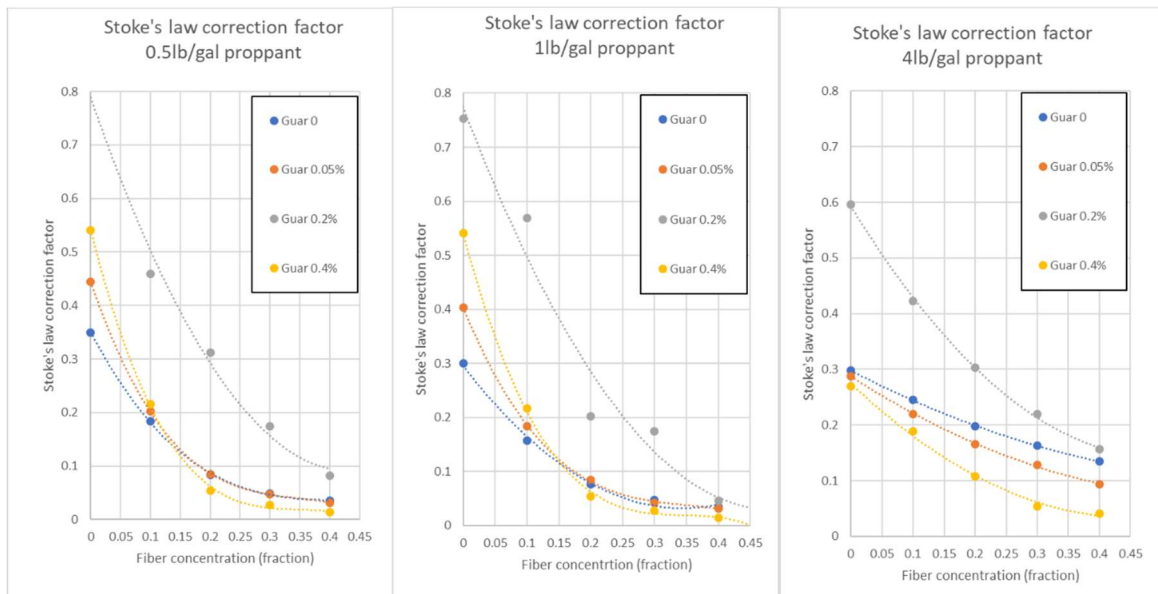
Figure 54. Normalized correction factors from fall rate tests where the apparent viscosity @300 rpm is 1, 1.5, 3.8, 7.5, and 22 cp for guar 0, 0.05, 0.1, 0.2, and 0.4 wt % at room temperature.

Simulation study models

The first model to simulate and compare is the vertical well with a single vertical fracture propagation as shown below.

Case I: A single vertical fracture propagation from a vertical well (conventional reservoir)

- **Reservoir:**
  Pay depth: 2150-2450ft, Initial reservoir pressure: 1500psi, Current reservoir pressure: 1000psi, Bottomhole flowing Pressure: 500psi, Sand formation, Porosity: 0.15, permeability: 5 md, rock compressibility: 1.7×10^{-6} 1/psi, oil reservoir with 25.7API gravity, Bottomhole reservoir temperature: 200°F.
- **Well data:**
  Treatment through tubing, vertical well, Borehole diameter=8.5";
  Casing: 7" OD, 6.366" ID, 0~2500 ft TVD;
  Tubing: 4.5 OD, 4.052" ID, 0~2300ft TVD;
  Fracture initiation: 2300-2400ft, with 6 shot/ft.
- **Geologic Layer Data:**
  Layer I: 1860 psi at 2000 ft TVD and 1860 psi at 2200 ft TVD with 0.8 psi/ft overburden;
  Layer II: 1540 psi at 2200 ft TVD and 1750 psi at 2500 ft TVD with 0.7 psi/ft overburden;
  Layer III: 2000 psi at 2500 ft TVD with 0.8 psi/ft overburden;
  Young's modulus: 3×10^6 psi, Poisson's ratio: 0.2, fracture toughness: 2000 $psi\sqrt{in}$.
- **Slurry Data:**
  Fluid Data: Fluid loss coefficient= 0.0005 ft/$\sqrt{min}$, 0.1 wt. % guar, K'= 0.000134, n'= 0.9.
  Proppant data: 30/50 mesh ceramic proppant, density=$2.6 g/cm^3$ ($1.57\ g/cm^3$ as bulk density). Proppant pack porosity: 0.35 without fiber and 0.4 with fiber;
  Pump schedule: pad= 20,000 gal with 30 BPM (pump time 15.9min), slurry injection 40,000 gal with 30 BPM (4 PPG proppant concentration, 32.8min.)

The large-scale experiments show that in the presence of fibers, void spaces of different sizes are created by the fiber-proppant-clusters, the void spaces maintain its shape even after the pump is shut down. It should be noted that the void spaces are created even

with small amount of fiber is used as seen from **Fig. 55.** Due to this observation from the experimental study, proppant pack porosity value of 0.4 is used for the simulation for the case with fibers, and proppant pack porosity value of 0.35 is used for the case without the fiber.
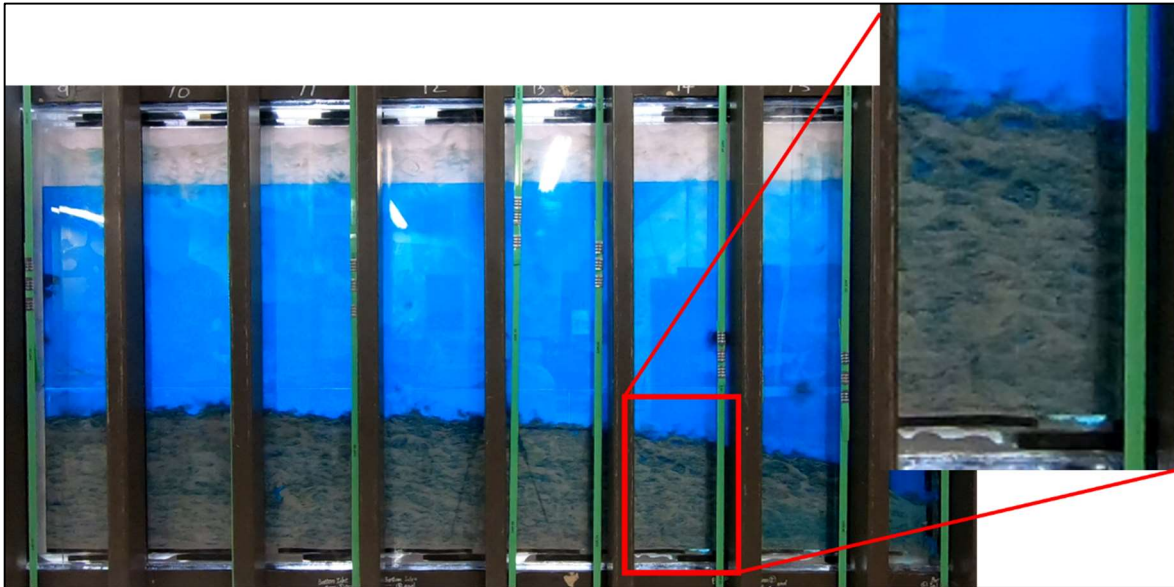
Figure 55. Fiber-proppant-clusters forming the laminated layers that can act as conduit for the fluid flow (0.1 wt.% guar, 0.1 wt. % PGA fiber (13 mm lengh), 40/70 ceramic proppant)

The following **Figs. 56** to **60** show the Case I simulation results with 7.5 cp fluid, and 4 lb/gal proppant in the absence of fibers. The simulation results show the fracture width and proppant concentration at the end of pumping and the proppant coverage after the closure. The use of 30/50 mesh ceramic proppant shows the proppant being well distributed up to the fracture tip.
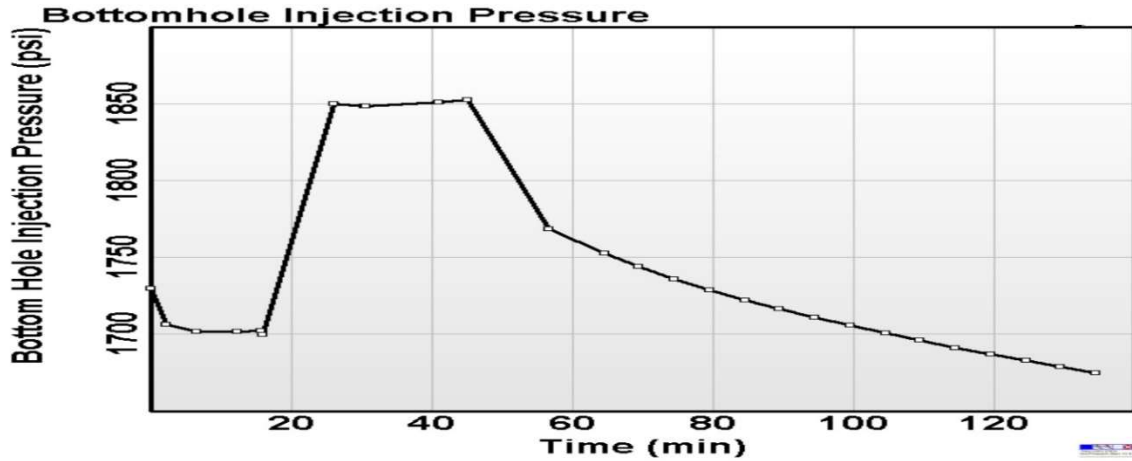
Figure 56. Bottomhole injection pressure showing the decrease in pressure as the fracture propagates after 40 minutes (Case I without fiber).
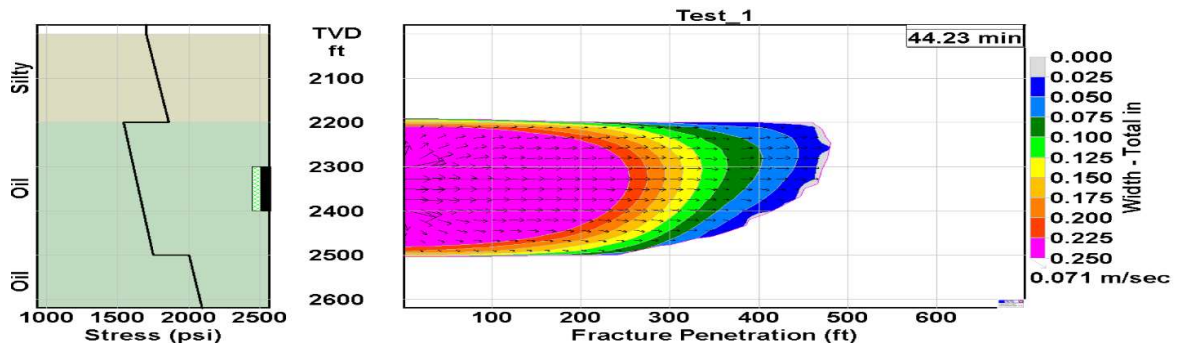
Figure 57. Growth of fracture width at the end of pumping (Case I without fiber).
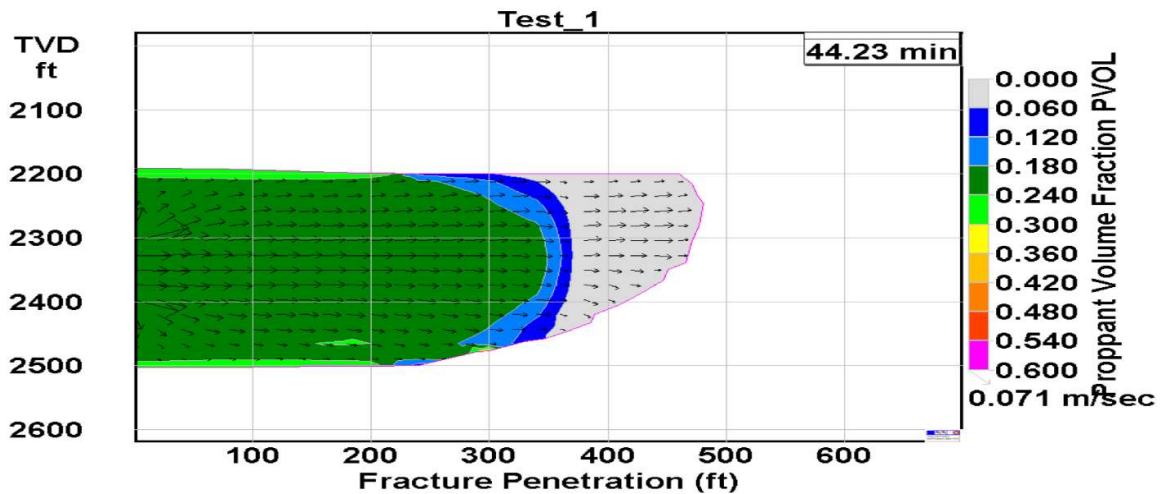
Figure 58 Proppant volume fraction at the end of pumping (Case I without fiber).
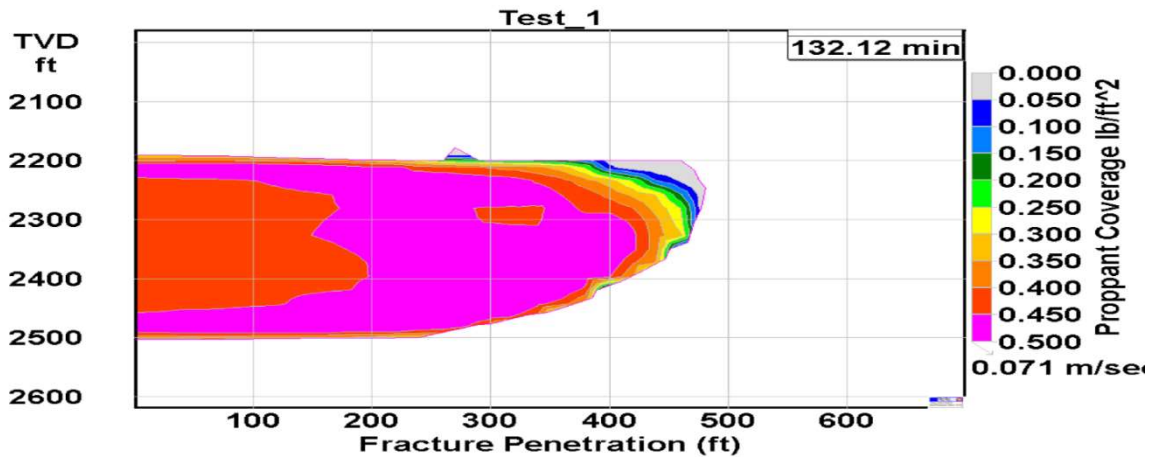
Figure 59. Proppant coverage 88 minutes after the pump is shut down (Case I without fiber).
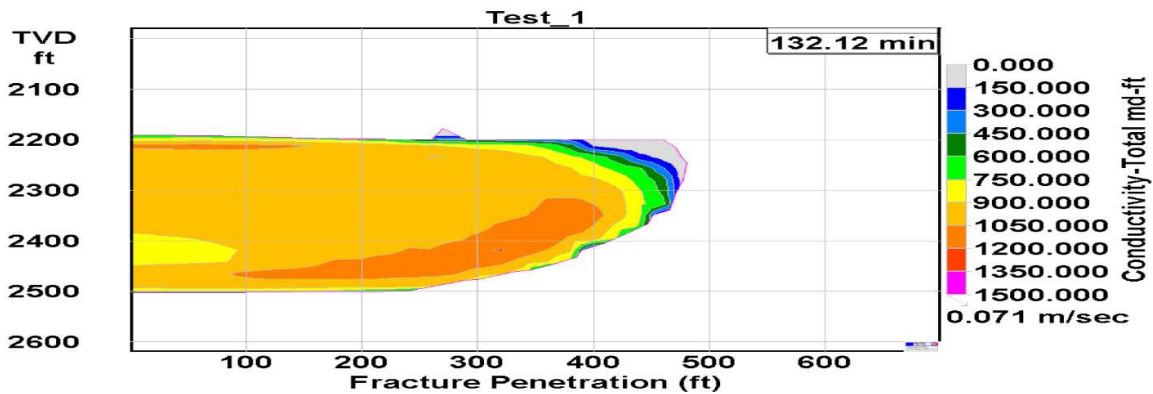
Figure 60. Conductivity, md-ft, 88 minutes after the pump is shut down (Case I without fiber).

Figs. 61 to **64** show the Case I simulation result with 7.5 cp fluid, and 4 lb/gal proppant in the presence of fibers, fiber of 0.3 wt. % is used for the simulation. Comparing simulation result with and without the fibers, it shows that the width is the same while the proppant concentration at the end of pumping and the proppant coverage after fracture closure are slightly better with the presence of fibers. The merit of using fiber is shown with the simulation run as it improves the fracture conductivity as the void space is created from fiber-proppant clusters as it is shown in **Fig. 64** from the experiments.

77
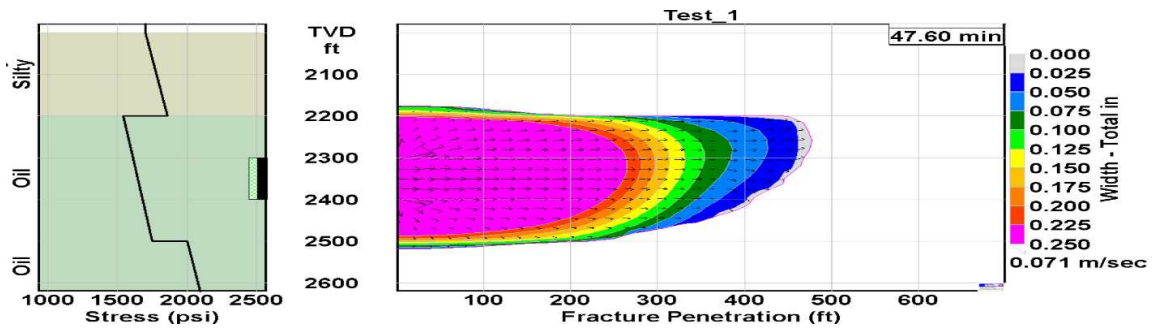
Figure 61. Growth of fracture width at the end of pumping (Case I with 0.3 wt. % fiber).
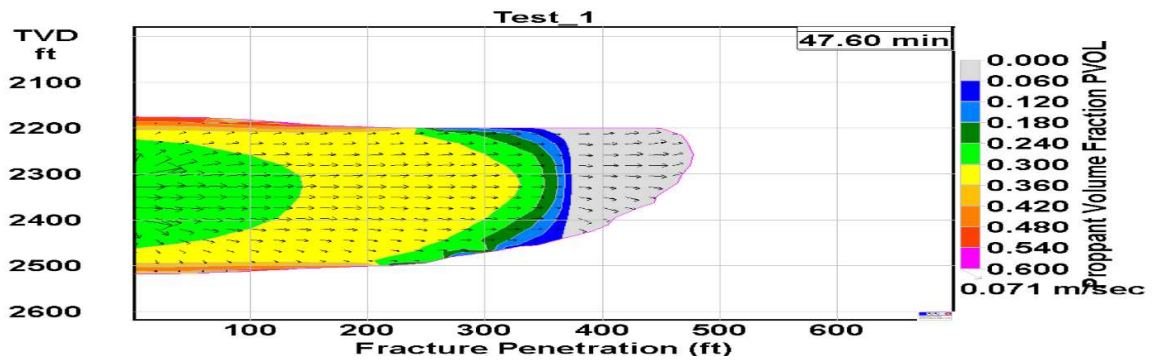
Figure 62. Proppant volume fraction at the end of pumping (Case I with 0.3 wt. % fiber).
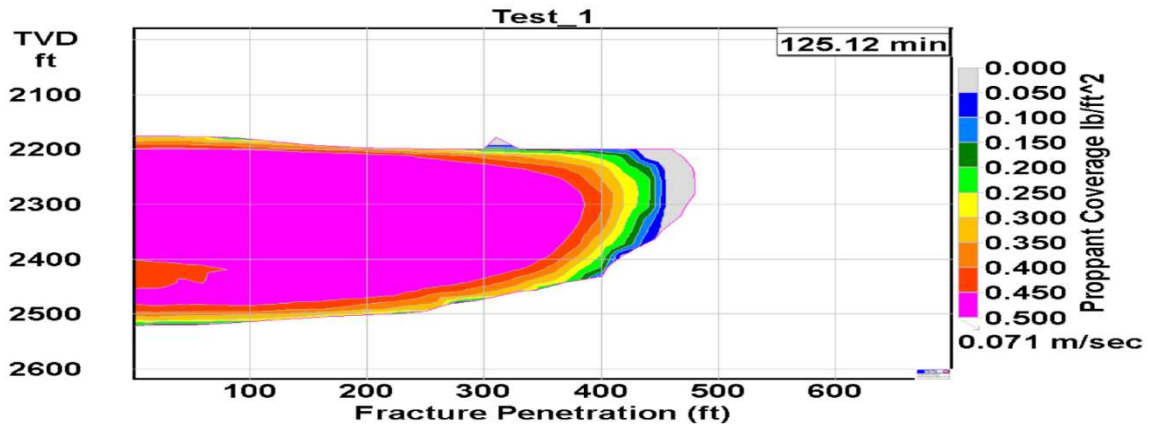
Figure 63. Proppant coverage 78 minutes after the pump is shut down (Case I with 0.3 wt. % fiber).
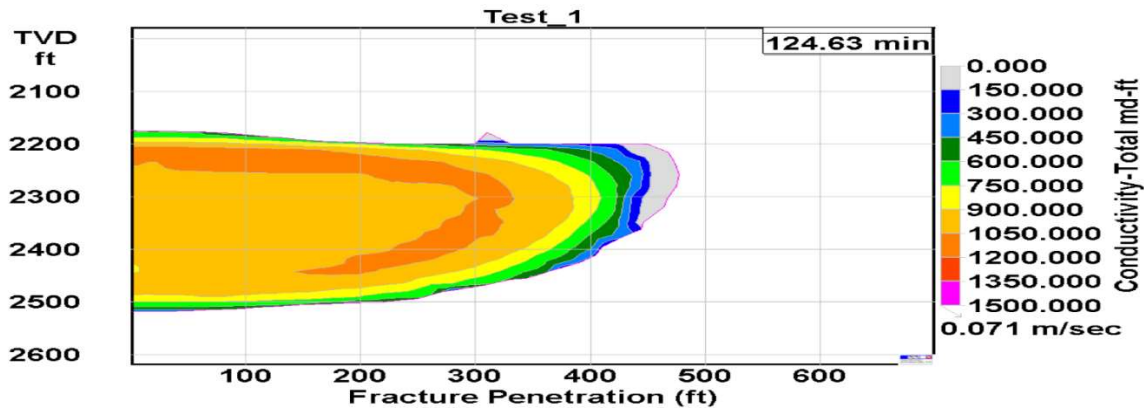
Figure 64. Conductivity, md-ft, 78 minutes after the pump is shut down (Case I with 0.3 wt. % fiber).

The second model to simulate and compare is a single horizontal well (unconventional reservoir) with a single vertical fracture propagation with the following details below.

Case II: A single vertical fracture propagation from a horizontal well (unconventional reservoir)

- **Reservoir:**
  Pay depth: 2150-2450ft, Initial reservoir pressure: 1500psi, Current reservoir pressure: 1000psi, Bottomhole Flowing Pressure: 500psi, Sand formation, Porosity: 0.15, permeability: 5 md, rock compressibility: 1.7×10^{-6} 1/psi, oil reservoir with 40 API gravity, Bottomhole reservoir temperature: 200°F.

- **Well data:**
  Treatment through tubing, horizontal well, Borehole diameter=8.5";
  Casing: 7" OD, 6.366" ID, 0~2500 ft TVD, Horizontal lateral length: 1100 ft kick-off at 2400 ft TVD
  Tubing: 4.5 OD, 4.052" ID, 0~2400ft TVD;
  Fracture initiation: 2550 - 2555ft, with 6 shot/ft.

- **Geologic Layer Data:**
  Layer I: 1710 psi at 1900 ft TVD and 1890 psi at 2100 ft TVD with 0.9 psi/ft overburden;
  Layer II: 1470 psi at 2100 ft TVD and 1820 psi at 2600 ft TVD with 0.7 psi/ft overburden;
  Layer III: 2340 psi at 2600 ft TVD with 0.9 psi/ft overburden;
  Young's modulus: 3×10^{6} psi, Poisson's ratio: 0.2, fracture toughness: 2000 $psi\sqrt{in}$.

- **Slurry Data:**
  Fluid Data: Fluid loss coefficient= 0.0005 ft/$\sqrt{min}$, 0.1 wt. % guar, K'= 0.000134, n'= 0.9.
  Proppant data: 30/50 mesh ceramic proppant, density=2.6g/cm^3 (1.57 g/cm^3 as bulk density). Proppant pack porosity: 0.35 without fiber and 0.4 with fiber; Pump schedule: pad= 20,000 gal with 30 BPM (pump time 15.9min), slurry injection 60,000 gal with 30 BPM (4 PPG proppant concentration, pump time 47.7min.)

The case II is simulated, and the results are illustrated from **Figs 65** to **68**. In this case, 30/50 mesh ceramic proppant with 7.5 cp viscosity guar fluid is used without presence of fibers. The figures show the fracture width and proppant concentration at the end of pumping and the proppant coverage after closure. The use of 30/50 mesh ceramic proppant enabled the proppant distribution up to the fracture tip.

Figure 65. Bottomhole injection pressure for the Case II.
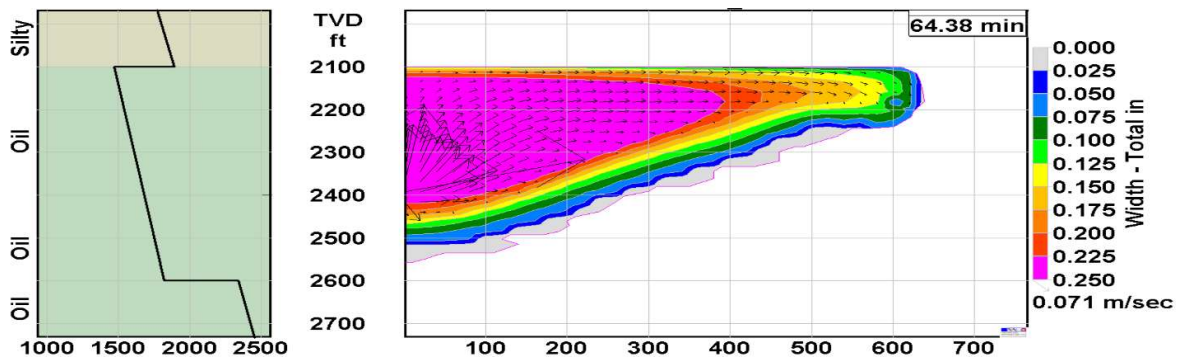
Figure 66. Fracture width at the end of pumping (Case 2 without fiber, with 7.5 cp viscosity at the reservoir condition).

Figure 67. Proppant coverage after fracture closure (Case 2 without fiber, with 7.5 cp viscosity at the reservoir condition).

Figure 68. Propped fracture conductivity after fracture closure (Case 2 without fiber, with 7.5 cp viscosity at the reservoir condition).

Figs. 69 to **71** show a simulation with 7.5 cp frac fluid and 4 lb/gal proppant with 0.3 wt. % fiber under Case 2 condition. The proppant concentration distribution and proppant coverage are slightly better with fiber than the simulation case without fiber. The proppant conductivity is also better with fibers since the pack porosity is increased with scattered voids due to the presence of fiber-proppant clusters.

81
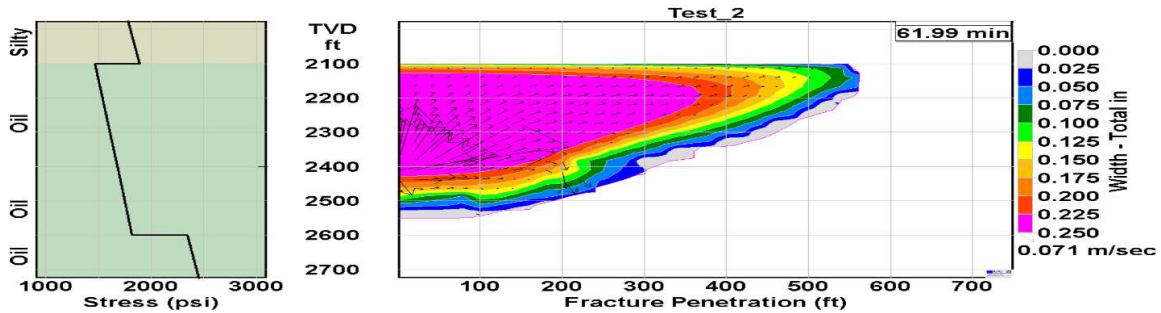
Figure 69. Fracture width at the end of pumping (Case 2 with 0.3 wt. % fiber, with 7.5 cp viscosity at the reservoir condition).

Figure 70. Proppant coverage after fracture closure (Case 2 with 0.3 wt. % fiber, with 7.5 cp viscosity at the reservoir condition).

Figure 71. Propped fracture conductivity after fracture closure (Case 2 with 0.3 wt. % fiber, with 7.5 cp viscosity at the reservoir condition).

The third model to simulate and compare is a single horizontal well (unconventional reservoir) with a single vertical fracture propagation with the following details below. This case differs from the case 2 on the fracturing fluid and proppant size used.

Case 3: A single vertical fracture propagation from a horizontal well (unconventional reservoir)

- **Reservoir:**
  Same as the case 2.
- **Well data:**
  Same as the Case 2.
- **Geologic Layer Data:**
  Same as the Case 2.
- **Slurry Data:**
  Fluid Data: Fluid loss coefficient= 0.0005 ft/$\sqrt{min}$, 0.1 wt. % guar, K'= 0.000134, n'= 0.9.
  Proppant data: 40/70 mesh ceramic proppant, density=2.6g/cm^3 (1.57 g/cm^3 as bulk density). Proppant pack porosity: 0.35 without fiber and 0.4 with fiber; Pump schedule: pad= 20,000 gal with 30 BPM (pump time 14.3 min), slurry injection 60,000 gal with 30 BPM (1 PPG proppant concentration, pump time 42.9 min.)

Figs. 72 to **76** show the simulation run with frac fluid with 3 cp and 1 lb/gal proppant without fiber under Case 3 condition. The figures show the fracture width and proppant concentration at the end of pumping and the proppant coverage after fracture closure. Since 40/70 mesh proppant is used, the proppant is well distributed up to the fracture tip during injection. However, after shutting down the pump, the proppant is settled to the bottom of the fracture creating proppant dune; using 1 ppg proppant lead to poor proppant coverage.
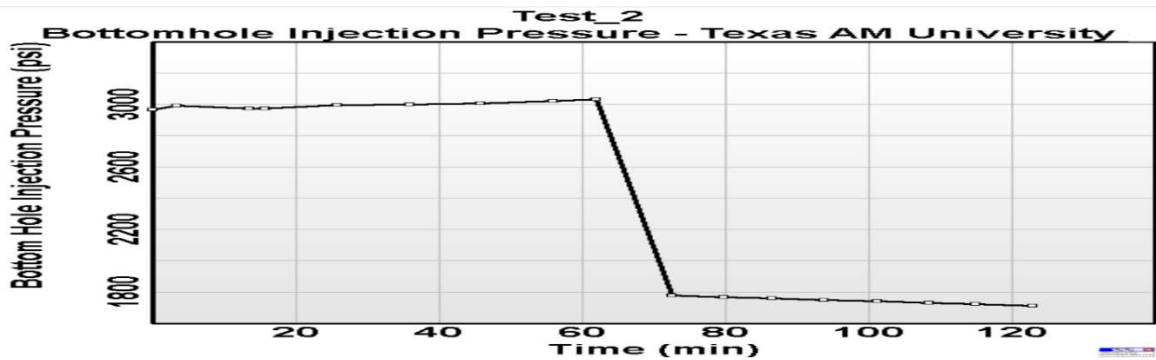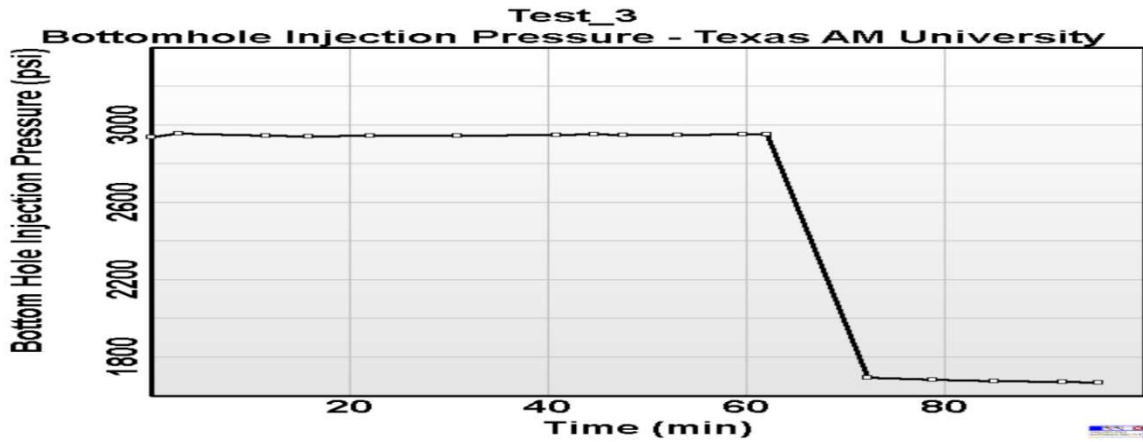
**Figure 72. Bottomhole injection pressure for the Case 3.**
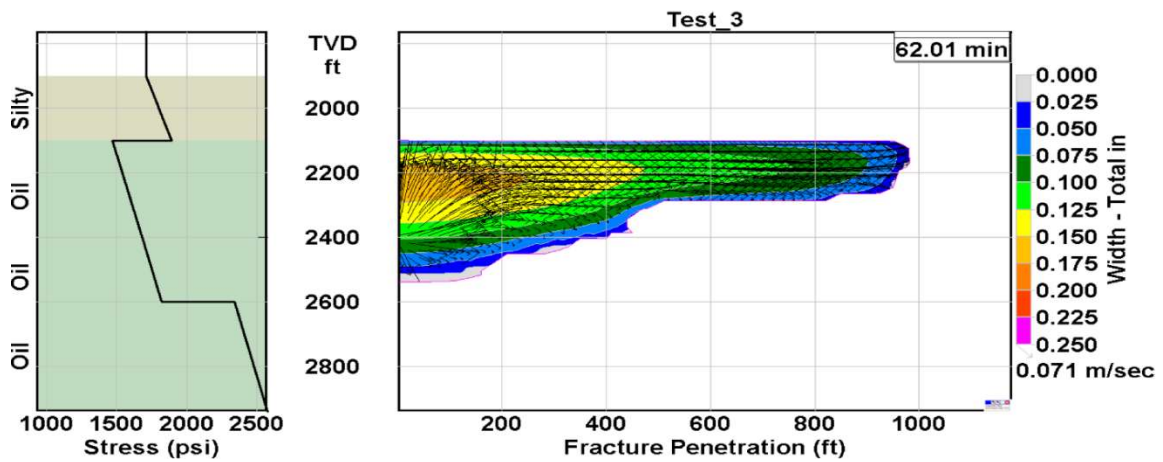
Figure 73. Fracture width at the end of pumping (Case 3 without fiber, with 3.0 cp viscosity at the reservoir condition).
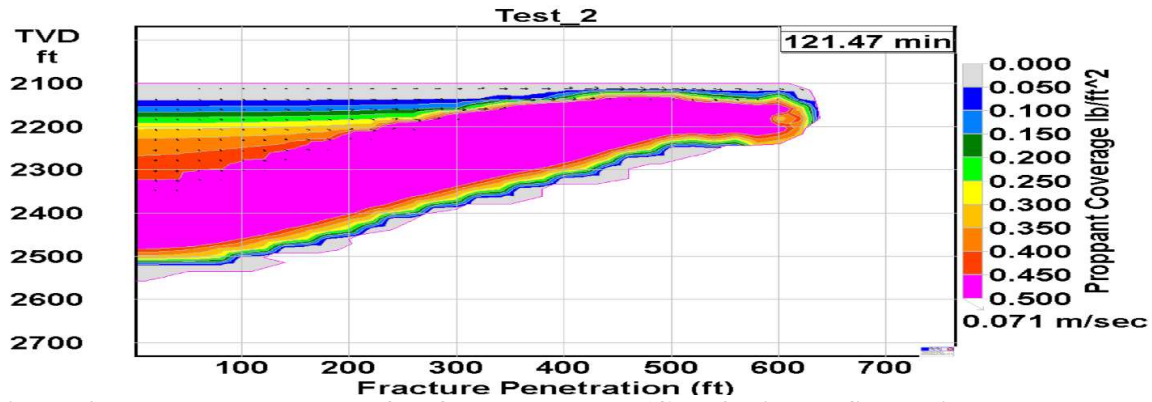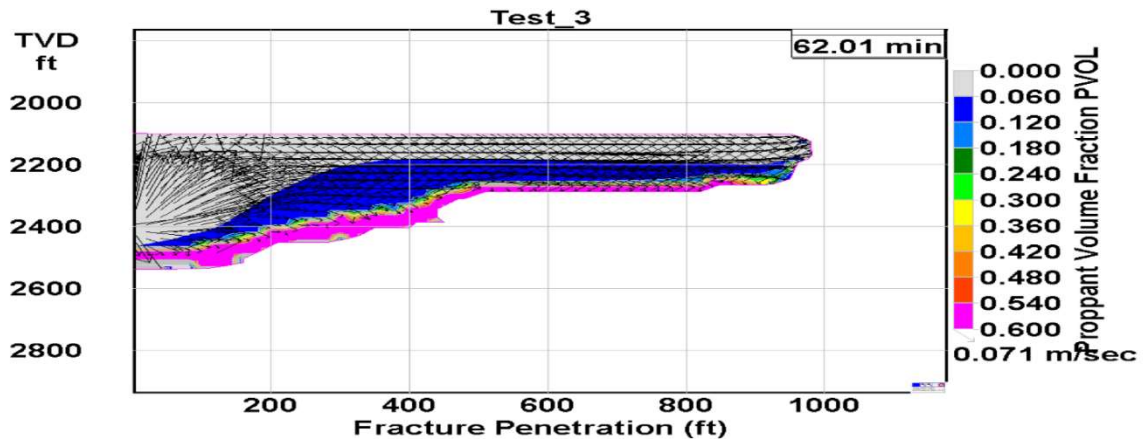

Figure 74. Proppant concentration at the end of pumping (Case 3 without fiber, with 3.0 cp viscosity at the reservoir condition).

84
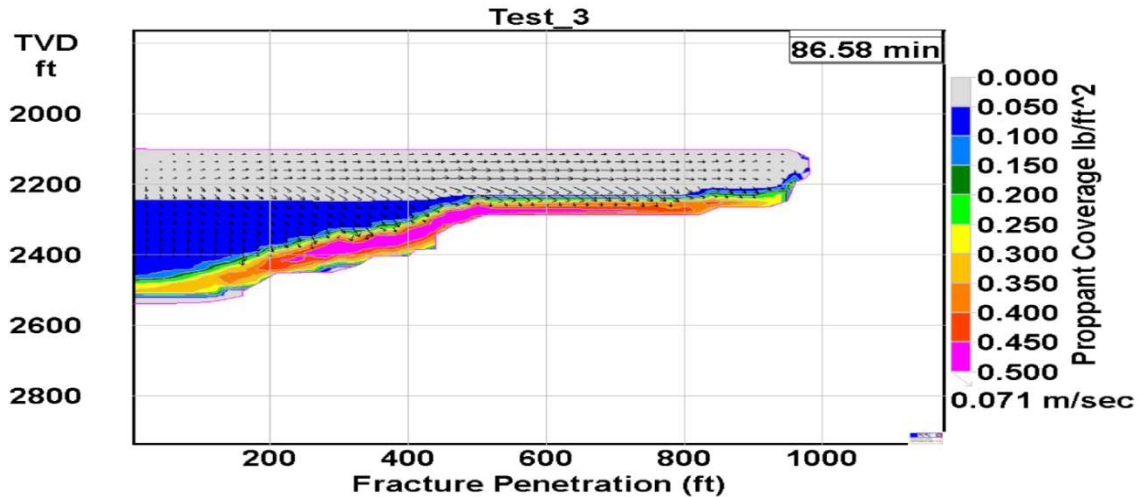
Figure 75. Proppant coverage after fracture closure (Case 3 without fiber, with 3.0 cp viscosity at the reservoir condition).
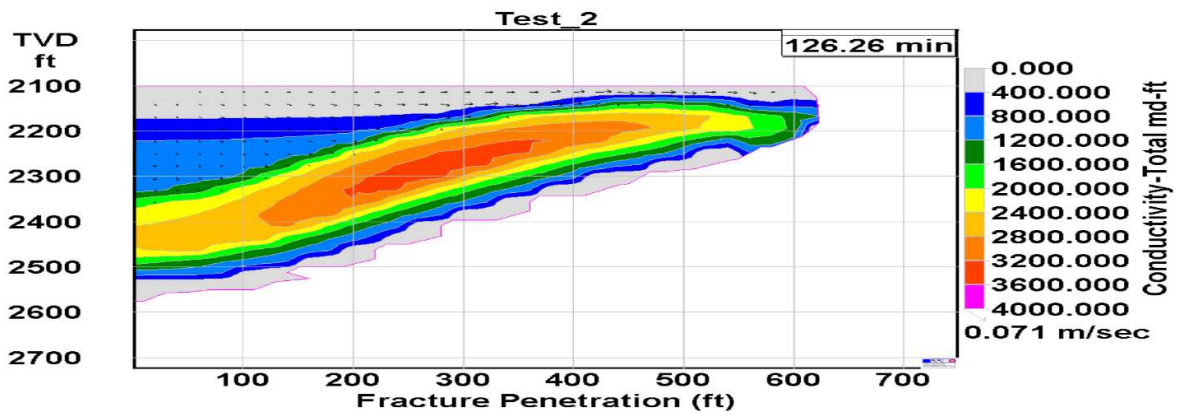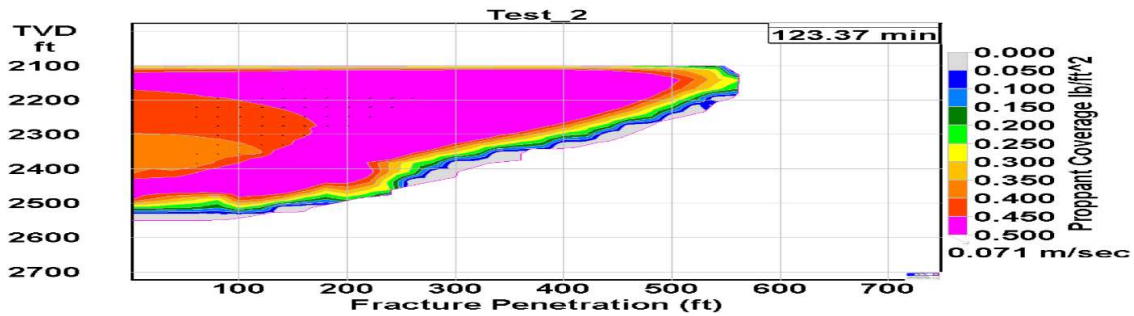

Figure 76 Proppant fracture conductivity after fracture closure (Case 3 without fiber, with 3.0 cp viscosity at the reservoir condition).

Figs. 77 to **82** show the simulation runs with 3 cp frac fluid and 1 lb/gal proppant with 0.2 wt. % and 0.5 wt. % fiber, respectively. The fracture width is approximately the same if fiber concentration is less than 0.2 (comparing with **Figs. 73** and **77**). The settled proppants prevent fracture propagation downwards so that fracture length becomes large. However, if the fiber concentration is as large as 0.5 wt. %, the proppant does not settle. Therefore, fracture width shown in **Fig. 80** is more uniform than those shown in **Figs. 73**

85

and **77**, resulting in shorter fracture. The proppant concentration and coverage distribution improved as the fiber concentration increases. If the fiber concentration is as much as 0.5 wt. %, the entire fracture surface is covered by proppant. The proppant coverage figure (**Fig. 81**) shows the proppant covering the entire fracture surface indicating an excellent proppant transport with 0.5 % of fiber concentration. The proppant distribution covering the entire surface can be observed with high fiber concentration as the experiment shows in **Fig. 83** with zero guar. The proppant-fiber clusters are covering entire fracture surface even several minutes after the pump is shut down.
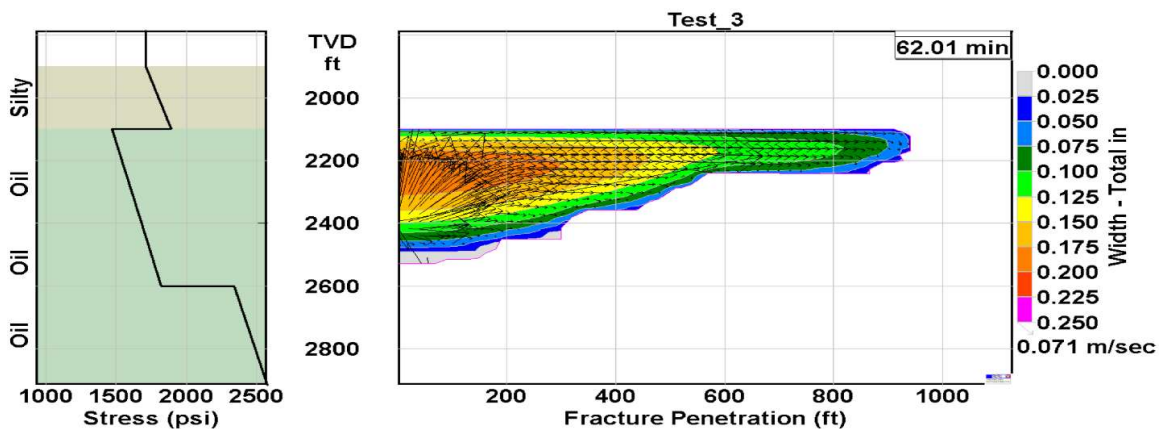
Figure 77. Fracture width after fracture closure (Case 3 with 0.2 wt. % fiber, with 3.0 cp viscosity at the reservoir condition).
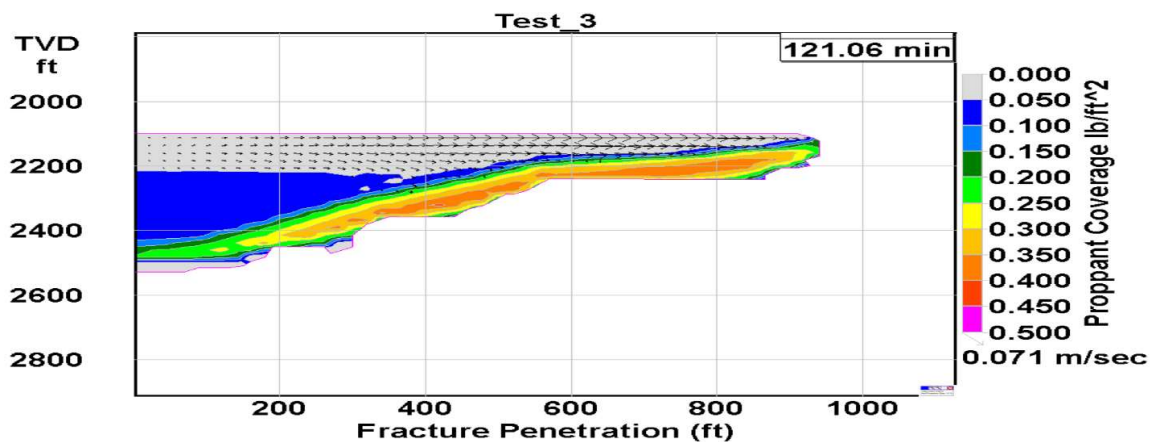
Figure 78. Proppant coverage after fracture closure (Case 3 with 0.2 wt. % fiber, with 3.0 cp viscosity at the reservoir condition).
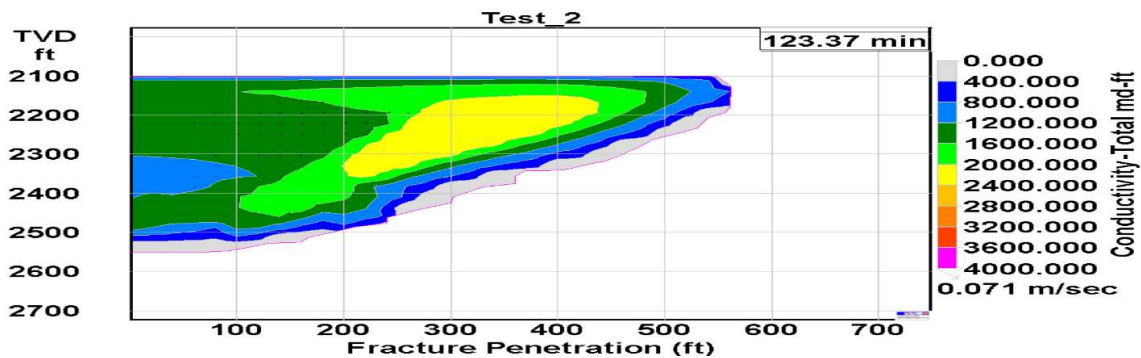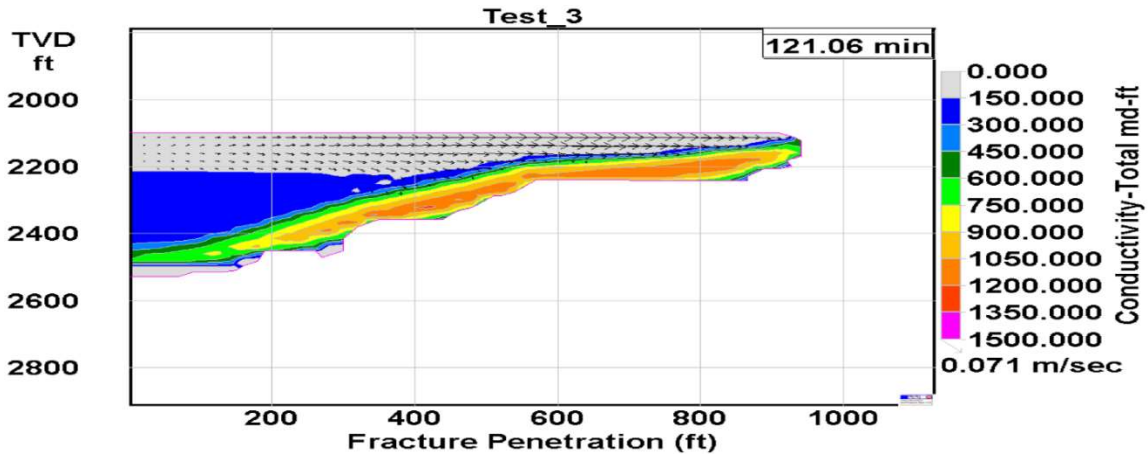
Figure 79. Conductivity after fracture closure (Case 3 with 0.2 wt. % fiber, with 3.0 cp viscosity at the reservoir condition).
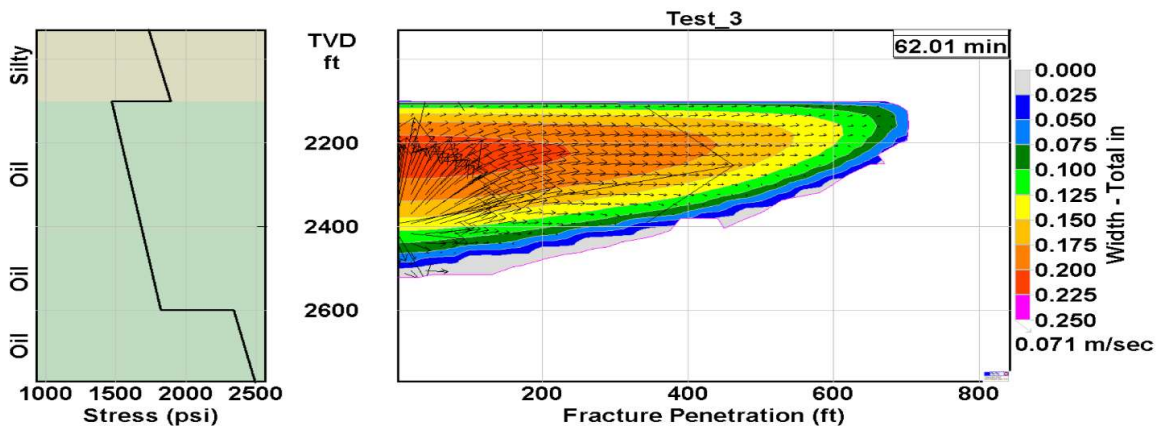
Figure 80. Fracture width after fracture closure (Case 3 with 0.5 wt. % fiber, with 3.0 cp viscosity at the reservoir condition).
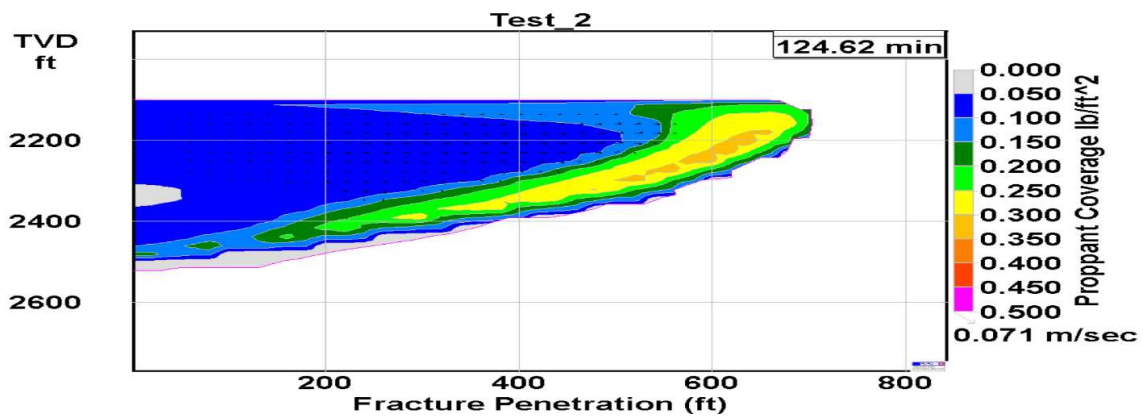
Figure 81. Proppant coverage after fracture closure (Case 3 with 0.5 wt. % fiber, with 3.0 cp viscosity at the reservoir condition).

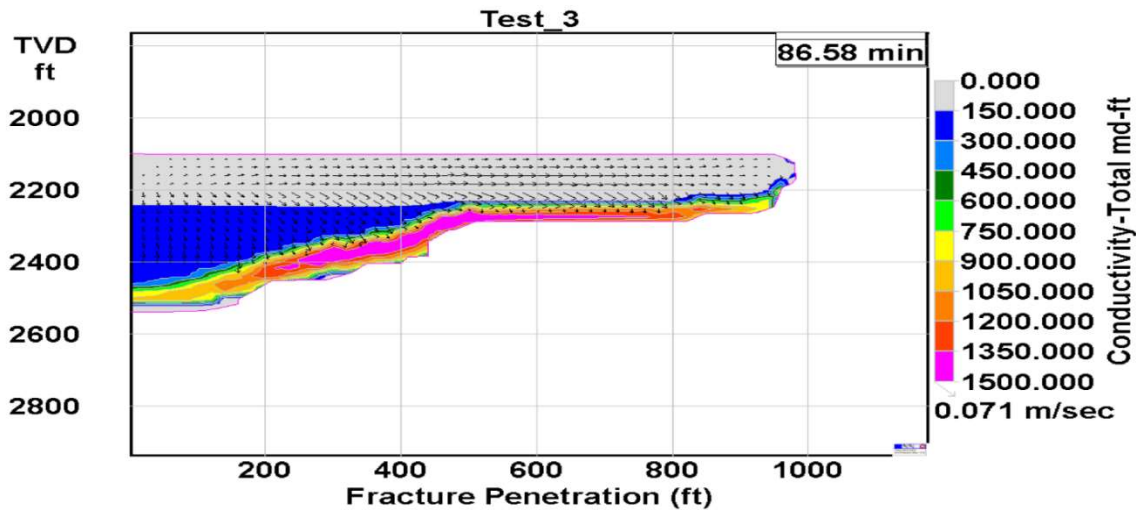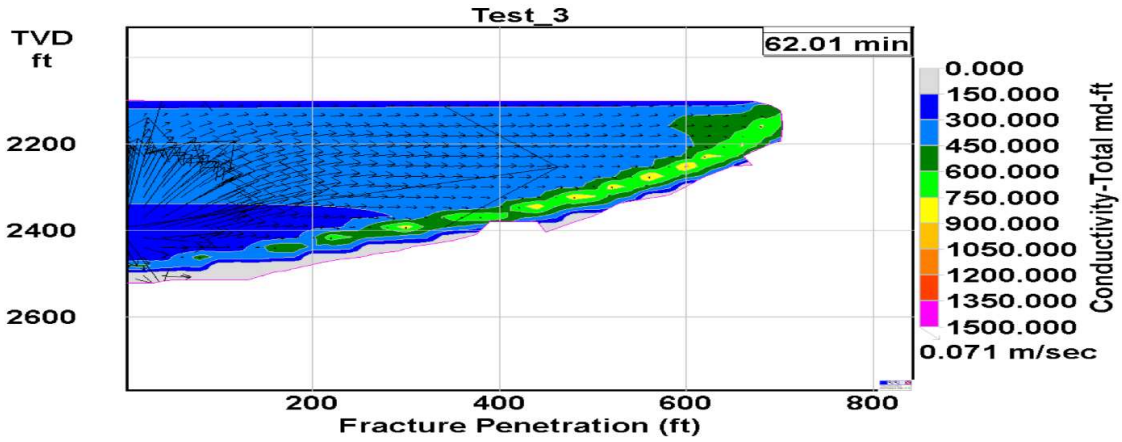**Figure 82. Proppant fracture conductivity after fracture closure (Case 3 with 0.5 wt. % fiber, with 3.0 cp viscosity at the reservoir condition).**
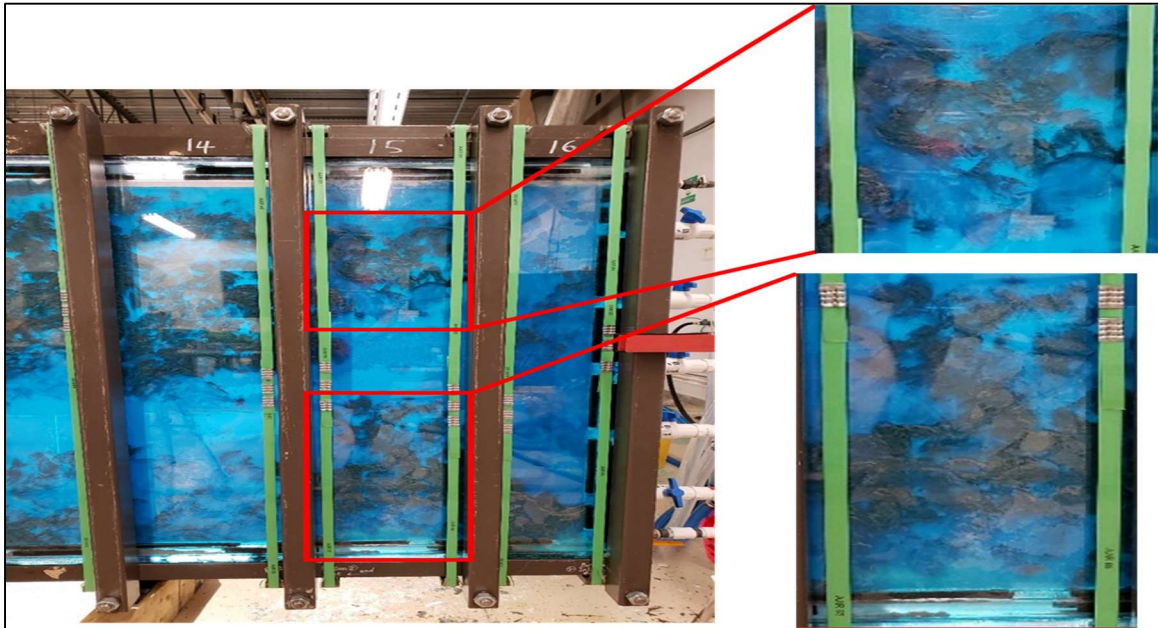
Figure 83. Fiber-proppant-flocculation showing the random suspended islands. (0 wt. % guar, 0.3 wt. % PGA (13 mm), 30/50 ceramic proppant).

The simulation results are largely consistent with the results of the large-scale dynamic proppant transport tests with some differences. Agreement between simulation and experimental results are as follows,

1. The inclusion of fibers results in increasing the proppant conductivity: both simulation and experiment results show that if the fluid viscosity exceeds 7.5 cp (16 lb/1000gal guar at room temperature, or 32 lb/1000gal at 200°F in-situ) and the proppant concentration exceeds 4 ppg, the proppant transport is equivalent for proppant size smaller than 20/40 mesh (both 30/50 and 40/70 mesh) with and without the fibers. However, the inclusion of fiber leads to fiber-proppant clustering which helps to create scattered voids within the proppant pack resulting in increased conductivity as the fiber degrades due to the hydrolysis after the fracture closure.

2. The inclusion of fibers improves proppant transport: both simulation and experiment using low viscous frac fluid as low as 3cp (8 lb/1000gal guar at room temperature, 16 lb/1000gal at 200°F in-situ), and low proppant concentration at 1 ppg shows the proppant covering entire fracture surface without much of falling. This results in a uniform proppant conductivity over the entire fracture surface.

Difference between simulation and experimental results

1. If fiber is included, rolling or gliding of proppant-fiber clusters occurred after settlement on the fracture bottom during the large-scale dynamic proppant transport experiments. Fiber-proppant clusters were swept away with flow once they were settled. This process was complex and this complex phenomenon could not be included in the simulated model.

2. If the viscosity of frac fluid is less than 1.6cp, and the proppant concentration is less than 1 lb/gal with 0.2-0.3% fiber concentration, the injected fluid with fiber and proppant flows through the previously injected fiber-proppant clusters forming fingers and channels. This flow process distributes proppant over entire fracture surface. This complex force interaction is not represented in the proppant-settlement equations used by the simulation model.

3. According to the simulation study, the fiber does not significantly affect the interwell pressure relation. However, it affects each fractures in the geometry; proppant settles early without the fiber, which leads to limited width growth and longer fracture length, whereas the fiber leads to wider width and shorter fracture length as more proppants are transported, leading to higher conductivity.

Three additional simulations are studied using different parameters that are attached in the Appendix B. The Appendix B-1 compares case 2 with lower injection rate for 3 fractures in a cluster. The Appendix B-2 compares with case 2 with different proppant size for 3 fractures in a cluster. The Appendix B-3 compares with case 3 but with multiple fractures as a cluster.

CHAPTER VI

CONCLUSIONS

An experimental study with various sizes of apparatus has been carried out to compare the performance of fiber in proppant transport. Mainly the fiber and guar concentrations are compared with respect to the transport mechanism. The results on the fiber performance from the experiment are used and compared with a well-known commercial software. The experiment and simulation results have some important implications in hydraulic fracturing with slickwater in the presence of fibers. The conclusions are summarized as below.

1. The static proppant settlement and the dynamic proppant transport tests in both small- and large-scale apparatus are recommended to study the proppant transport mechanisms. The static apparatus can be used to effectively examine the fall rate of the proppants. These data are required for a fracture propagation simulation model to evaluate proppant distribution after fracture closure. The large-scale dynamic proppant test is appropriate to study the proppant transport as the proppant transport includes complex fluid flow and solid interactions. It is important to check the difference between a simulation model and actual proppant transport.

2. Both fiber and guar may be used as a proppant transport agent. However, two distinct differences occur between them in the vertical settlement.

   (A) If guar is used without fiber, the fall rate is generally reduced as the guar concentration increases with proppant concentration. Only exception is that if

the proppant concentration exceeds a certain critical concentration, proppant clusters are formed which fall with significantly higher rate than surrounding uniform proppant slurry.

(B) If fiber is used with small guar concentration, the fiber concentration must be proportionally increased with proppant concentration to maintain the same proppant fall rate. Therefore, the fiber application is economically feasible if the proppant concentration is low.

(C) The total suspension of proppants is observed with 1 wt.% of fiber concentration for 4 ppg or less proppant independent of guar concentration, while linear gel without fiber can only slow down the settling velocity with a higher concentration.

3. The proppant transport mechanisms in the presence of fiber are distinctively different for the viscosity less than 1.6 cp and more than 4 cp. If the frac fluid has no guar (approximately 1.6 cp), the fiber-proppant clusters forms channels and flow path for the following fiber-proppant clusters to flow through at higher velocity. If the frac fluid has more than 0.1 wt. % guar concentration (approximately 4 cp), the fiber-proppant clusters flow laterally further with small fall rate without the channel formation.

4. The inclusion of degradable fiber enhances proppant transport and increase proppant pack conductivity even with limited amount of guar. Fiber-proppant-clusters are formed leading to significant reduction in fall rate. For unconventional

fracture operation, 30/50 or 40/70 mesh proppant may be used instead of more popular 100 mesh proppant as the fiber helps in reducing the fall rate. The settled fiber-proppant clusters form low density agglomerates with voids leading to higher conductivity as the fibers leading to higher productivity, and they are turned into liquid due to hydrolysis.

5. Both degradable PLA and PGA fibers may be used depending on the reservoir temperature. PGA normally dissolves within several hours while PLA dissolves within several days during the standard fracturing operations. PGA's higher tensile strength maintains its high strength with normal hydraulic fracturing operations. Proppant transport capability is enhanced for the low and high viscous frac fluids in the presence of fibers. Fiber length slightly larger than the maximum frac width is sufficient to form fiber-proppant clusters, although longer fibers are more effective.

6. The simulation results largely agree with the experiments as follows,

    (A) The inclusion of fibers results in increasing the proppant conductivity: both simulation and empirical results show that if the fluid viscosity exceeds 7.5 cp (16 lb/1000gal guar at room temperature, or 32 lb/1000gal at 200°F in-situ) and the proppant concentration exceeds 4 ppg, the proppant transport is equivalent with and without the fibers for proppant size smaller than 20/40 mesh (both 30/50 and 40/70 mesh). However, the inclusion of fiber lead to fiber-proppant clustering which helps to create scattered voids within the

proppant pack leading to increased conductivity as the fiber degrades due to the hydrolysis after the fracture closure.

(B) The inclusion of fibers improves proppant transport: both simulation and experiment using low viscous frac fluid as low as 3cp (8 lb/1000gal guar at room temperature, 16 lb/1000gal at 200°F in-situ), and low proppant concentration at 1 ppg shows the proppant covering entire fracture surface without much of falling. This results in a uniform proppant conductivity over the entire fracture surface.

(C) Although the fiber affects the width and fracture half length: inclusion of fiber leads to wider, shorter fracture. The inclusion of fiber does not affect the stress interference between the wells according to the simulation.

REFERENCES

Al-Muntasheri, G. A. (2014). A Critical Review of Hydraulic-Fracturing Fluids for Moderate-to Ultralow-Permeability Formations Over the Last Decade. SPE Prod & Oper 29 (4): 243– 260. *WOS: 000345288100002*.

Alotaibi, M. A., & Miskimins, J. L. (2015). *Slickwater proppant transport in complex fractures: new experimental findings & scalable correlation.* Paper presented at the SPE Annual Technical Conference and Exhibition.

Barati, R., & Liang, J. T. (2014). A review of fracturing fluid systems used for hydraulic fracturing of oil and gas wells. *Journal of Applied Polymer Science, 131*(16).

Barree, R., & Conway, M. (1994). *Experimental and numerical modeling of convective proppant transport.* Paper presented at the SPE Annual Technical Conference and Exhibition.

Bivins, C. H., Boney, C., Fredd, C., Lassek, J., Sullivan, P., Engels, J., . . . Mogollon, A. E. S. (2005). New fibers for hydraulic fracturing. *Oilfield Review, 17*(2), 34-43.

Blyton, C. A., Gala, D. P., & Sharma, M. M. (2018). A Study of Proppant Transport With Fluid Flow in a Hydraulic Fracture. *SPE Drilling & Completion, 33*(04), 307-323.

Card, R., Howard, P., & Feraud, J. (1995). A novel technology to control proppant backproduction. *SPE Production & Facilities, 10*(04), 271-276.

Cary, V. E. (2018). *Improving Proppant Transport in Slickwater Fluids Using Newly Developed Viscosifiers.*

Collins, N. A., Grim, R. G., Ghosh, K., & Dorgan, J. R. (2018). *Effect of Degradable Fiber Composition and Shape on Proppant Suspension.* Paper presented at the SPE/AAPG Eastern Regional Meeting.

Dey, S. (1999). Sediment threshold. *Applied Mathematical Modelling, 23*(5), 399-417.

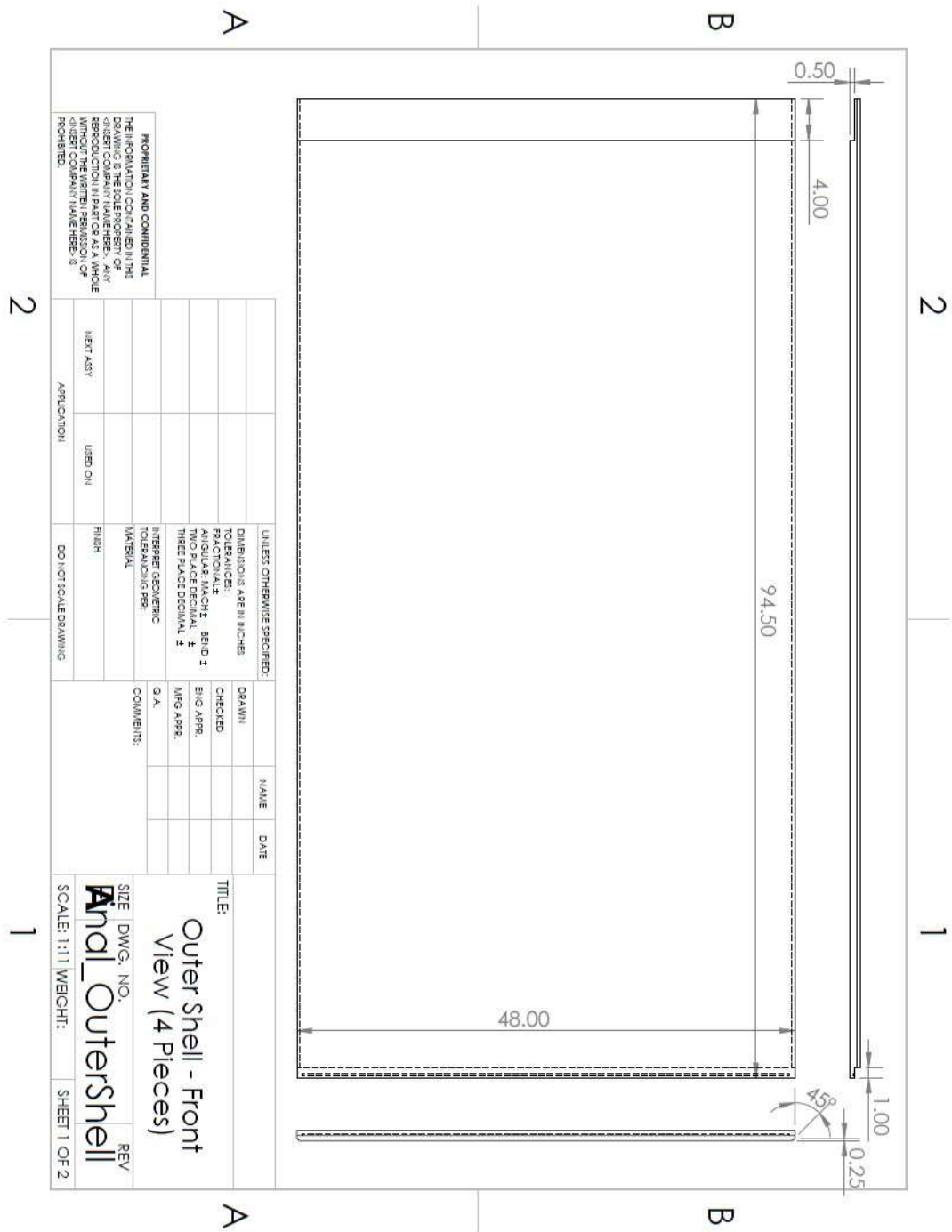Gallagher, D. G. (2011). The hierarchy of oily conductivity. *Journal of Petroleum Technology, 63*(04), 18-19.

Hodge, R., MacKinlay, W., & Landrum, W. (1995). *The selection and application of loss control materials to minimize formation damage in gravel packed completions for a North Sea Field.* Paper presented at the SPE European Formation Damage Conference.

Jack Perrin, T. C. (2016). Hydraulic fractured wells provide two-third of U.S. natural gas production. *Energy Information Administration*. Retrieved from https://www.eia.gov/todayinenergy/detail.php?id=26112

Jaripatke, O. A., Barman, I., Ndungu, J. G., Schein, G. W., Flumerfelt, R. W., Burnett, N., . . . Barzola, G. J. (2018). *Review of Permian completion designs and results.* Paper presented at the SPE Annual Technical Conference and Exhibition.

Johnson, J. L., Turner, M. G., Weinstock, C. T., Pena, A. A., Laggan, M. J., Rondon, J. R., & Lyapunov, K. (2011). *Channel fracturing-a paradigm shift in tight gas stimulation.* Paper presented at the SPE Hydraulic Fracturing Technology Conference.

Kern, L., Perkins, T., & Wyant, R. (1959). The mechanics of sand movement in fracturing. *Journal of Petroleum Technology, 11*(07), 55-57.

Kim, J. Y., Jing, Z., & Morita, N. (2019). *Proppant Transport Studies Using Three Types of Fracture Slot Equipment.* Paper presented at the 53rd US Rock Mechanics/Geomechanics Symposium.

Liang, F., Sayed, M., Al-Muntasheri, G., & Chang, F. F. (2015). *Overview of existing proppant technologies and challenges.* Paper presented at the SPE Middle East Oil & Gas Show and Conference.

Mack, M., Sun, J., & Khadilkar, C. (2014). *Quantifying proppant transport in thin fluids: theory and experiments.* Paper presented at the SPE Hydraulic Fracturing Technology Conference.

Matsui, H., Daitoh, M., Yoshimura, K., & Morita, N. (2012). *Development of environmentally friendly lost circulation materials for riserless drilling.* Paper presented at the International Conference on Health, Safety and Environment in Oil and Gas Exploration and Production.
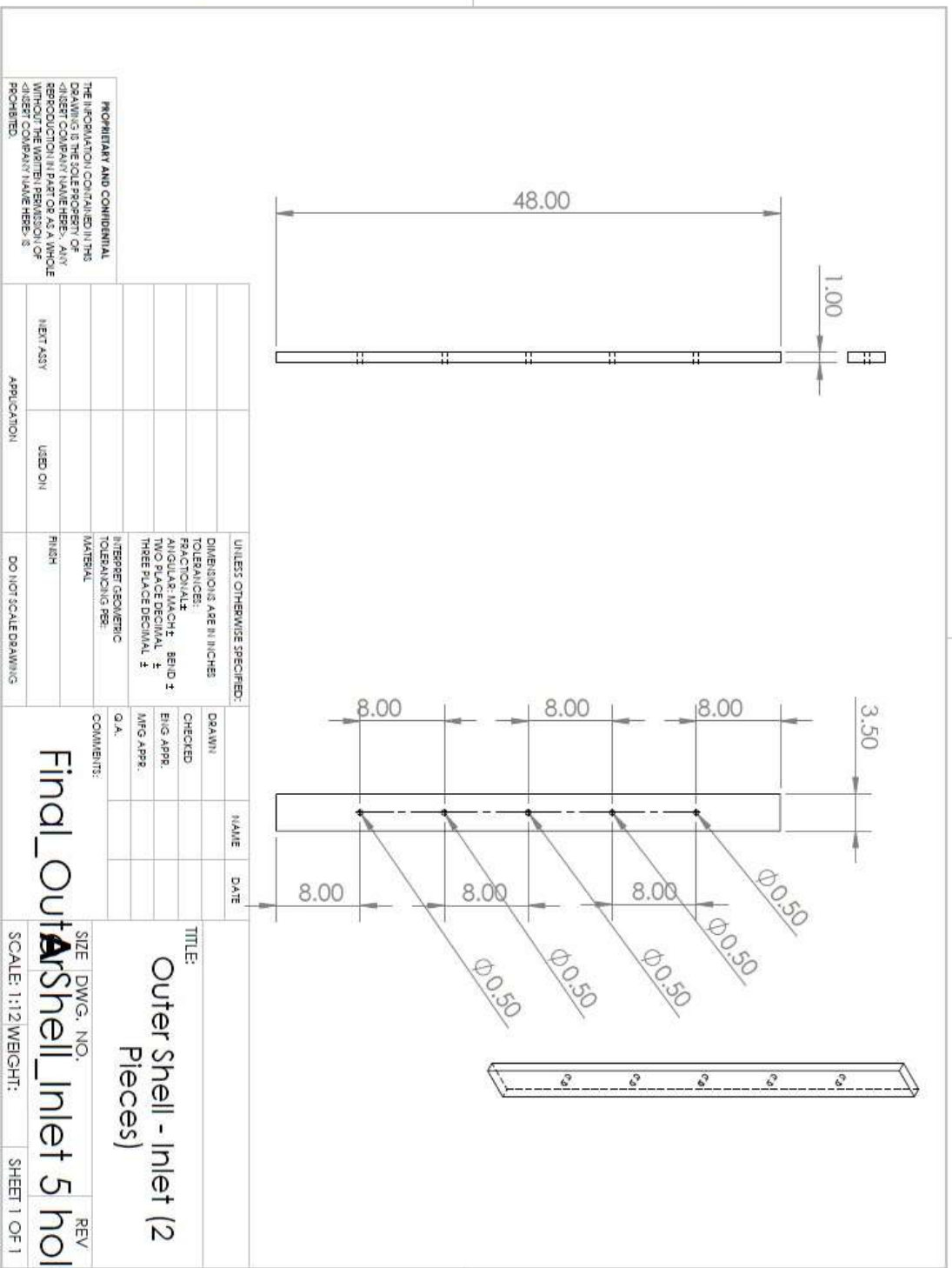
Medvedev, A. V., Kraemer, C. C., Pena, A. A., & Panga, M. K. R. (2013). *On the mechanisms of channel fracturing.* Paper presented at the SPE Hydraulic Fracturing Technology Conference.

Novotny, E. (1977). *Proppant transport.* Paper presented at the SPE Annual Fall Technical Conference and Exhibition.

Okura, M., Takahashi, S., Kobayashi, T., Saijo, H., & Takahashi, T. (2015). *Improvement of impact strength of polyglycolic acid for self-degradable tools for low-temperature wells.* Paper presented at the SPE Middle East Unconventional Resources Conference and Exhibition.

Palisch, T., Duenckel, R., & Wilson, B. (2015). New technology yields ultrahigh-strength proppant. *SPE Production & Operations, 30*(01), 76-81.

Palisch, T. T., Vincent, M., & Handren, P. J. (2010). Slickwater fracturing: food for thought. *SPE Production & Operations, 25*(03), 327-344.

Patel, P., Robart, C., Ruegamer, M., & Yang, A. (2014). *Analysis of US hydraulic fracturing fluid system and proppant trends.* Paper presented at the SPE Hydraulic Fracturing Technology Conference.

Ramones, M., Gutiérrez, L., & Morán, M. (2015). *Unlocking a Mature Field Reservoir Potential through Optimized Fit-for-Purpose Hydraulic Fracturing.* Paper presented at the SPE Latin American and Caribbean Petroleum Engineering Conference.

Safari, R., Lewis, R., Ma, X., Mutlu, U., & Ghassemi, A. (2017). Infill-well fracturing optimization in tightly spaced horizontal wells. *SPE Journal, 22*(02), 582-595.

Schein, G. (2005). The application and technology of slickwater fracturing.

Sitdikov, S. S., Serdyuk, A., Nikitin, A., Yudin, A. V., Mullen, K., Oussoltsev, D., & Butula, K. K. (2009). *Fiber-laden fluid: applied solution for addressing multiple challenges of hydraulic fracturing in western siberia.* Paper presented at the SPE Hydraulic Fracturing Technology Conference.

Southard, J. (2006). *Introduction to Fluid Motions, Sediment Transport and Current-Generated Sedimentary Structures*.

Stokes, G. G. (1851). *On the effect of the internal friction of fluids on the motion of pendulums* (Vol. 9): Pitt Press Cambridge.

Takahashi, S., Okura, M., Kobayashi, T., & Takahashi, T. (2015). *Development and Verification of Degradable Sealing Elements for Fully Degradable Frac Plugs.* Paper presented at the SPE Asia Pacific Unconventional Resources Conference and Exhibition.

Tran, T., Kim, J. Y., Morita, N., & Yoshimura, K. (2017). *Application of PGA Fiber and Fluid-Loss Materials to Slick Water Fracturing.* Paper presented at the 51st US Rock Mechanics/Geomechanics Symposium.

Tran, T. N. (2018). *Effect of Scale in Proppant Transport Experiment Using PGA.*

Valko, P., & Economides, M. (1997). Foam proppant transport. *SPE Production & Facilities, 12*(04), 244-249.

Weijers, L., Wright, C., Mayerhofer, M., Pearson, M., Griffin, L., & Weddle, P. (2019). *Trends in the North American Frac Industry: Invention through the Shale Revolution.* Paper presented at the SPE Hydraulic Fracturing Technology Conference and Exhibition.

Woodworth, T. R. (2006). *Proppant placement in low-viscosity slickwater type fracturing fluids.* Colorado School of Mines. Arthur Lakes Library,

Woodworth, T. R., & Miskimins, J. L. (2007). *Extrapolation of laboratory proppant placement behavior to the field in slickwater fracturing applications.* Paper presented at the SPE Hydraulic Fracturing Technology Conference.

Wu, K., & Olson, J. E. (2014). *Mechanics analysis of interaction between hydraulic and natural fractures in shale reservoirs*.

Yoshimura, K., Matsui, H., & Morita, N. (2016). Development of Polyglycolic-and polylactic-acid fluid-loss-control materials for fracturing fluids. *SPE Drilling & Completion, 30*(04), 295-309.

48.00

1.00

3.50

8.00 8.00 8.00

8.00 8.00 8.00

Ø0.50

Ø0.50

Ø0.50

Ø0.50

Ø0.50

NEXT ASSY

USED ON

APPLICATION

DO NOT SCALE DRAWING

UNLESS OTHERWISE SPECIFIED:

DIMENSIONS ARE IN INCHES
TOLERANCES:
FRACTIONAL±
ANGULAR: MACH± BEND ±
TWO PLACE DECIMAL ±
THREE PLACE DECIMAL ±

INTERPRET GEOMETRIC
TOLERANCING PER:

MATERIAL

FINISH

	NAME	DATE
DRAWN		
CHECKED		
ENG APPR.		
MFG APPR.		
Q.A.		
COMMENTS:		

TITLE:

Final_OuterShell_Inlet 5 hole p
Outer Shell - Inlet (2 Pieces)

SIZE DWG. NO. REV
A

SCALE: 1:12 WEIGHT: SHEET 1 OF 1

Outer Shell Patch
(2 Pieces)

8.00

48.00

0.50

NEXT ASSY

APPLICATION

USED ON

UNLESS OTHERWISE SPECIFIED:

DIMENSIONS ARE IN INCHES
TOLERANCES:
FRACTIONAL±
ANGULAR: MACH± BEND ±
TWO PLACE DECIMAL ±
THREE PLACE DECIMAL ±

INTERPRET GEOMETRIC
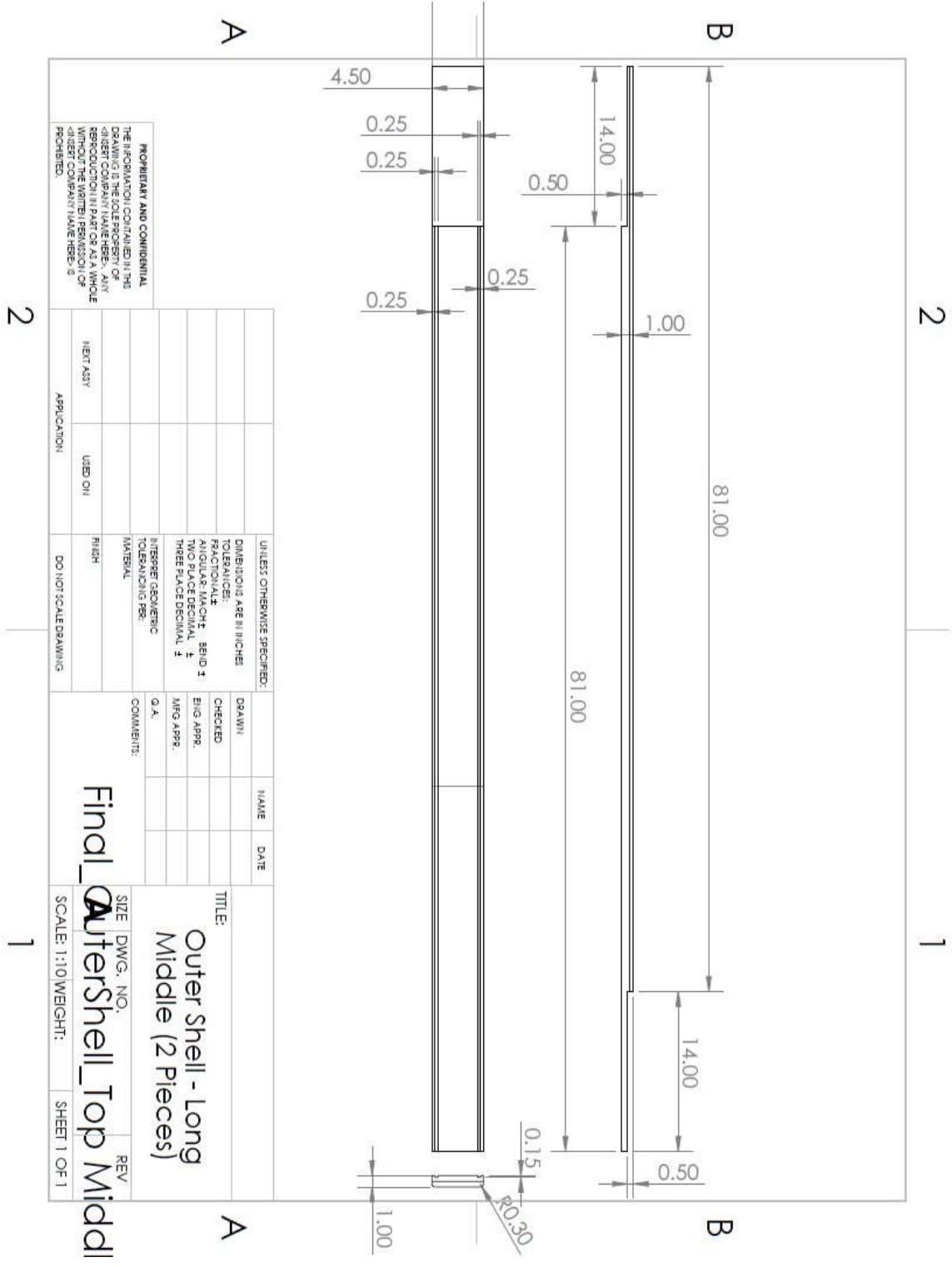TOLERANCING PER:

MATERIAL

FINISH

DO NOT SCALE DRAWING

	NAME	DATE
DRAWN		
CHECKED		
ENG APPR.		
MFG APPR.		
Q.A.		
COMMENTS:		

TITLE:

Outer Shell Patch
(2 Pieces)

Finca OuterShell_Patch

SIZE DWG. NO.   REV
A   OuterShell_Patch

SCALE: 1:10 WEIGHT: SHEET 1 OF 1

102

A

B

2

1

4.50

0.25

0.25

1.00

0.25

0.25

R0.30

95.00

81.00

1.00

14.00

0.50

0.15

R0.30

	NAME	DATE
DRAWN		
CHECKED		
ENG APPR.		
MFG APPR.		
Q.A.		
COMMENTS:		

UNLESS OTHERWISE SPECIFIED:

DIMENSIONS ARE IN INCHES
TOLERANCES:
FRACTIONAL±
ANGULAR: MACH±   BEND ±
TWO PLACE DECIMAL   ±
THREE PLACE DECIMAL   ±

INTERPRET GEOMETRIC
TOLERANCING PER:

MATERIAL

FINISH

DO NOT SCALE DRAWING

NEXT ASSY

USED ON

APPLICATION

TITLE:

Outer Shell Long
Corner (2 Pieces)

SIZE DWG. NO.   REV
A   FinalAOuterShell_Top Left

SCALE: 1:10 WEIGHT: SHEET 1 OF 1

103

Outer Shell - Long Middle (2 Pieces)

4.50
0.25
0.25
0.25
0.25
14.00
0.50
1.00
81.00
81.00
14.00
0.50
0.15
R0.30
1.00

NEXT ASSY | USED ON
APPLICATION

DO NOT SCALE DRAWING

UNLESS OTHERWISE SPECIFIED:

DIMENSIONS ARE IN INCHES
TOLERANCES:
FRACTIONAL±
ANGULAR: MACH± BEND ±
TWO PLACE DECIMAL ±
THREE PLACE DECIMAL ±

INTERPRET GEOMETRIC
TOLERANCING PER:

MATERIAL

FINISH

	NAME	DATE
DRAWN		
CHECKED		
ENG APPR.		
MFG APPR.		
Q.A.		
COMMENTS:		

TITLE:

Outer Shell - Long
Middle (2 Pieces)

SIZE | DWG. NO. | REV
A

SCALE: 1:10 | WEIGHT: | SHEET 1 OF 1

Final_CAD_OuterShell_Top_Middl

2 | 1

A | B

104

Outer Shell - Short Corner (2 Pieces)

Final_OuterShell_Top Right Panel E

UNLESS OTHERWISE SPECIFIED:

DIMENSIONS ARE IN INCHES
TOLERANCES:
FRACTIONAL±
ANGULAR: MACH± BEND ±
TWO PLACE DECIMAL ±
THREE PLACE DECIMAL ±

INTERPRET GEOMETRIC
TOLERANCING PER:

MATERIAL

FINISH

DO NOT SCALE DRAWING

NAME   DATE
DRAWN
CHECKED
ENG APPR.
MFG APPR.
Q.A.
COMMENTS:

TITLE:

SIZE DWG. NO.   REV
A

SCALE: 1:5 WEIGHT: SHEET 1 OF 1

NEXT ASSY   USED ON
APPLICATION

Dimensions: 0.50, 14.00, 27.00, 12.70, R0.30, 0.25, 0.25, 1.00, 0.25, 0.25, 1.00, 0.15, 4.50, 1.00

105

17.00

0.50

29.00

1.00

0.80

0.80

UNLESS OTHERWISE SPECIFIED:

DIMENSIONS ARE IN INCHES
TOLERANCES:
FRACTIONAL±
ANGULAR: MACH± BEND ±
TWO PLACE DECIMAL ±
THREE PLACE DECIMAL ±

INTERPRET GEOMETRIC
TOLERANCING PER:

MATERIAL

FINISH

DO NOT SCALE DRAWING

NAME   DATE

DRAWN
CHECKED
ENG APPR.
MFG APPR.
Q.A.
COMMENTS:

NEXT ASSY   USED ON

APPLICATION

TITLE:

Needs 2 Pieces

SIZE DWG. NO.   REV
A   InnerShell_Bottom Edge Short Bottom

SCALE: 1:5 WEIGHT: SHEET 1 OF 1

106

29.00

0.20

0.50

UNLESS OTHERWISE SPECIFIED:

DIMENSIONS ARE IN INCHES
TOLERANCES:
FRACTIONAL±
ANGULAR: MACH± BEND ±
TWO PLACE DECIMAL ±
THREE PLACE DECIMAL ±

INTERPRET GEOMETRIC
TOLERANCING PER:

MATERIAL

FINISH

DO NOT SCALE DRAWING

NEXT ASSY | USED ON
APPLICATION

DRAWN
CHECKED
ENG APPR.
MFG APPR.
Q.A.
COMMENTS:

NAME | DATE

TITLE:

InnerShell Bottom Edge Short

SIZE | DWG. NO. | REV
A

SCALE: 1:4 | WEIGHT: | SHEET 1 OF 1

107

0.50

17.00

95.00

1.00

17.00

0.50

0.80

B

UNLESS OTHERWISE SPECIFIED:

DIMENSIONS ARE IN INCHES
TOLERANCES:
FRACTIONAL±
ANGULAR: MACH±   BEND ±
TWO PLACE DECIMAL   ±
THREE PLACE DECIMAL ±

INTERPRET GEOMETRIC
TOLERANCING PER:

MATERIAL

FINISH

DO NOT SCALE DRAWING

	NAME	DATE
DRAWN		
CHECKED		
ENG APPR.		
MFG APPR.		
Q.A.		
COMMENTS:		

NEXT ASSY   USED ON

APPLICATION

TITLE:

Needs 2 Pieces

SIZE DWG. NO.   REV
A   InnerShell_Bottom Middle Long Bottom

SCALE: 1:16 WEIGHT: SHEET 1 OF 1

108

78.00

0.20

0.50

		UNLESS OTHERWISE SPECIFIED:			NAME	DATE
		DIMENSIONS ARE IN INCHES	DRAWN			
		TOLERANCES:	CHECKED			
		FRACTIONAL±	ENG APPR.			
		ANGULAR: MACH± BEND ±	MFG APPR.			
		TWO PLACE DECIMAL ±				
		THREE PLACE DECIMAL ±	Q.A.			

INTERPRET GEOMETRIC
TOLERANCING PER:

MATERIAL

FINISH

COMMENTS:

NEXT ASSY   USED ON

APPLICATION   DO NOT SCALE DRAWING

TITLE:

Needs 2 Pieces

SIZE DWG. NO.   REV
A   InnerShell_Bottom Middle Long Top

SCALE: 1:13 WEIGHT: SHEET 1 OF 1

109

92.50

44.00

0.25

NEXT ASSY   USED ON

APPLICATION

DO NOT SCALE DRAWING

UNLESS OTHERWISE SPECIFIED:

DIMENSIONS ARE IN INCHES
TOLERANCES:
FRACTIONAL±
ANGULAR: MACH±   BEND ±
TWO PLACE DECIMAL   ±
THREE PLACE DECIMAL ±

INTERPRET GEOMETRIC
TOLERANCING PER:

MATERIAL
Plycarbonate

FINISH

COMMENTS:

DRAWN
CHECKED
ENG APPR.
MFG APPR.
Q.A.

NAME   DATE

TITLE:

Polycarbonate
Needs 4 Pieces

SIZE DWG. NO.   REV
A   Polycarbonate

SCALE: 1:20 WEIGHT: SHEET 1 OF 1

Inner Shell (4 Pieces)

Dimensions noted on drawing:

- 0.75
- 0.05
- 93.50
- 46.00
- 1.00
- 0.20
- 1.00
- 1.00
- 0.05
- 0.05
- 0.75
- 1.00

	NAME	DATE
DRAWN		
CHECKED		
ENG APPR.		
MFG APPR.		
Q.A.		
COMMENTS:		

UNLESS OTHERWISE SPECIFIED:

DIMENSIONS ARE IN INCHES
TOLERANCES:
FRACTIONAL±
ANGULAR: MACH± BEND ±
TWO PLACE DECIMAL ±
THREE PLACE DECIMAL ±

INTERPRET GEOMETRIC TOLERANCING PER:

MATERIAL

FINISH

DO NOT SCALE DRAWING

NEXT ASSY | USED ON
APPLICATION

TITLE:

SIZE A | DWG. NO. Final_InnerShell | REV

SCALE: 1:11 | WEIGHT: | SHEET 1 OF 1

2 | 1

A | B

Needs 2 Pieces

95.00

0.80

17.00

0.50

1.00

UNLESS OTHERWISE SPECIFIED:

DIMENSIONS ARE IN INCHES
TOLERANCES:
FRACTIONAL±
ANGULAR: MACH± BEND ±
TWO PLACE DECIMAL ±
THREE PLACE DECIMAL ±

INTERPRET GEOMETRIC
TOLERANCING PER:

MATERIAL

FINISH

	NAME	DATE
DRAWN		
CHECKED		
ENG APPR.		
MFG APPR.		
Q.A.		
COMMENTS:		

DO NOT SCALE DRAWING

NEXT ASSY | USED ON
APPLICATION

TITLE:

Needs 2 Pieces

SIZE DWG. NO.   REV
A   Final_InnerShell_Bottom Left Bottom

SCALE: 1:14 WEIGHT: SHEET 1 OF 1

112

TITLE: Needs 2 Pieces

78.00

0.50   0.20

-

UNLESS OTHERWISE SPECIFIED:

DIMENSIONS ARE IN INCHES
TOLERANCES:
FRACTIONAL±
ANGULAR: MACH± BEND ±
TWO PLACE DECIMAL ±
THREE PLACE DECIMAL ±

INTERPRET GEOMETRIC TOLERANCING PER:

MATERIAL

FINISH

DO NOT SCALE DRAWING

	NAME	DATE
DRAWN		
CHECKED		
ENG APPR.		
MFG APPR.		
Q.A.		
COMMENTS:		

NEXT ASSY | USED ON

APPLICATION

SIZE | DWG. NO. | REV
A | Final_InnerShell_Bottom Left Top

SCALE: 1:11 | WEIGHT: | SHEET 1 OF 1

113

1.00

8.00

8.00

7.00

7.00

8.00

8.00

1.10

φ0.50

φ0.50

φ0.50

φ0.50

φ0.50

46.00

UNLESS OTHERWISE SPECIFIED:				NAME	DATE
DIMENSIONS ARE IN INCHES		DRAWN			
TOLERANCES:		CHECKED			
FRACTIONAL±		ENG APPR.			
ANGULAR: MACH± BEND ±		MFG APPR.			
TWO PLACE DECIMAL ±					
THREE PLACE DECIMAL ±		Q.A.			
		COMMENTS:			
INTERPRET GEOMETRIC					
TOLERANCING PER:					
MATERIAL					
FINISH					
DO NOT SCALE DRAWING					

NEXT ASSY

USED ON

APPLICATION

TITLE:

Needs 2 Pieces

SIZE   DWG. NO.   REV
A   Final_InnerShell_Intlet 5 holes Bottom

SCALE: 1:10 WEIGHT: SHEET 1 OF 1

A

B

2

1

B

A

UNLESS OTHERWISE SPECIFIED:

DIMENSIONS ARE IN INCHES
TOLERANCES:
FRACTIONAL±
ANGULAR: MACH±   BEND ±
TWO PLACE DECIMAL   ±
THREE PLACE DECIMAL ±

INTERPRET GEOMETRIC
TOLERANCING PER:

MATERIAL

FINISH

DO NOT SCALE DRAWING

	NAME	DATE
DRAWN		
CHECKED		
ENG APPR.		
MFG APPR.		
Q.A.		
COMMENTS:		

NEXT ASSY | USED ON
APPLICATION

1.00

5.00

0.20

TITLE:

Needs 4 Pieces

SIZE DWG. NO.   REV
A   Final_InnerShell_Intlet 5 holes Bottom 1

SCALE: 1:2 WEIGHT: SHEET 1 OF 1

Needs 4 Pieces

115

192.50

0.25

50.50

2.25

2.25

2.25

NEXT ASSY

APPLICATION

USED ON

UNLESS OTHERWISE SPECIFIED:

DIMENSIONS ARE IN INCHES
TOLERANCES:
FRACTIONAL±
ANGULAR: MACH± BEND ±
TWO PLACE DECIMAL ±
THREE PLACE DECIMAL ±

INTERPRET GEOMETRIC
TOLERANCING PER:

MATERIAL

FINISH

DO NOT SCALE DRAWING

NAME   DATE

DRAWN

CHECKED

ENG APPR.

MFG APPR.

Q.A.

COMMENTS:

TITLE:

Steel Frame

SIZE DWG. NO.   REV
A

SCALE: 1:22 WEIGHT: SHEET 1 OF 1

52.50

1.00

0.25

0.75

Ø0.63

2.00

R0.38

0.25

54.50

3.00

	NAME	DATE
DRAWN		
CHECKED		
ENG APPR.		
MFG APPR.		
Q.A.		
COMMENTS:		

TITLE:

SIZE **A** DWG. NO. **Steel Bar** REV
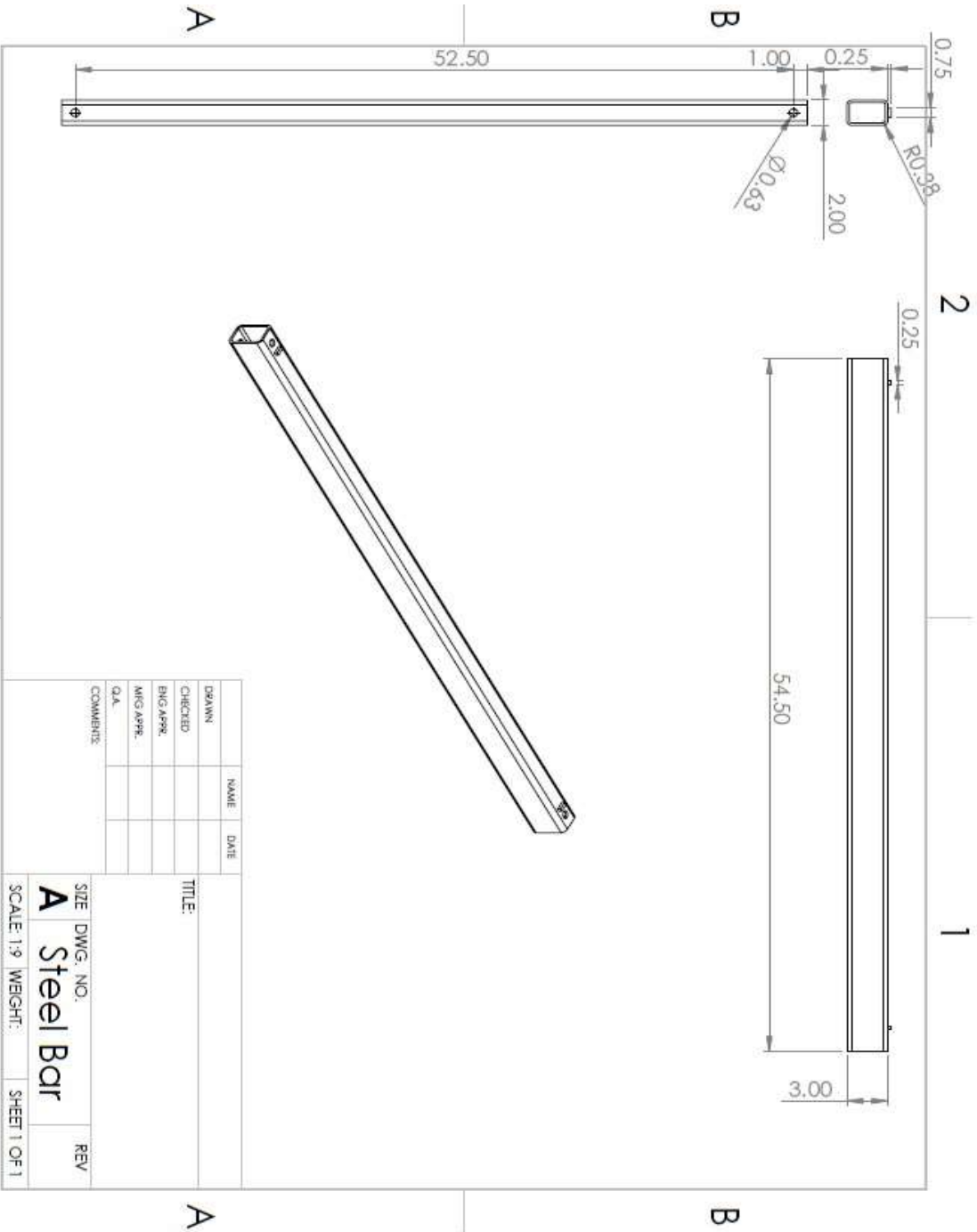
SCALE: 1:9 WEIGHT: SHEET 1 OF 1

A

B

2

1

A

B

APPENDIX B   ADDITIONAL SIMULATION STUDY

In this appendix B-1, first model to simulate and compare is a single horizontal well (unconventional reservoir) with three vertical fractures with the following details below. We use a lower pumping rate to show what happens if the injection rate of frac fluid is low when compare to the case 3. In this case, pre-pad pump rate and amount pumped increased from 30 bpm to 60 bpm, and 20,000 gal to 60,000 gal. The slurry pump rate and the amount pumped increased from 30 bpm to 60 bpm, and 60,000 gal to 180,000 gal. Below is the detail of the simulation, which has the same geology and reservoir data. The difference is the number of fractures; case 3 has one whereas this case has three fractures.

Appendix B-1: three vertical fracture propagations from a horizontal well (unconventional reservoir)

- **Reservoir:**
  Pay depth: 2150-2450ft, Initial reservoir pressure: 1500psi, Current reservoir pressure: 1000psi, Bottomhole Flowing Pressure: 500psi, Sand formation, Porosity: 0.15, permeability: 5 md, rock compressibility: 1.7×10^{-6} 1/psi, oil reservoir with 40 API gravity, Bottomhole reservoir temperature: 200°F.
- **Well data:**
  Treatment through tubing, horizontal well, Borehole diameter=8.5";
  Casing: 7" OD, 6.366" ID, 0~2500 ft TVD, Horizontal lateral length: 1100 ft kick-off at 2400 ft TVD
  Tubing: 4.5 OD, 4.052" ID, 0~2400ft TVD;
  Fracture initiation: 2500 – 2505 ft with 6 shots/ft; 2550 – 2555 ft with 6 shots/ft; 2600 – 2605 with 6 shots/ft
- **Geologic Layer Data:**
  Layer I: 1710 psi at 1900 ft TVD and 1890 psi at 2100 ft TVD with 0.9 psi/ft overburden;
  Layer II: 1470 psi at 2100 ft TVD and 1820 psi at 2600 ft TVD with 0.7 psi/ft overburden;
  Layer III: 2340 psi at 2600 ft TVD with 0.9 psi/ft overburden;
  Young's modulus: 3×10^6 psi, Poisson's ratio: 0.2, fracture toughness: 2000 $psi\sqrt{in}$.

- **Slurry Data:**

  Fluid Data: Fluid loss coefficient= 0.0005 ft/$\sqrt{min}$, 0.1 wt. % guar, K'= 0.000134, n'= 0.9.

  Proppant data: 30/50 mesh ceramic proppant, density=2.6g/cm^3 (1.57 g/cm^3 as bulk density). Proppant pack porosity: 0.35 without fiber and 0.4 with fiber; Pump schedule: pad= 60,000 gal with 60 BPM (pump time 23.8min), slurry injection 180,000 gal with 60 BPM (4 PPG proppant concentration, pump time 71.4min.)

The simulation results are illustrated below in **Figs. 85** to **93**. The total of 4 different fiber concentrations (0.4, 0.3, 0.2, and 0.1 wt. %) are compared to the fluids composition and slurry data shown above without the presence of fibers. Each of the three fractures are compared separately related to the fiber concentration. **Fig. 84** is shown as the bottom hole pressure for the base case.
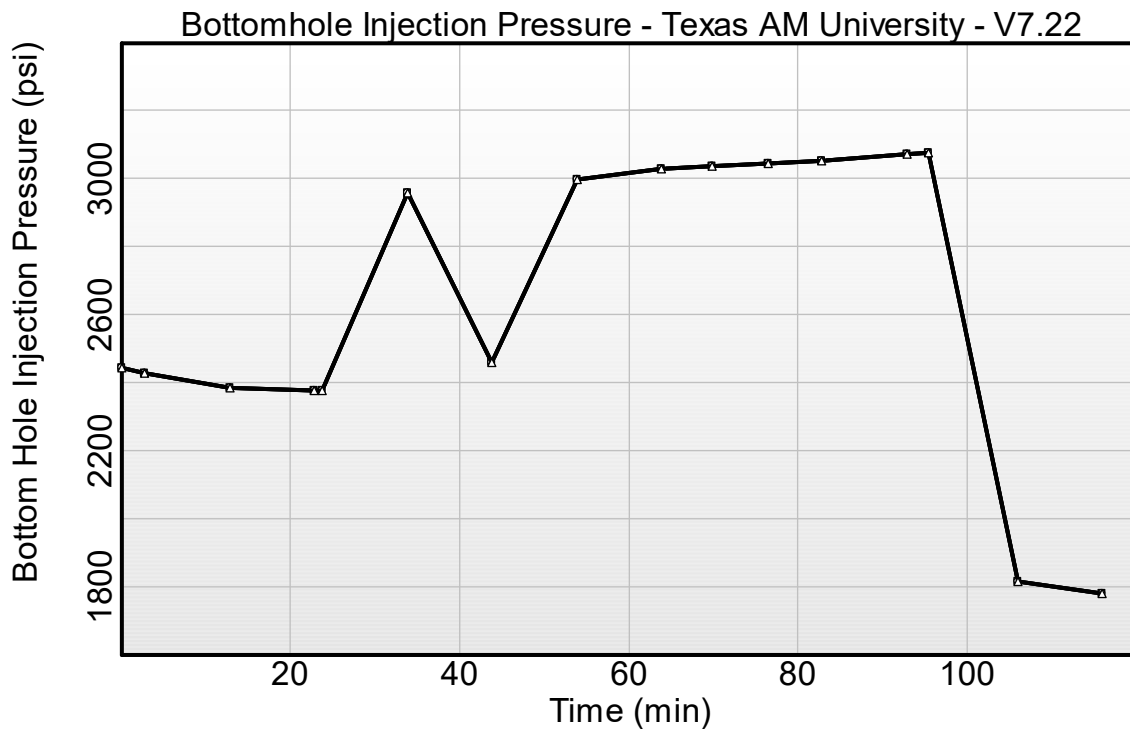

Figure 84. Bottomhole injection pressure for the appendix B-1 (Base case without fiber).

Figs. 85 shows the fracture geometry comparison of the fracture perforated between 2500 to 2505 ft MD, fracture closest to the heel of the well. As the fiber is included in the fluid, we can see that the fracture geometry changes drastically. The fracture length decreased by 39% when 0.1 wt. % of fiber is introduced compared to the base case. The average width of the fracture with 0.1 wt. % fiber increased to 0.3, which is about 88% increase when compare to the base case, the trend continues as more fibers are introduced. The average width increases while the fracture half-length decreases when the fiber concentration increases. The early proppant settlement contributes to the change in the fracture geometry. As the proppant settles early in the base case, it creates resistance for the fluids to flow, leading longer fracture half-length as the fluid has less resistance traveling horizontally.
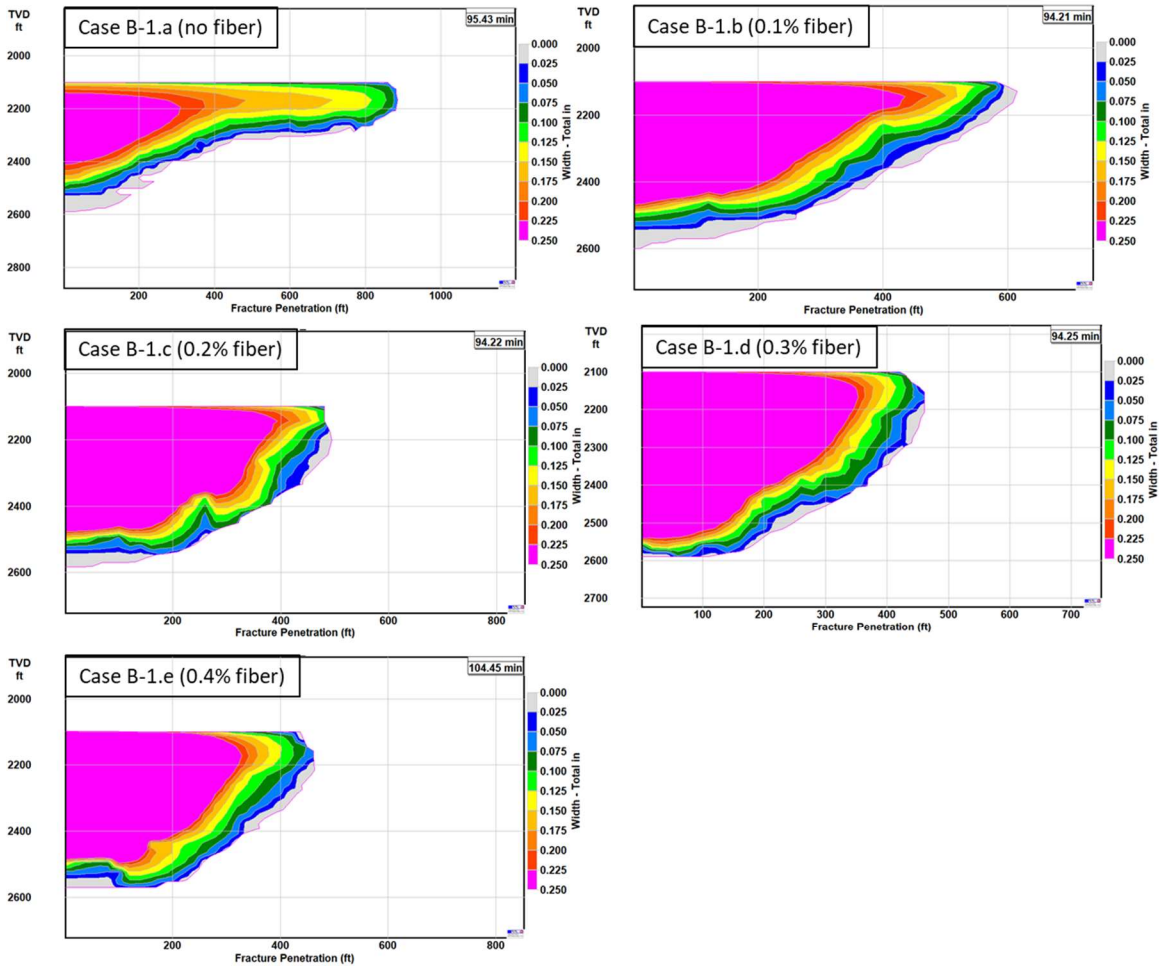
Figure 85. Fracture widths at the end of pumping for the fracture perforated between 2500 to 2505 MD (Appendix B-1 (a to e), with 3 cp viscosity at the reservoir condition).

The next three figures (**Figs. 86** to **88**) compare the proppant transport with increase in the fiber concentration. It should be noted that the average proppant concentration and the average conductivity increased by approximately 43% as the fiber is introduced. The increase continues, although small, as more fibers are added. The better proppant suspension for the fluids with fiber lead to enhanced proppant transport, increasing proppant coverage and the conductivity.

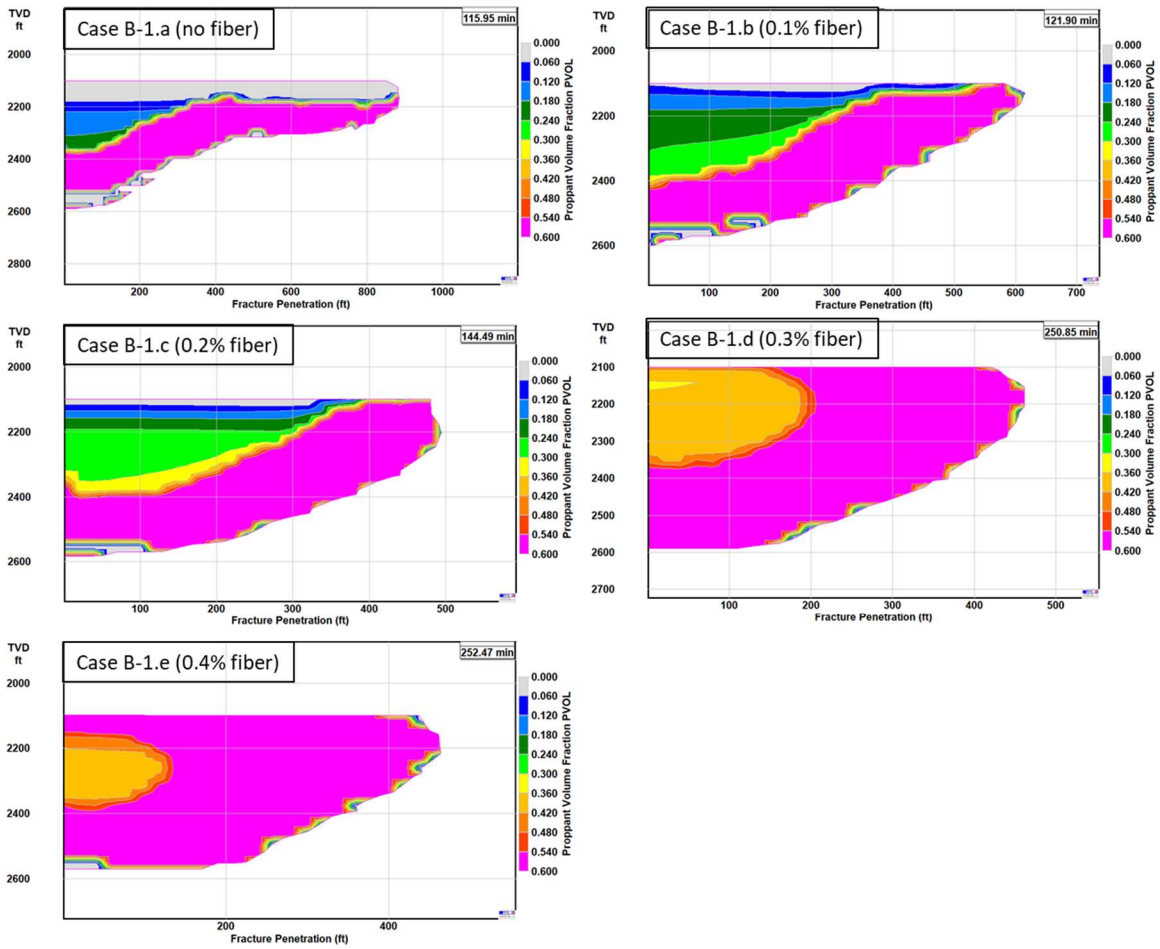Appendix B-1. perf between 2500 ~ 2505 MD with 6 shots/ft

Figure 86. Proppant volume fraction after fracture closure (Appendix B-1 (a to e), with 3 cp viscosity at the reservoir condition).

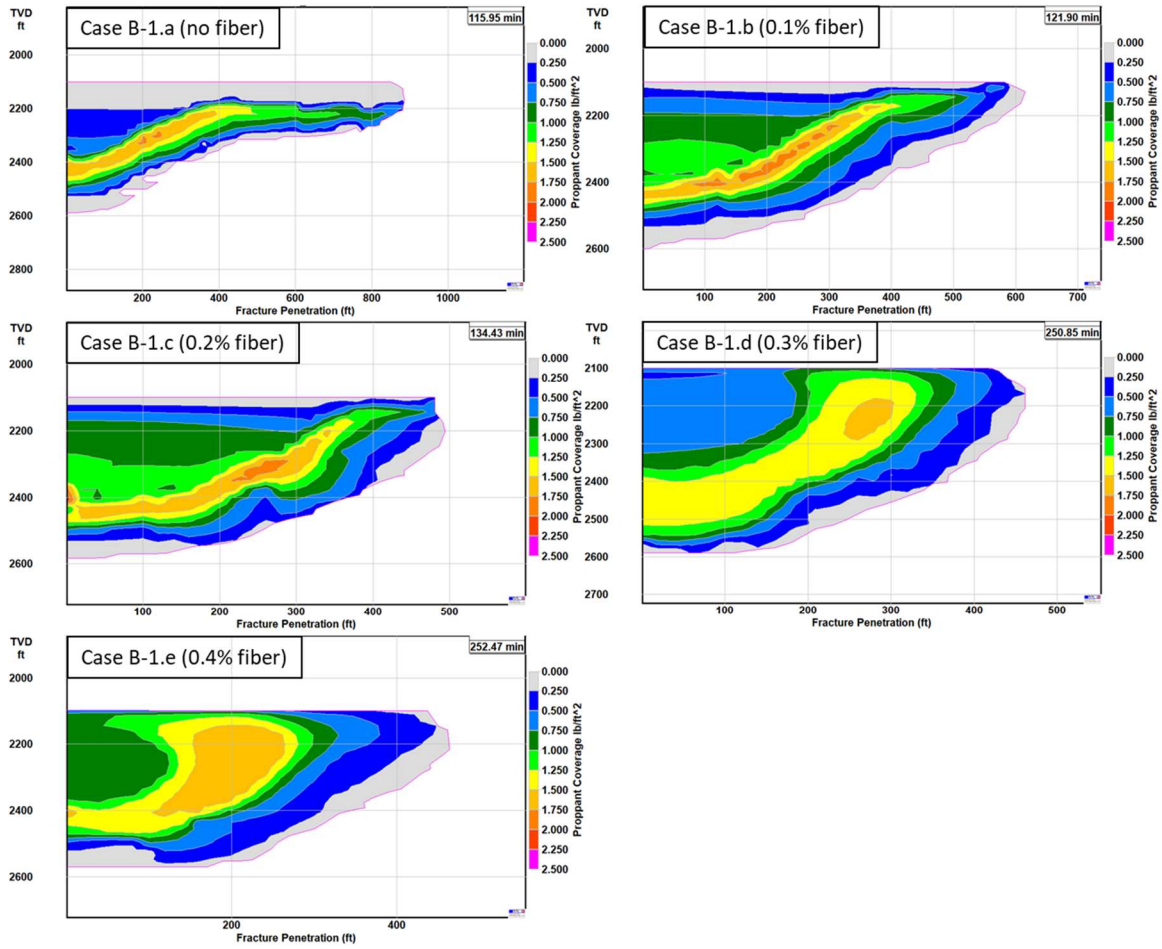**Figure 87. Proppant coverage after fracture closure (Appendix B-1 (a to e), with 3 cp viscosity at the reservoir condition).**
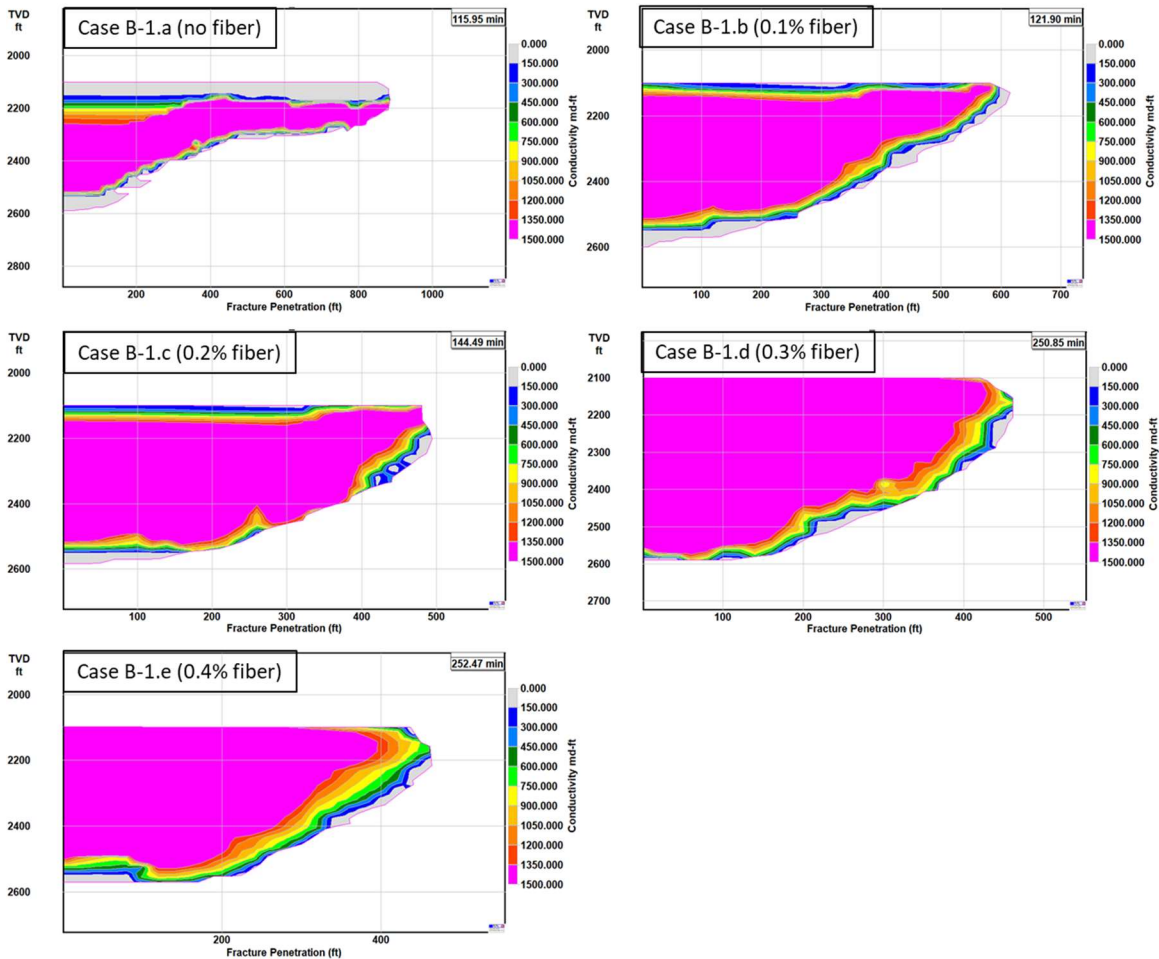
Figure 88. Proppant fracture conductivity after fracture closure (Appendix B-1 (a to e), with 3 cp viscosity at the reservoir condition).

As it can be seen from **Fig. 89**, due to the stress interference of the multiple, parallel fractures, the second fracture that is placed at the middle of the three fractures only propagated 300 feet at the most without any significant width for further comparison of the proppant transport mechanism. Thus, the comparison is not done on the second fracture that sits between the other two fractures.
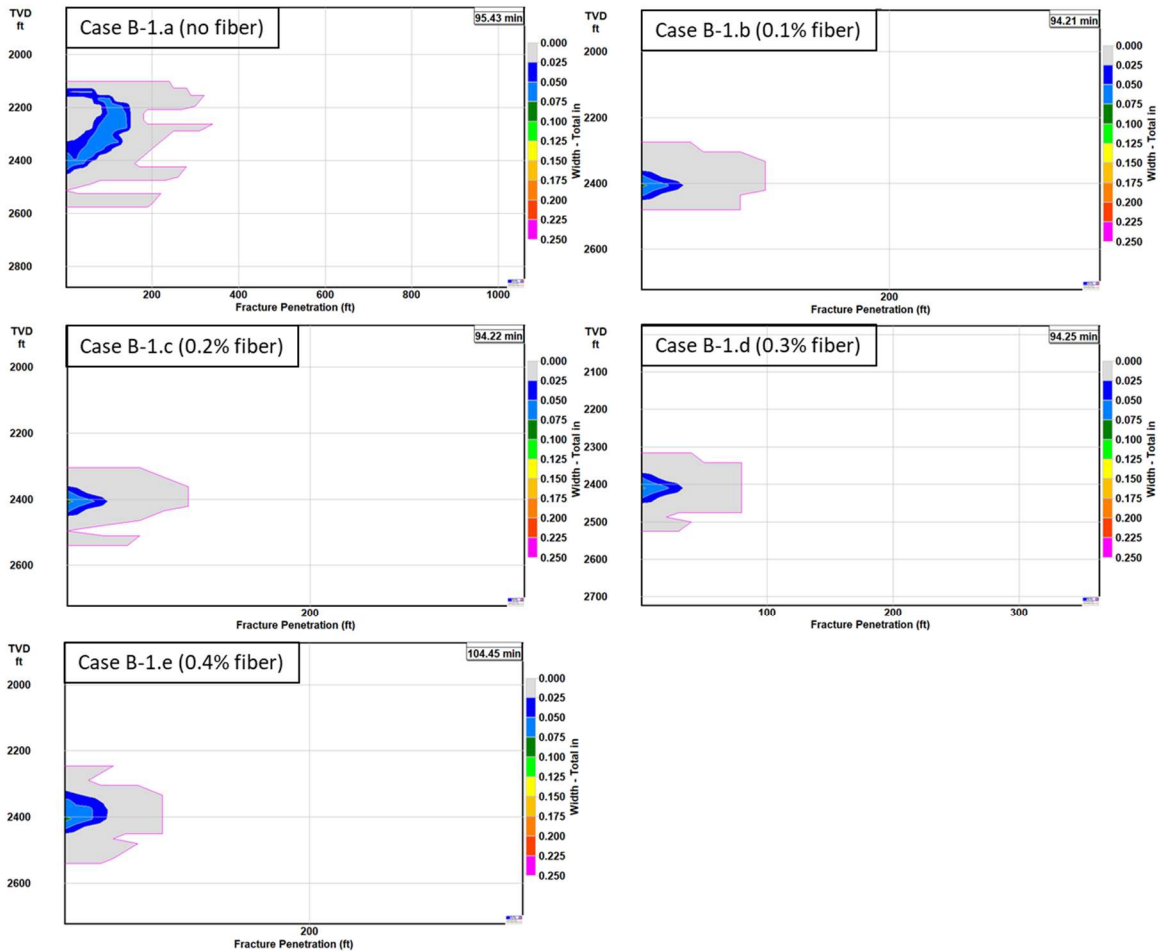
Figure 89. Fracture widths at the end of pumping for the fracture perforated between 2550 to 2555 MD (Appendix B-1 (a to e), with 3 cp viscosity at the reservoir condition).

The final comparison is done on the perforation between 2600 and 2605 ft. MD, which is located near the toe of the fracture. As it can be seen from **Fig. 90**, the fracture half-length decreases and the width increases as the fibers are added to the fracturing fluids. The fracture half-length for the base case is approximately 940 ft., which is longer than the base case of the fracture that is located near the heel side of the horizontal well. The decrease in the fracture half-length when fiber is added are approximately 30, 45, 50, and 51 % from the base case for 0.1, 0.2, 0.3, and 0.4 wt. % fiber, still giving longer

fracture half-length on all fiber concentrations compare the fracture located near the hill. The fracture width is also showing similar behavior when compared to the fracture located near the hill. The average width increased by more than 46% to 166% as the fiber is added compared to the average width of 0.15 inches for the base case.
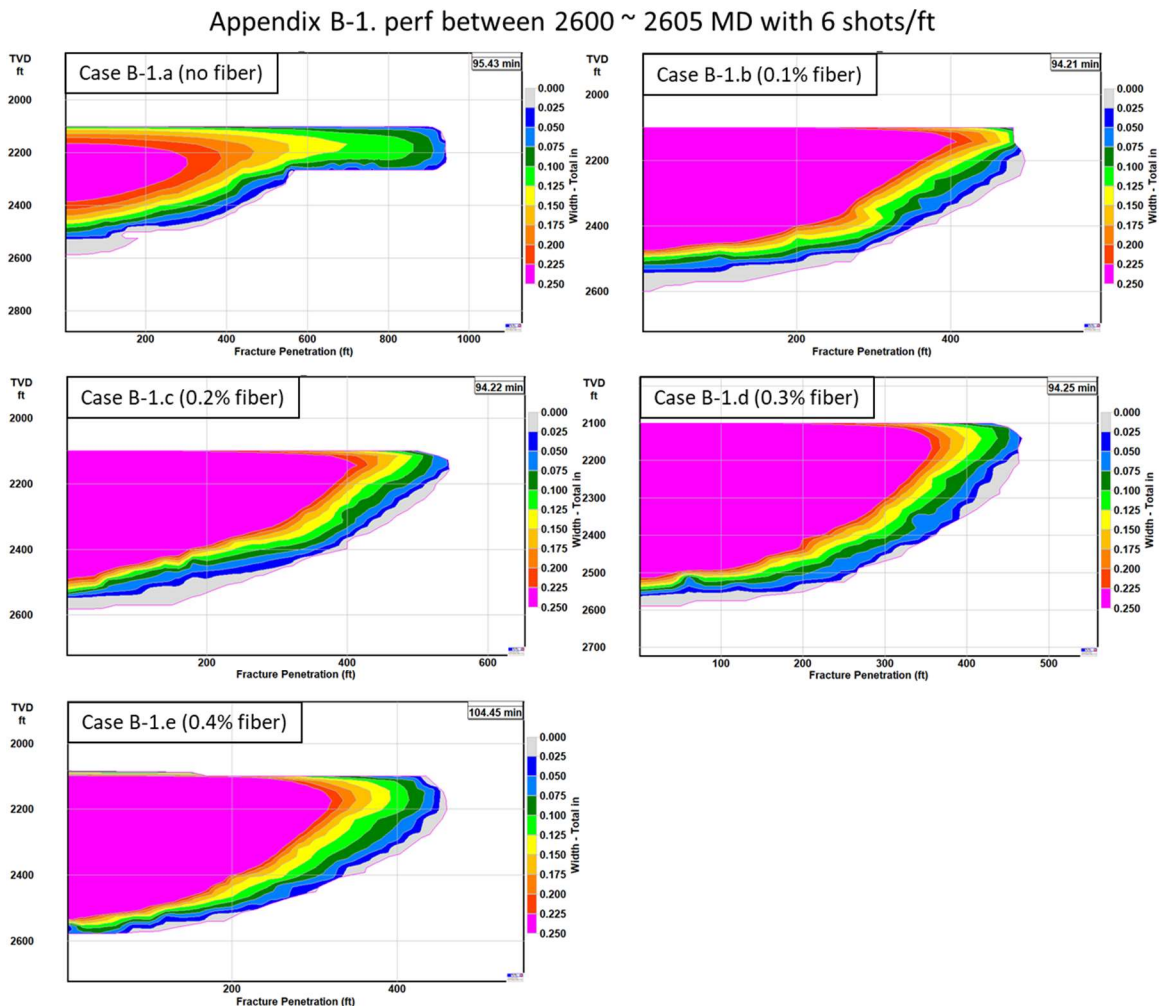

Figure 90. Fracture widths at the end of pumping for the fracture perforated between 2600 to 2605 MD (Appendix B-1 (a to e), with 3 cp viscosity at the reservoir condition).

The next three figures (**Figs. 91** to **93**) compare the proppant transport with increase in the fiber concentration for the fracture located near the toe of the fracture. As more fiber is added, the average proppant concentration and conductivity increased significantly. The

increase is quite different compare to the fracture near the toe. The concentration and conductivity increased by approximately 16% to 63% as the more fibers are added. When 0.1 wt. % of fiber is added, the concentration and conductivity only increased by approximately 16%. This is small increase compare to the fracture located near the hill of the wellbore; the increase is approximately 43%. As more fiber is added, the increase of the proppant concentration and conductivity becomes more significant; increase is approximately 43% for 0.4 wt. % fiber compare to the base case; and the average proppant concentration and conductivity is approximately 0.9 $\frac{lbs}{ft^2}$ and 2700 md-ft for the fracture at the toe and hill with 0.4 wt. % fiber.
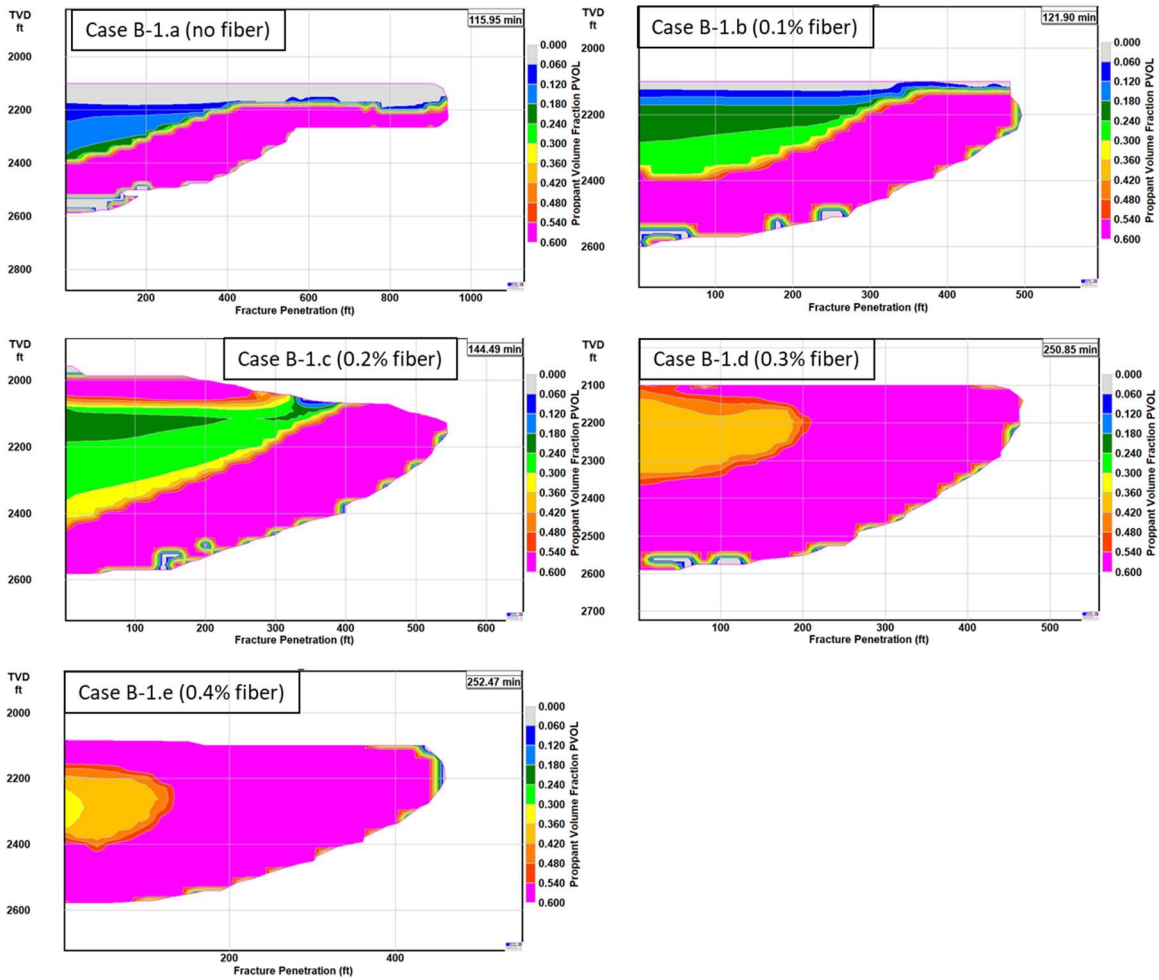
Figure 91. Proppant volume fraction after fracture closure for the fracture perforated between 2600 to 2605 MD (Appendix B-1 (a to e), with 3 cp viscosity at the reservoir condition).
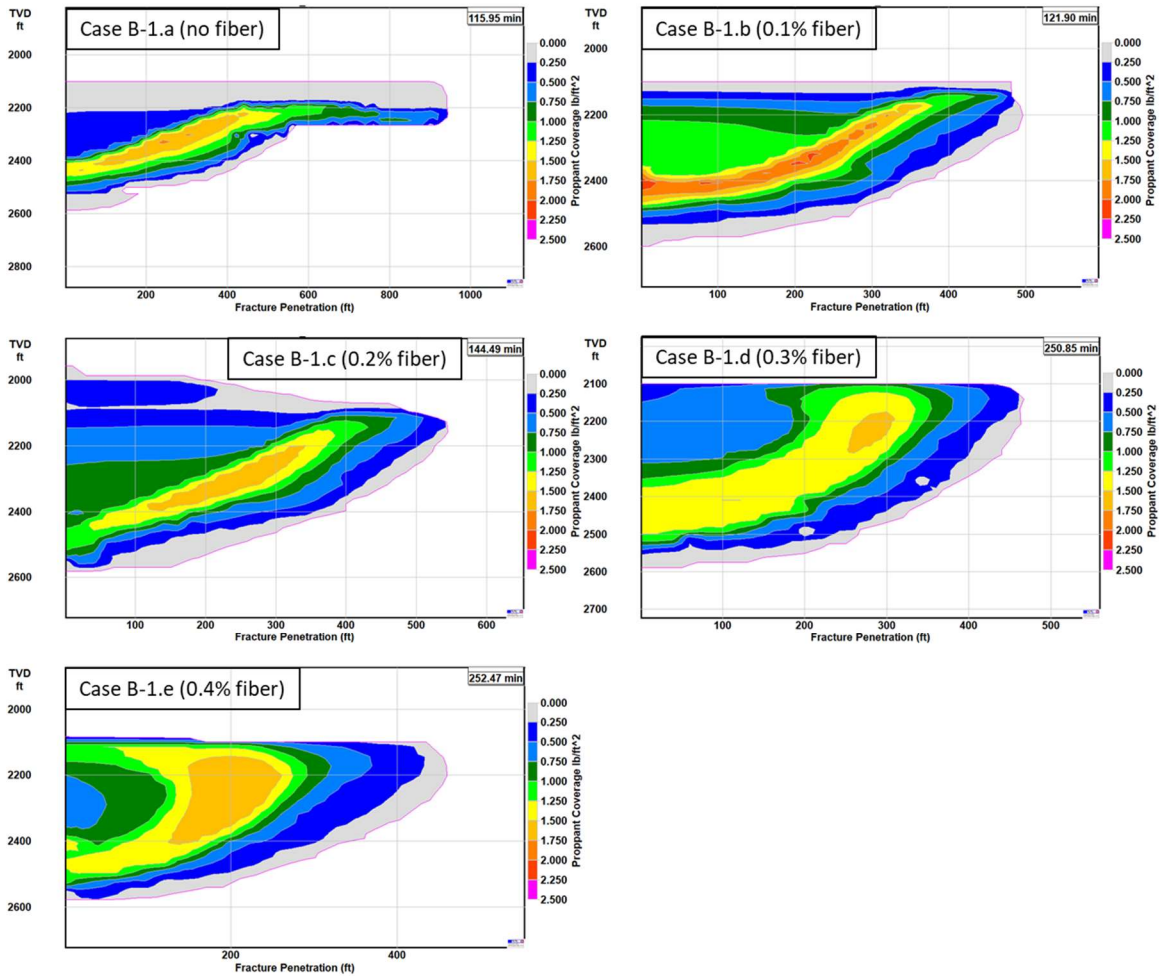
Figure 92. Proppant coverage after fracture closure for the fracture perforated between 2600 to 2605 MD (Appendix B-1 (a to e), with 3 cp viscosity at the reservoir condition).
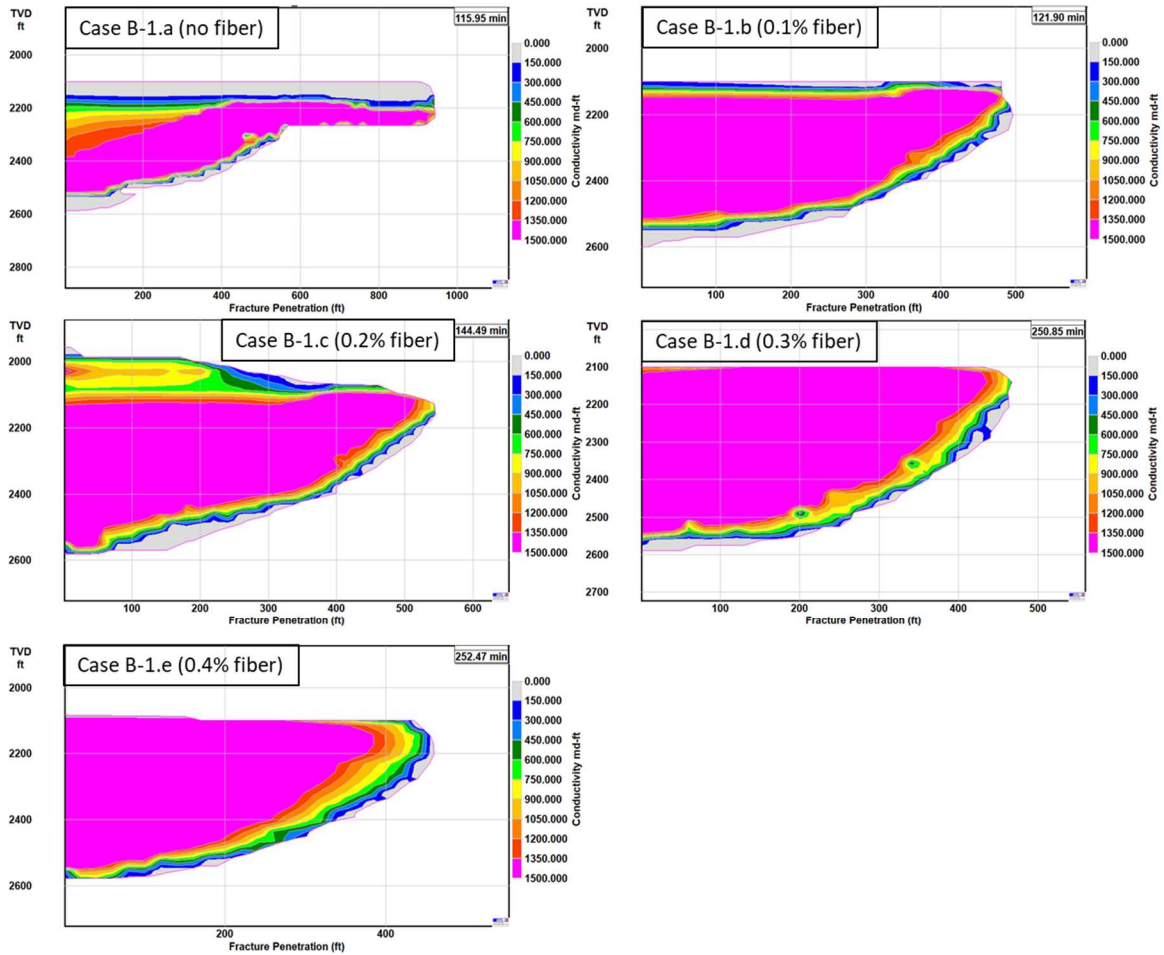
Figure 93. Proppant fracture conductivity after fracture closure for the fracture perforated between 2600 to 2605 MD (Appendix B-1 (a to e), with 3 cp viscosity at the reservoir condition).

The appendix B-2 simulate a single horizontal well (unconventional reservoir) with three vertical fractures with the following details below. The conditions are the same as Case 2 except for three fractures are induced from one cluster instead of one fracture. The proppant size differs as well, 40/70 mesh proppant is used instead of 30/50 mesh. The injection volume and injection rate are set to three times larger than Case 2 since three fractures simultaneously propagate for this case compare to Case 2.

Appendix B-2: three vertical fracture propagations from a horizontal well (unconventional reservoir)

- **Reservoir:**
  Pay depth: 2150-2450ft, Initial reservoir pressure: 1500psi, Current reservoir pressure: 1000psi, Bottomhole Flowing Pressure: 500psi, Sand formation, Porosity: 0.15, permeability: 5 md, rock compressibility: 1.7×10^{-6} 1/psi, oil reservoir with 40 API gravity, Bottomhole reservoir temperature: 200°F.

- **Well data:**
  Treatment through tubing, horizontal well, Borehole diameter=8.5";
  Casing: 7" OD, 6.366" ID, 0~2500 ft TVD, Horizontal lateral length: 1100 ft kick-off at 2400 ft TVD
  Tubing: 4.5 OD, 4.052" ID, 0~2400ft TVD;
  Fracture initiation: 2500 – 2505 ft with 6 shots/ft; 2550 – 2555 ft with 6 shots/ft; 2600 – 2605 with 6 shots/ft

- **Geologic Layer Data:**
  Layer I: 1710 psi at 1900 ft TVD and 1890 psi at 2100 ft TVD with 0.9 psi/ft overburden;
  Layer II: 1470 psi at 2100 ft TVD and 1820 psi at 2600 ft TVD with 0.7 psi/ft overburden;
  Layer III: 2340 psi at 2600 ft TVD with 0.9 psi/ft overburden;
  Young's modulus: 3×10^6 psi, Poisson's ratio: 0.2, fracture toughness: 2000 $psi\sqrt{in}$.

- **Slurry Data:**
  Fluid Data: Fluid loss coefficient= 0.0005 ft/$\sqrt{min}$, 0.1 wt. % guar, K'= 0.000134, n'= 0.9.
  Proppant data: 40/70 mesh ceramic proppant, density=2.6g/cm^3 (1.57 g/cm^3 as bulk density). Proppant pack porosity: 0.35 without fiber and 0.4 with fiber;
  Pump schedule: pad= 60,000 gal with 90 BPM (pump time 15.9 min), slurry injection 180,000 gal with 90 BPM (4 PPG proppant concentration, pump time 47.6

min.)

The appendix B-2 simulation results are illustrated below in **Figs. 95** to **106**. The total of 4 different fiber concentrations (0.4, 0.3, 0.2, and 0.1 wt. %) are compared to the fluids composition and slurry data shown above for the case 4 without the presence of fibers. Each of the three fractures are compared separately related to the fiber concentration. **Fig. 94** is shown as the bottom hole pressure for the base case.
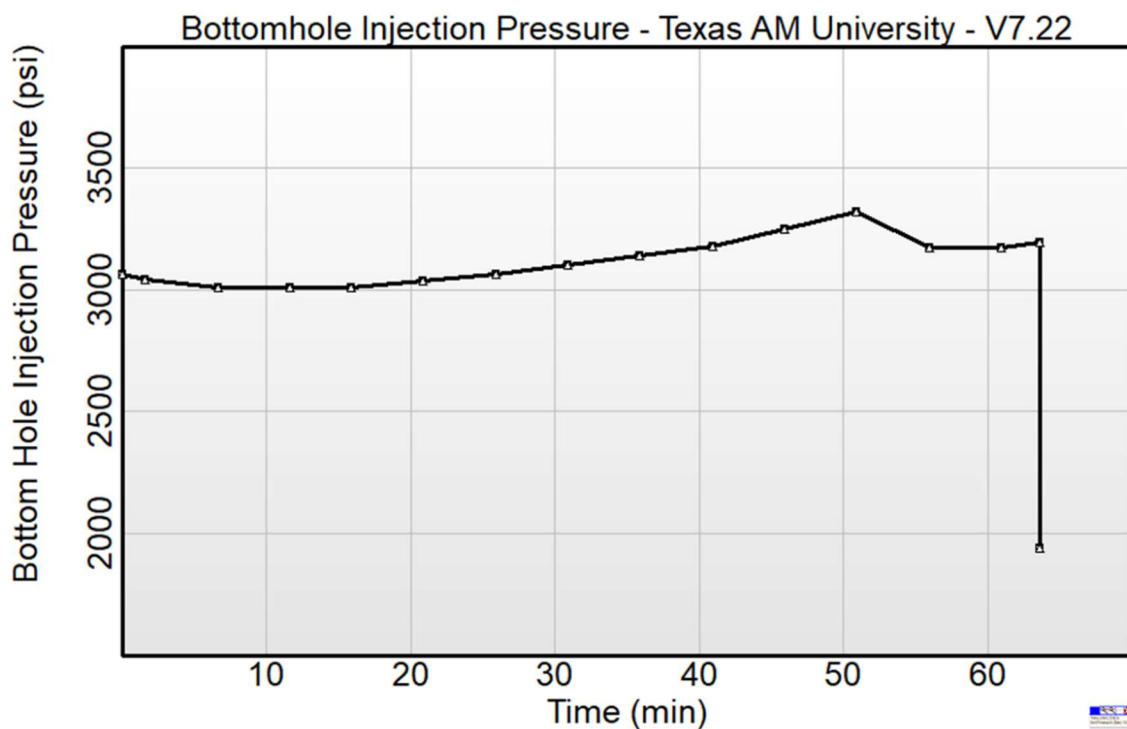

Figure 94. Bottomhole injection pressure for the appendix B-2 (Base case without fiber).

Fig. 95 shows the fracture geometry comparison of the fracture perforated between 2500 to 2505 ft MD, fracture closest to the heel of the well. As the fiber is included in the fluid, we can see that the average widths increased to up to 52% from the base case at 0.19 inch. However, the change in the fracture length was not significant; ranged between 484 to 498

ft. The change in the maximum fracture height was not significant neither; ranged between 496 to 500 ft.
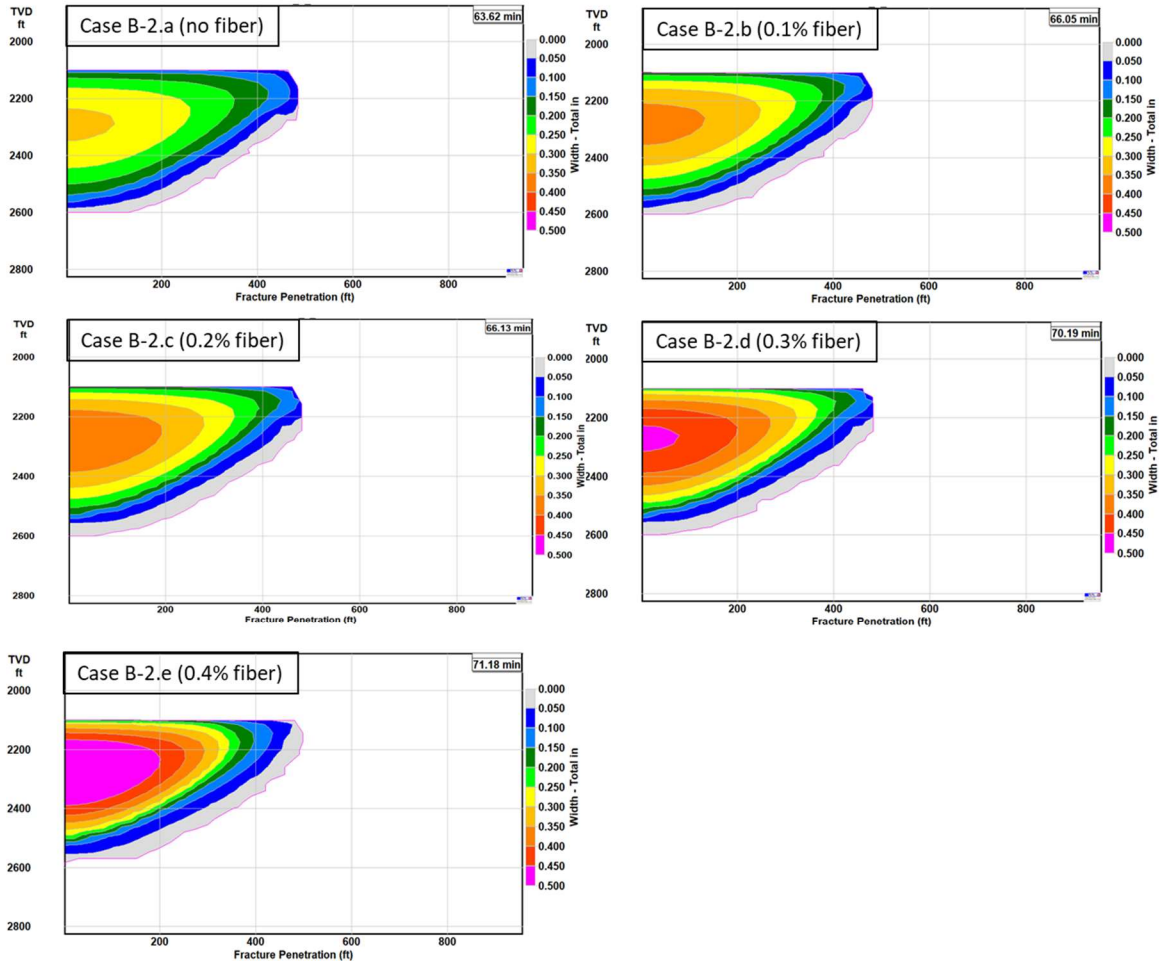

Figure 95. Fracture widths at the end of pumping for the fracture perforated between 2500 to 2505 MD (Appendix B-2 (a to e), with 7.5 cp viscosity at the reservoir condition).

The next three figures (**Figs. 96** to **98**) compare the proppant transport with increase in the fiber concentration. It should be noted that all three graph comparisons show better results. The average proppant concentration increased significantly. The conductivity and proppant concentrations are the most significant with 0.2 wt. % fiber. Overall the results indicate

that the proppant transport is better without changing the fracture geometry for the first

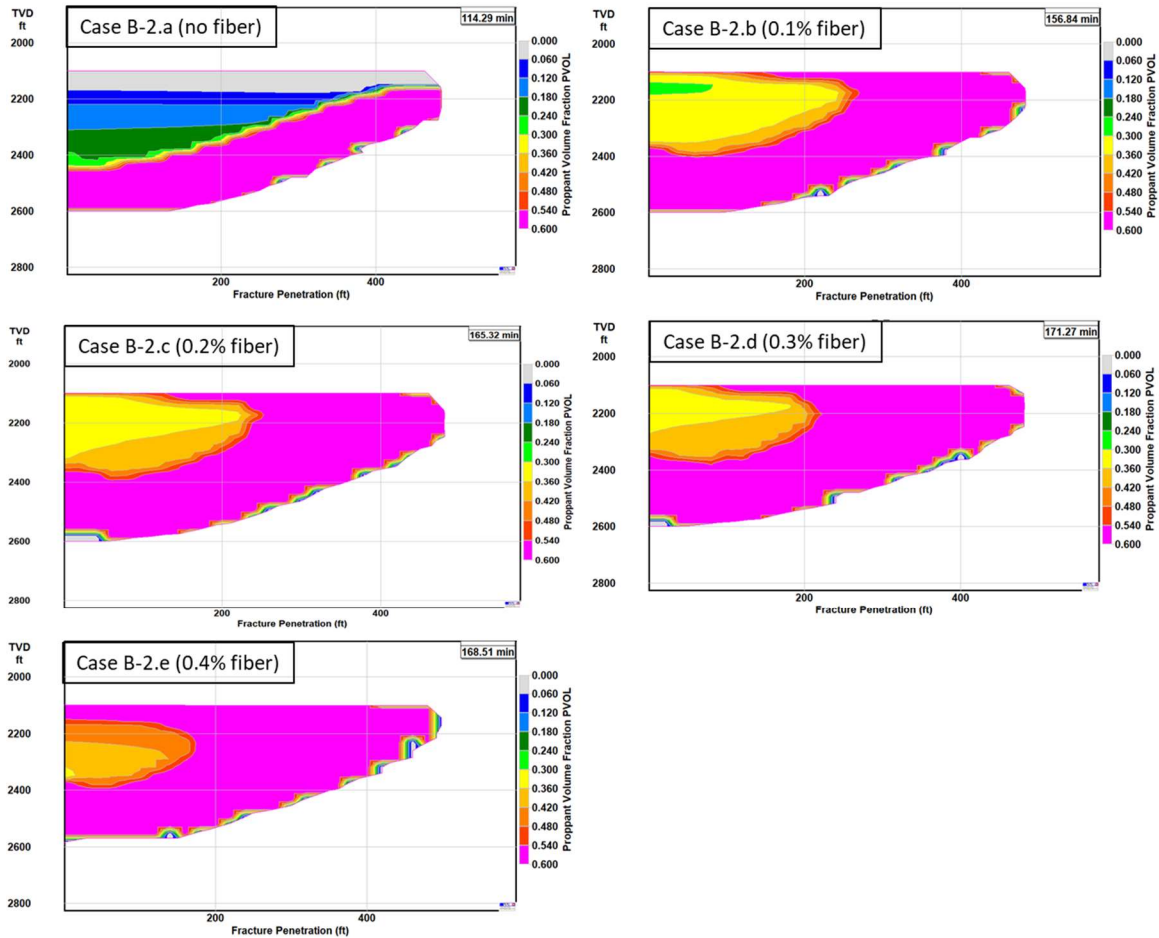fracture near the hill of the horizontal well.

Figure 96. Proppant volume fraction after fracture closure (Appendix B-2 (a to e), with 7.5 cp viscosity at the reservoir condition).

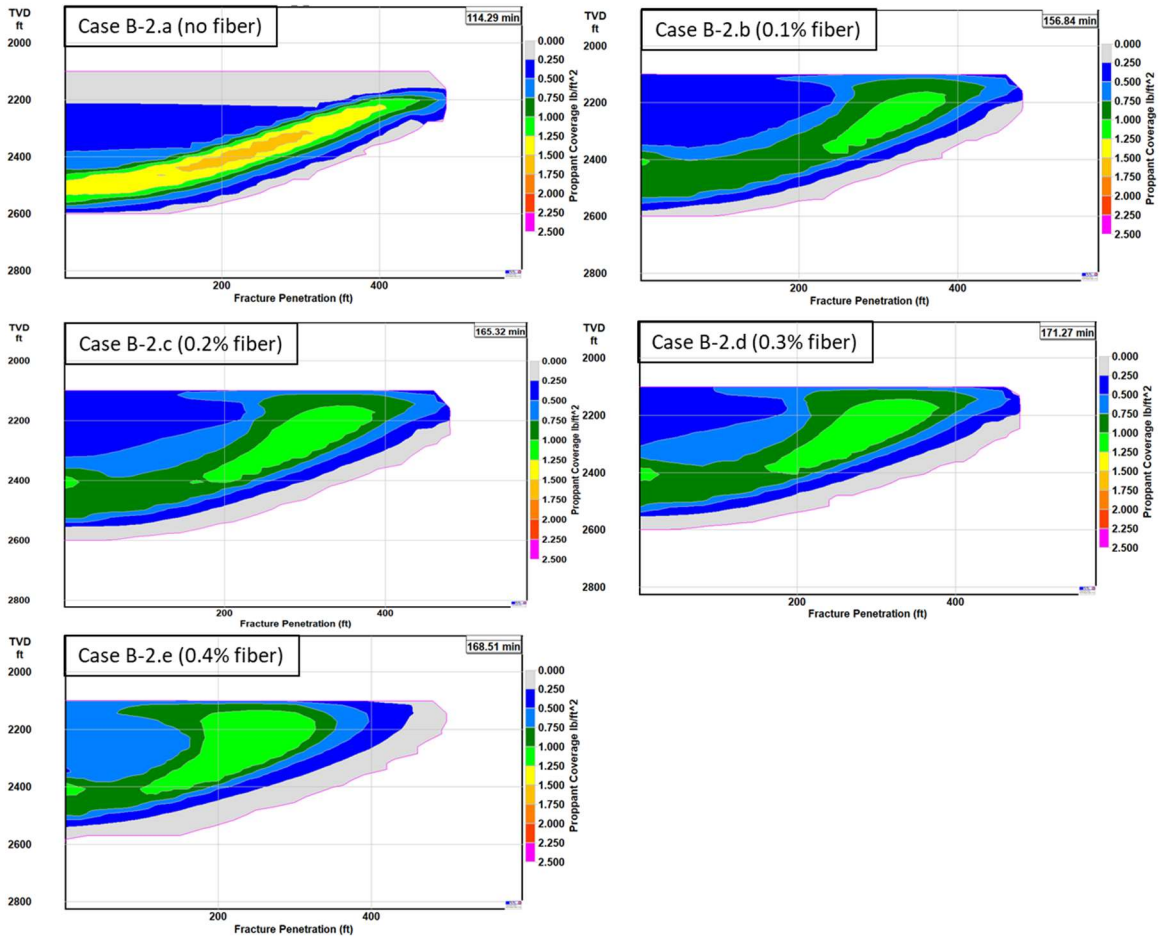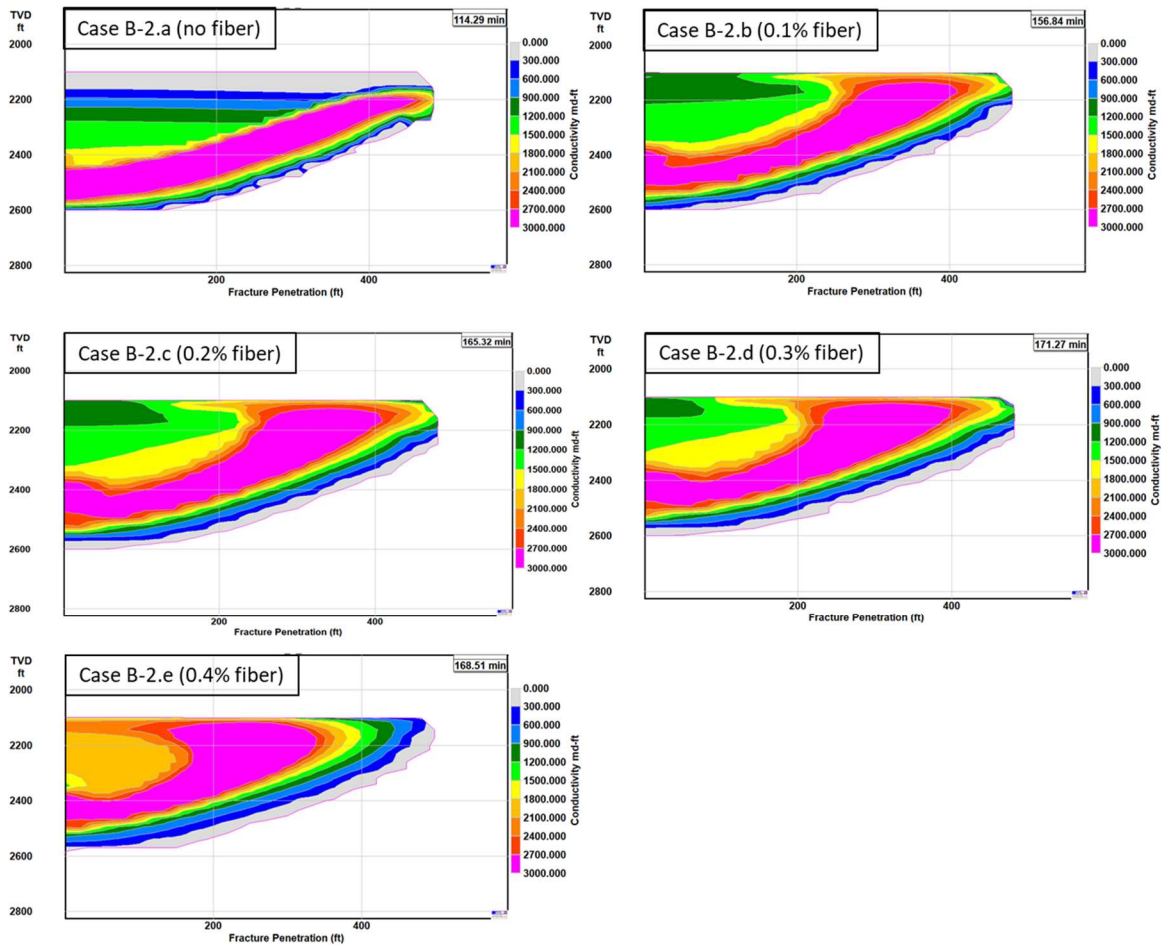Appendix B-2. perf between 2500 ~ 2505 MD with 6 shots/ft

Figure 97. Proppant coverage after fracture closure (Appendix B-2 (a to e), with 7.5 cp viscosity at the reservoir condition).

Figure 98. Proppant fracture conductivity after fracture closure (Appendix B-2 (a to e), with 7.5 cp viscosity at the reservoir condition).

Fig. 99 shows the fracture geometry comparison of the fracture at the middle. As the fibers are added, the fracture width increases from approximately 0.25 inch to 0.35 inches at the center. The fracture half-length decreased slightly from 400 ft. The fracture height stayed constant until more fibers are added, where the bottom limit broke off at 2600 ft for the case with 0.4 wt. % fiber.
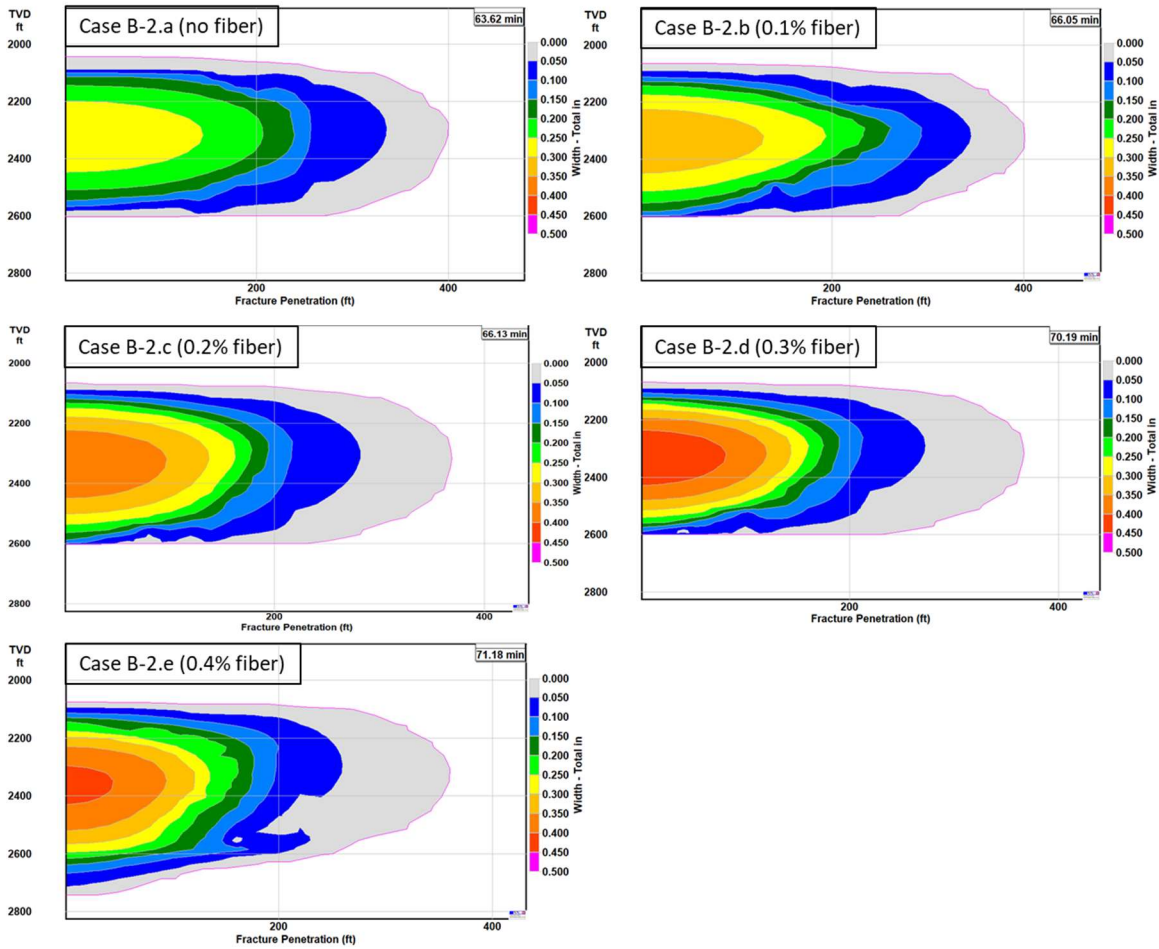
Figure 99. Fracture widths at the end of pumping for the fracture perforated between 2550 to 2555 MD (Appendix B-2 (a to e), with 7.5 cp viscosity at the reservoir condition).

The next three figures (**Figs. 100** to **102**) compare the proppant transport with increase in the fiber concentration. The increase in fiber concentration lead to decrease in average proppant concentration and average conductivity. The proppant coverage figure shows that the proppant does not travel as far with fibers compare to the base case without the presence of fibers. Although the average fracture width is wider with the case with fibers at the center of the fracture geometry, the width gets narrow at the edge due to the pressure

interference from the two fractures that sandwich the middle fracture as the fiber

concentration increases. This leads to lower conductivity and proppant concentration for

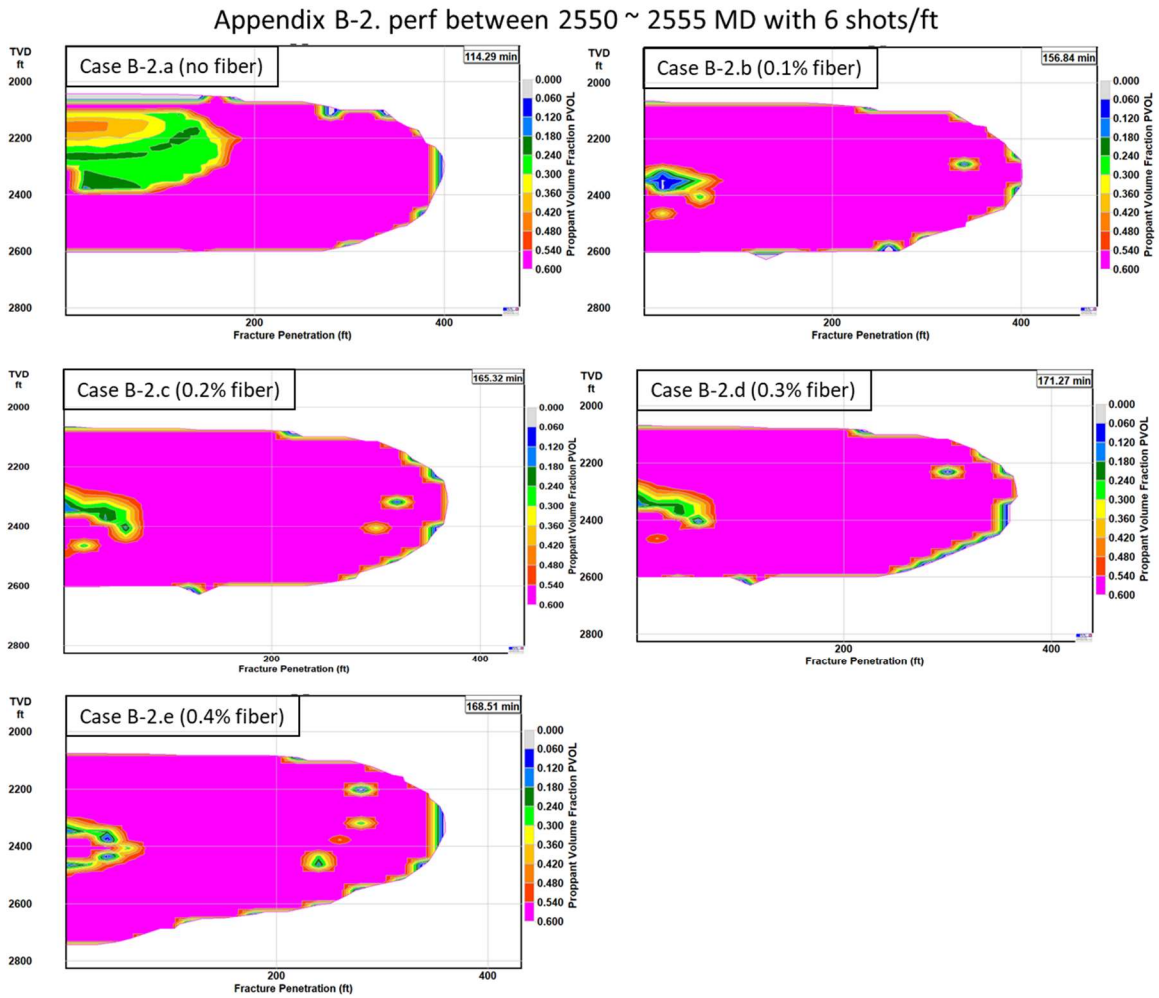the case with more fibers for the middle fracture.

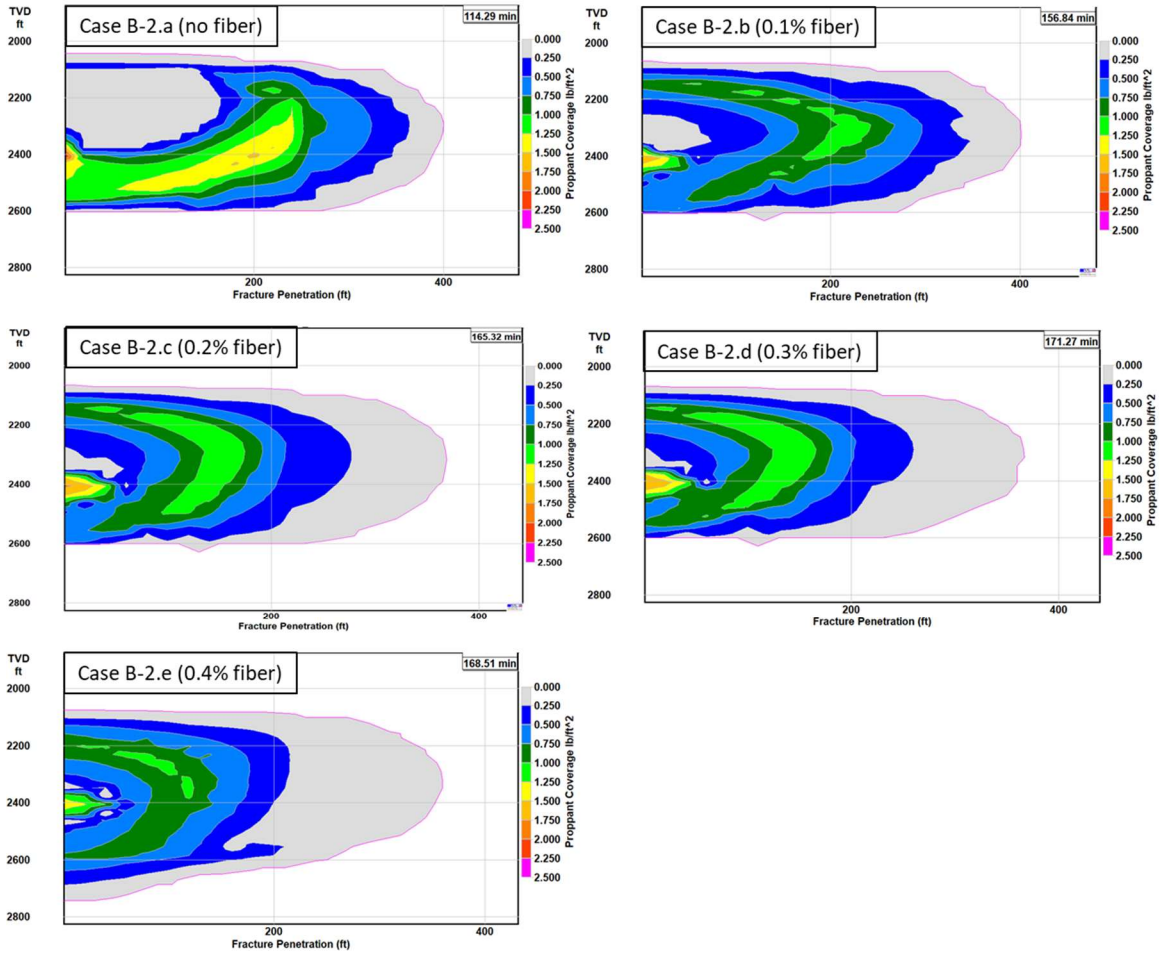**Figure 100. Proppant volume fraction after fracture closure (Appendix B-2 (a to e), with 7.5 cp viscosity at the reservoir condition).**

Figure 101. Proppant coverage after fracture closure (Appendix B-2 (a to e), with 7.5 cp viscosity at the reservoir condition).
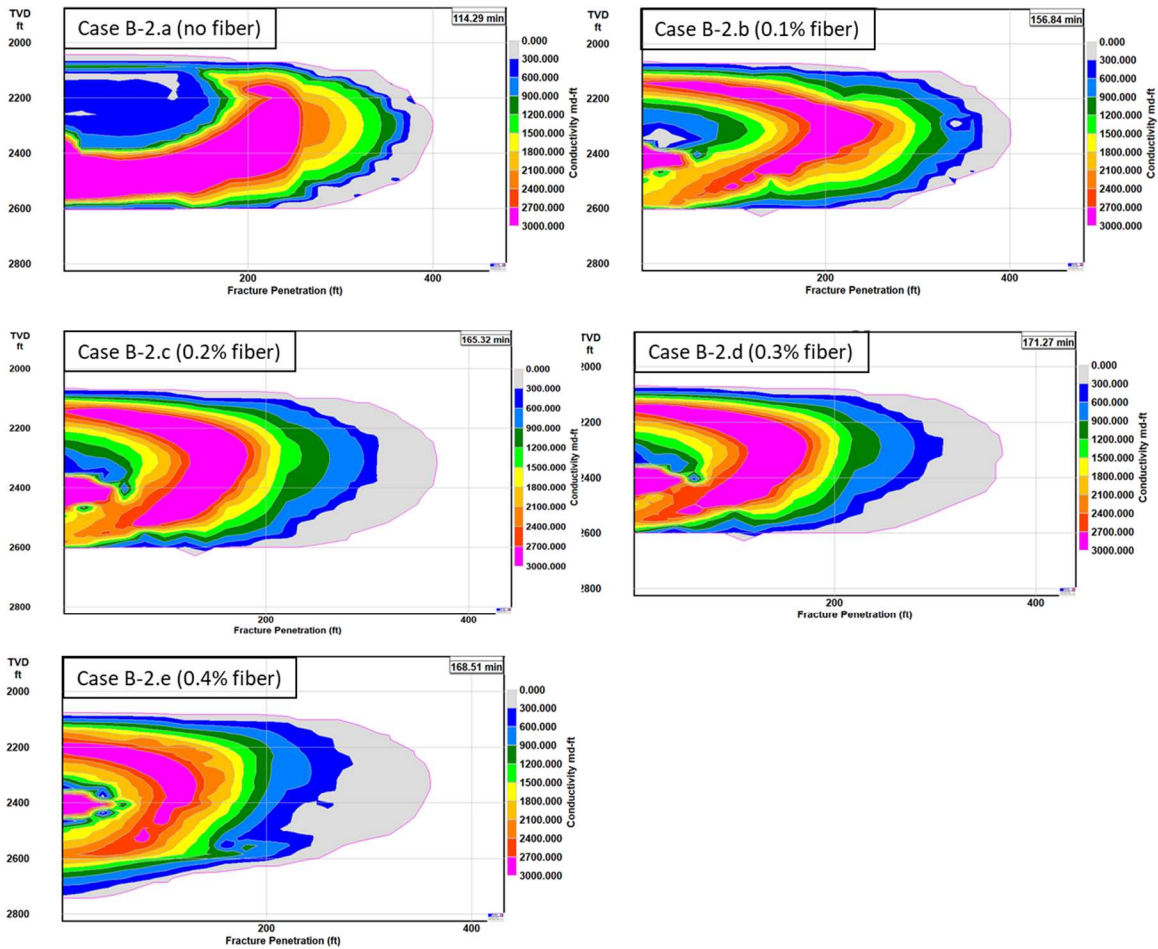
Figure 102. Proppant fracture conductivity after fracture closure (Appendix B-2 (a to e), with 7.5 cp viscosity at the reservoir condition).

The final comparison is done on the perforation between 2600 and 2605 ft. MD, which is located near the toe of the fracture. As it can be seen from **Fig. 103**, the change in the fracture half-length is not significant, but the average width increased from approximately 0.25 to 0.5 inches, which is about 50 % increase.
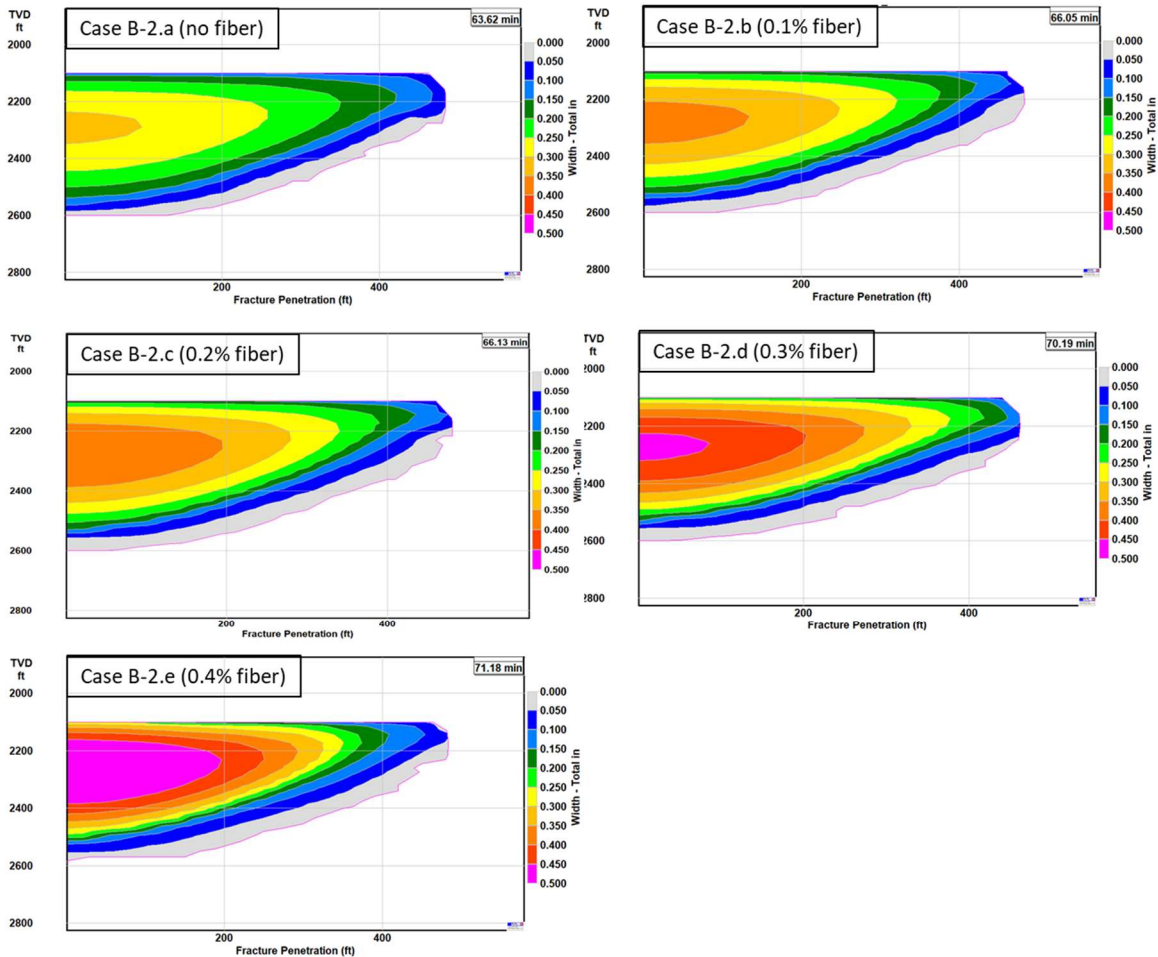
Figure 103. Fracture widths at the end of pumping for the fracture perforated between 2600 to 2605 MD (Appendix B-2 (a to e), with 7.5 cp viscosity at the reservoir condition).

The next three figures (**Figs. 104, 105, 106**) compare the proppant transport with increase in the fiber concentration for the fracture located near the toe of the fracture. As more fiber is added, the average proppant concentration and conductivity are increased significantly. The proppant coverage graph shows the addition of fiber lead to even coverage of proppants. The average conductivity also indicates that addition of fiber increases the proppant conductivity. The proppant volume fraction graph also shows

similar trend. It should be noted that the use of small fiber concentration, 0.1 wt. %, had the
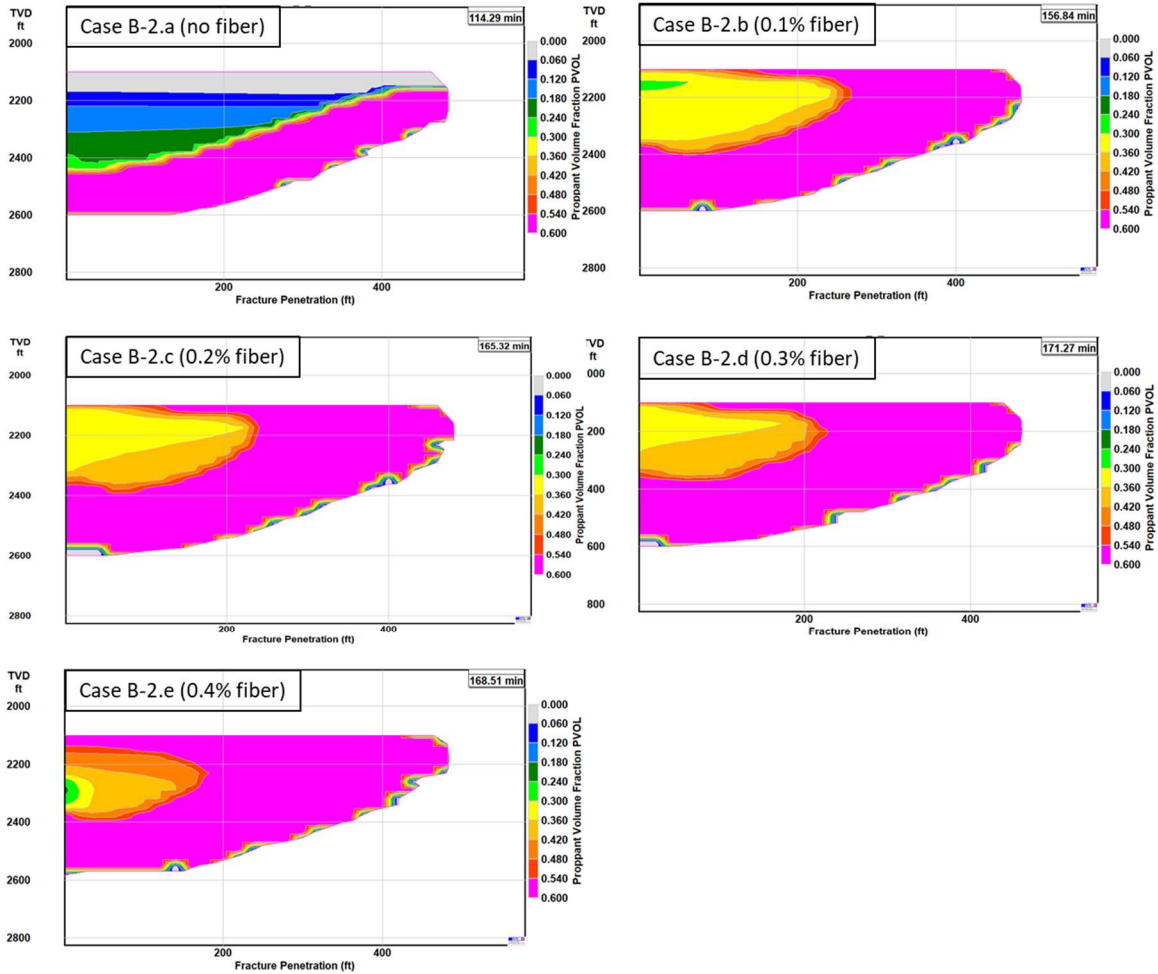
most affect in proppant transport.

Figure 104. Proppant volume fraction after fracture closure for the fracture perforated between 2600 to 2605 MD (Appendix B-2 (a to e), with 7.5 cp viscosity at the reservoir condition).
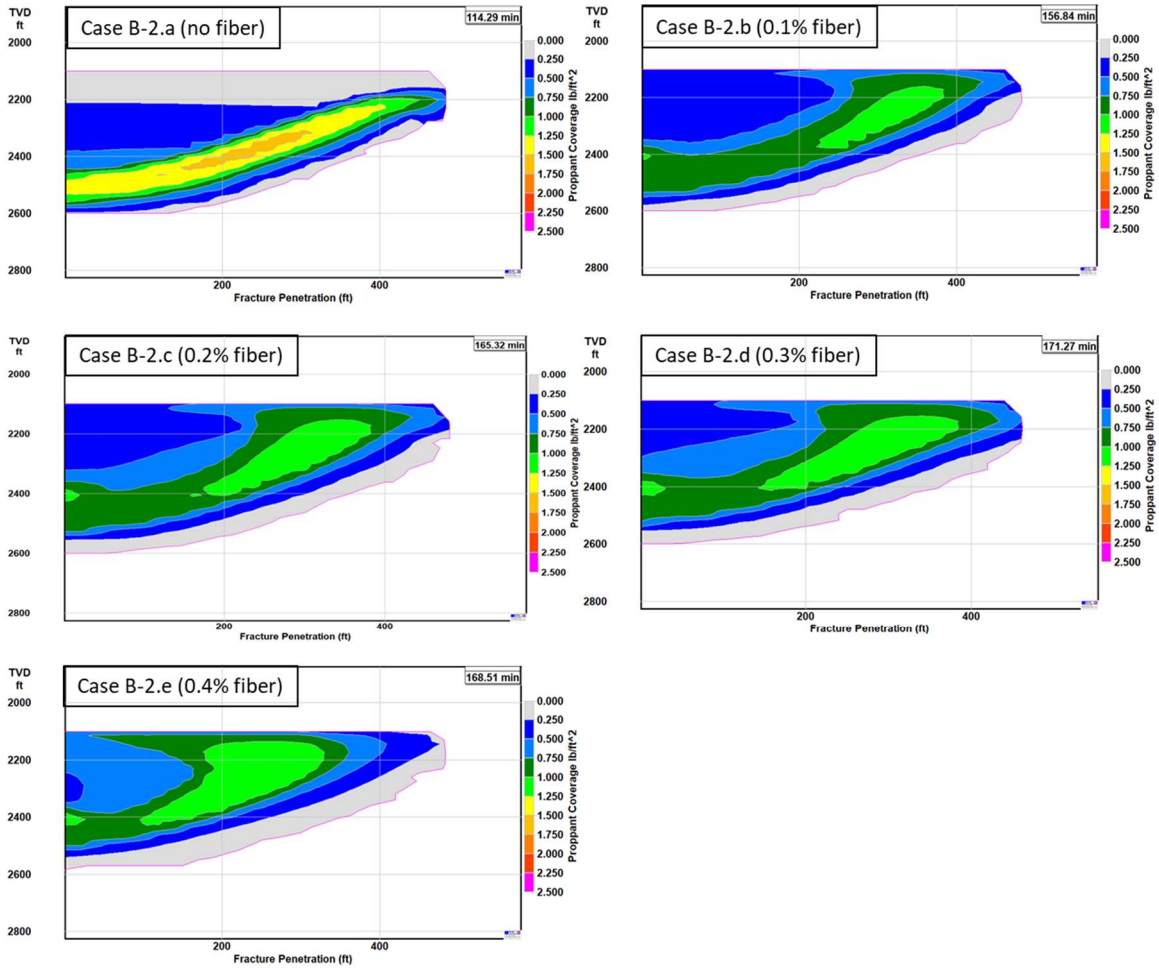
Figure 105. Proppant coverage after fracture closure for the fracture perforated between 2600 to 2605 MD (Appendix B-2 (a to e), with 7.5 cp viscosity at the reservoir condition).
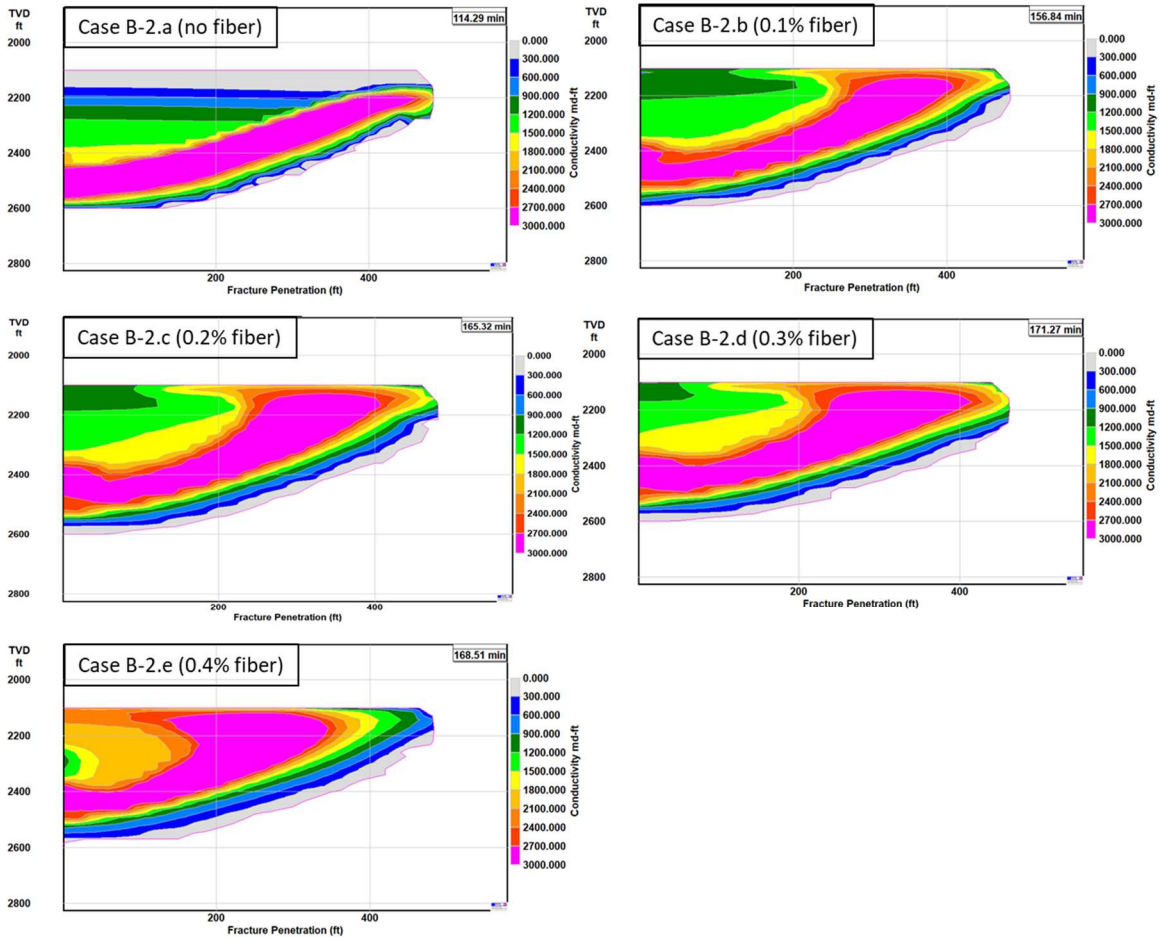
Figure 106. Proppant fracture conductivity after fracture closure for the fracture perforated between 2600 to 2605 MD (Appendix B-2 (a to e), with 7.5 cp viscosity at the reservoir condition).

The appendix B-3 model to simulate and compare is a single horizontal well (unconventional reservoir) with three vertical fractures with the following details below. The conditions are the same as Case 3 except for three fractures are induced from one cluster. The injection volume and injection rate are set to three times larger than Case 3 since three fractures simultaneously propagate for appendix B-3.

Appendix B-3: Three vertical fracture propagations from a horizontal well (unconventional reservoir)

- **Reservoir:**
  Pay depth: 2150-2450ft, Initial reservoir pressure: 1500psi, Current reservoir pressure: 1000psi, Bottomhole Flowing Pressure: 500psi, Sand formation, Porosity: 0.15, permeability: 5 md, rock compressibility: 1.7×10^{-6} 1/psi, oil reservoir with 40 API gravity, Bottomhole reservoir temperature: 200°F.
- **Well data:**
  Treatment through tubing, horizontal well, Borehole diameter=8.5";
  Casing: 7" OD, 6.366" ID, 0~2500 ft TVD, Horizontal lateral length: 1100 ft kick-off at 2400 ft TVD
  Tubing: 4.5 OD, 4.052" ID, 0~2400ft TVD;
  Fracture initiation: 2500 – 2505 ft with 6 shots/ft; 2700 – 2705 ft with 6 shots/ft; 2900 – 2905 with 6 shots/ft
- **Geologic Layer Data:**
  Layer I: 1710 psi at 1900 ft TVD and 1890 psi at 2100 ft TVD with 0.9 psi/ft overburden;
  Layer II: 1470 psi at 2100 ft TVD and 1820 psi at 2600 ft TVD with 0.7 psi/ft overburden;
  Layer III: 2340 psi at 2600 ft TVD with 0.9 psi/ft overburden;
  Young's modulus: 3×10^6 psi, Poisson's ratio: 0.2, fracture toughness: 2000 $psi\sqrt{in}$.
- **Slurry Data:**
  Fluid Data: Fluid loss coefficient= 0.0005 ft/$\sqrt{min}$, 0.1 wt. % guar, K'= 0.000134, n'= 0.9.
  Proppant data: 40/70 mesh ceramic proppant, density=2.6g/cm^3 (1.57 g/cm^3 as bulk density). Proppant pack porosity: 0.35 without fiber and 0.4 with fiber;
  Pump schedule: pad= 60,000 gal with 90 BPM (pump time 15.9 min), slurry injection 180,000 gal with 90 BPM (1 PPG proppant concentration, pump time 47.6

min.)

The appendix B-3 results are illustrated below in **Figs. 108** to **119.** The total of 4

different fiber concentrations (0.4, 0.3, 0.2, and 0.1 wt. %) are compared to the fluids

composition and slurry data shown above without the presence of fibers. Each of the three

fractures is compared separately with respect to the fiber concentration. **Fig. 107** is shown

as the bottom hole pressure for the base case. The bottom hole injection pressure for the

three fracture propagations is slightly higher than the single fracture propagation (Case 3)

due to the stress shadow effect, although the injection rate and volume are increased to
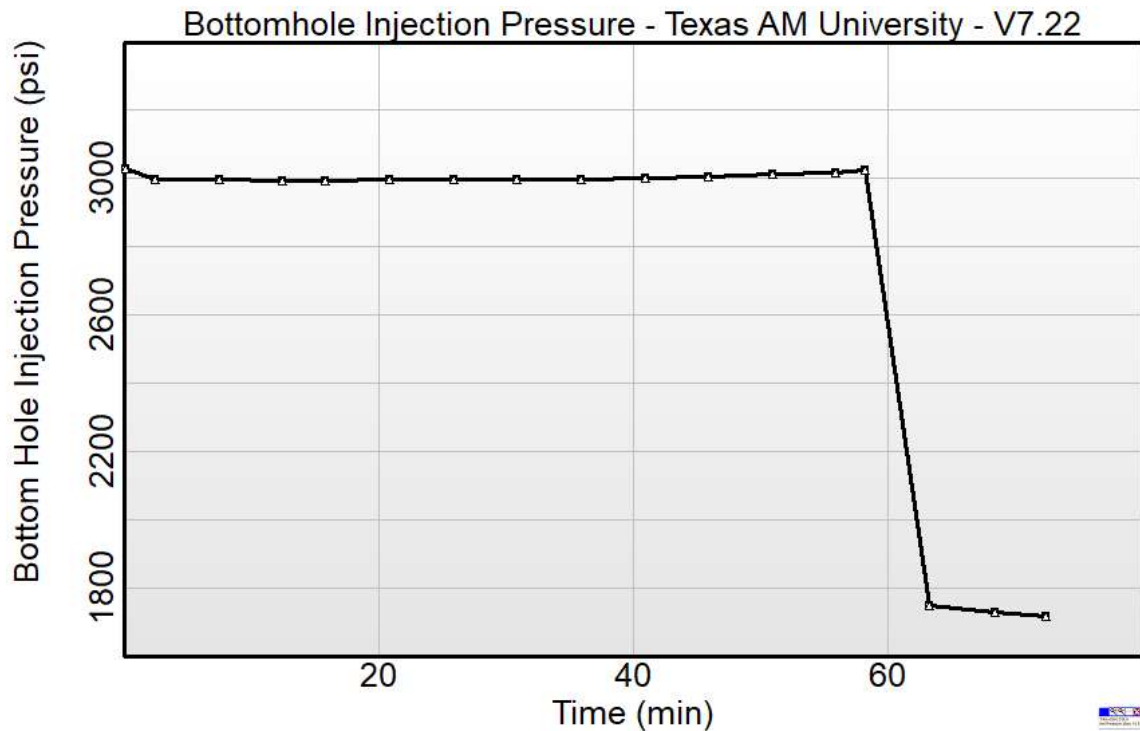
three times.

Figure 107 Bottomhole injection pressure for the Appendix B-3.

Fig. 108 shows the fracture geometry comparison of the fracture perforated between 2500 to 2505 ft MD, fracture closest to the heel of the well. As the fiber is included in the fluid, the average widths increased from 0.09 inch to 0.14 inch when 0.4 weight % fiber is used, which is 56% increase. The fracture length decreased from 768 ft to 621 ft as well. The fracture height did not change significantly; the maximum height decreased from 483 to 459 ft with the presence of fiber. The proppant settles at the fracture bottom, which prevents fracture from propagating downwards. It causes a longer fracture if no fiber is included.

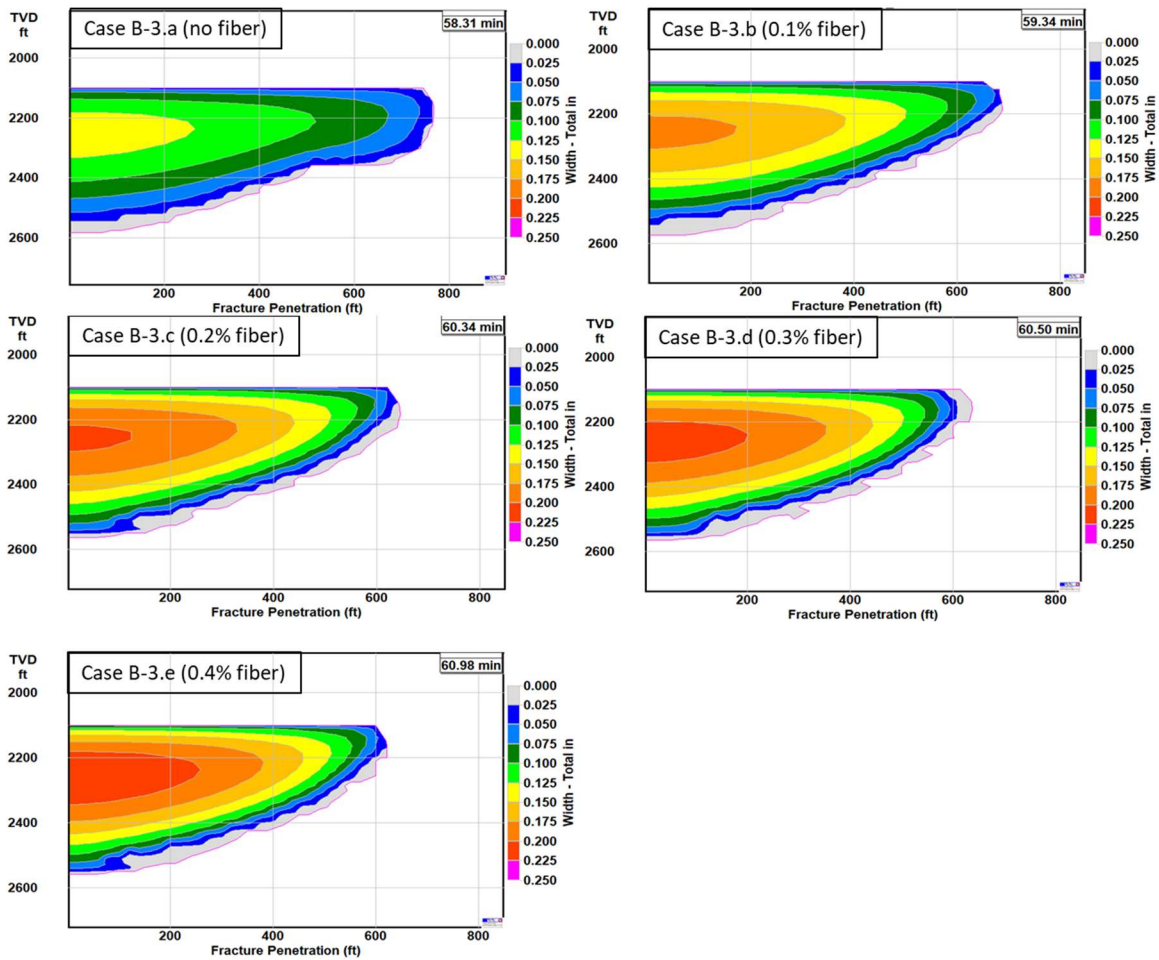Appendix B-3. perf between 2500 ~ 2505 MD with 6 shots/ft

Figure 108. Fracture widths at the end of pumping for the fracture perforated between 2500 to 2505 MD (Appendix B-3 (a to e), with 3 cp viscosity at the reservoir condition).

The next three figures (**Figs. 109** to **111**) compare the proppant transport with increase in the fiber concentration. All three graphs show the enhanced proppant placement as the fiber concentration increases. The graph comparison shows that more proppants are dispersed vertically, which leads to increase in the conductivity from 300 md-ft without fiber to 384 md-ft with 0.4 wt. % fibers. However, the proppant coverage around the injection center (2400 ft MD) is slightly smaller compared with the fracture tip. The reason is that for this design, the proppant injection is kept to 1lb/gal. The fluid loss coefficient, 0.0005 ft/$\sqrt{min}$, results in approximately 0.4 fluid efficiency (=frac volume/injected fluid volume). Therefore, the frac fluid traveling around the frac tip has several times higher proppant concentration compared with the fluid entering fracture. The proppant concentration should be increased at the end of injection to increase the proppant coverage around the inlet. Overall, the results indicate that the proppant transport is better with significant decrease in the fracture half-length and significant increase in the average width when fibers are used.
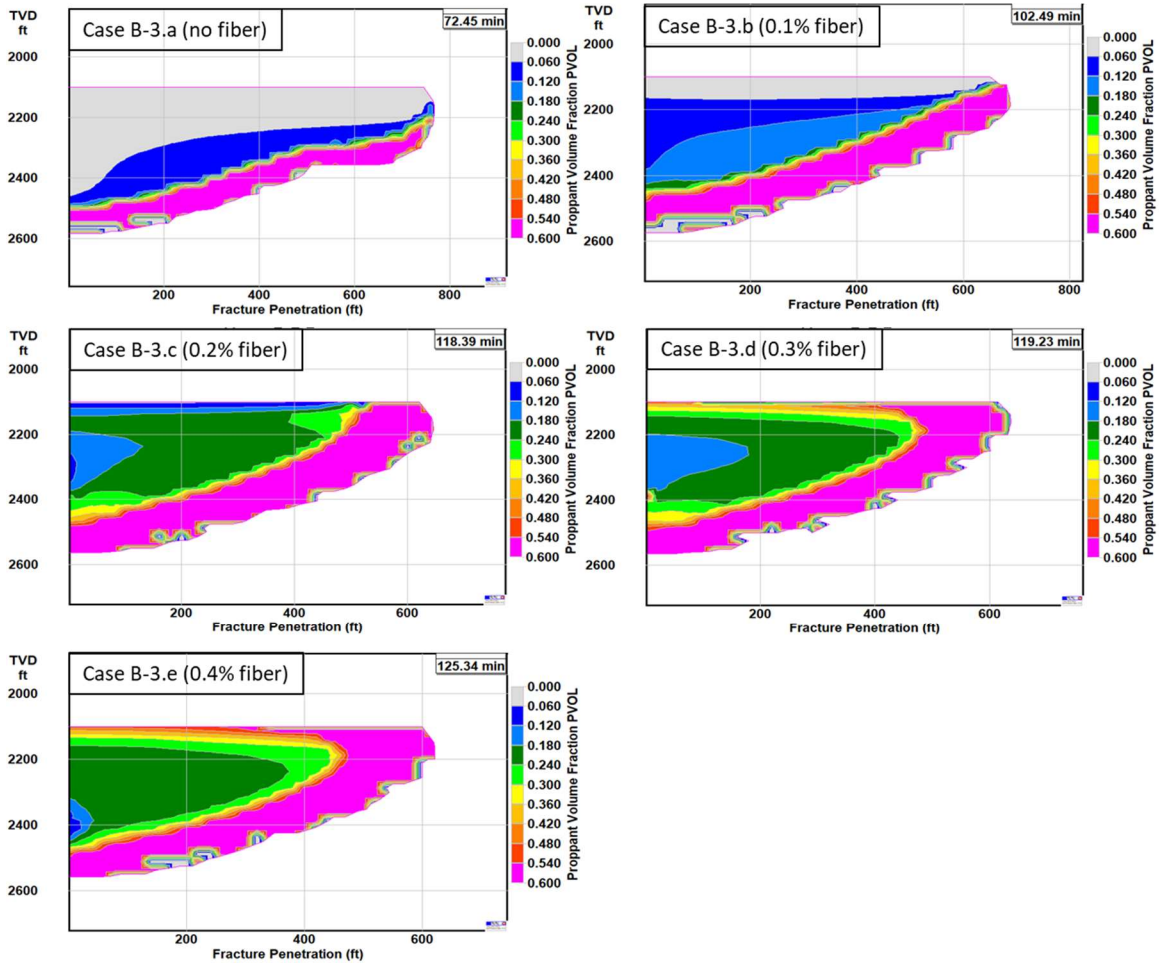
Figure 109. Proppant volume fraction after fracture closure (Appendix B-3 without fiber, with 3 cp viscosity at the reservoir condition).

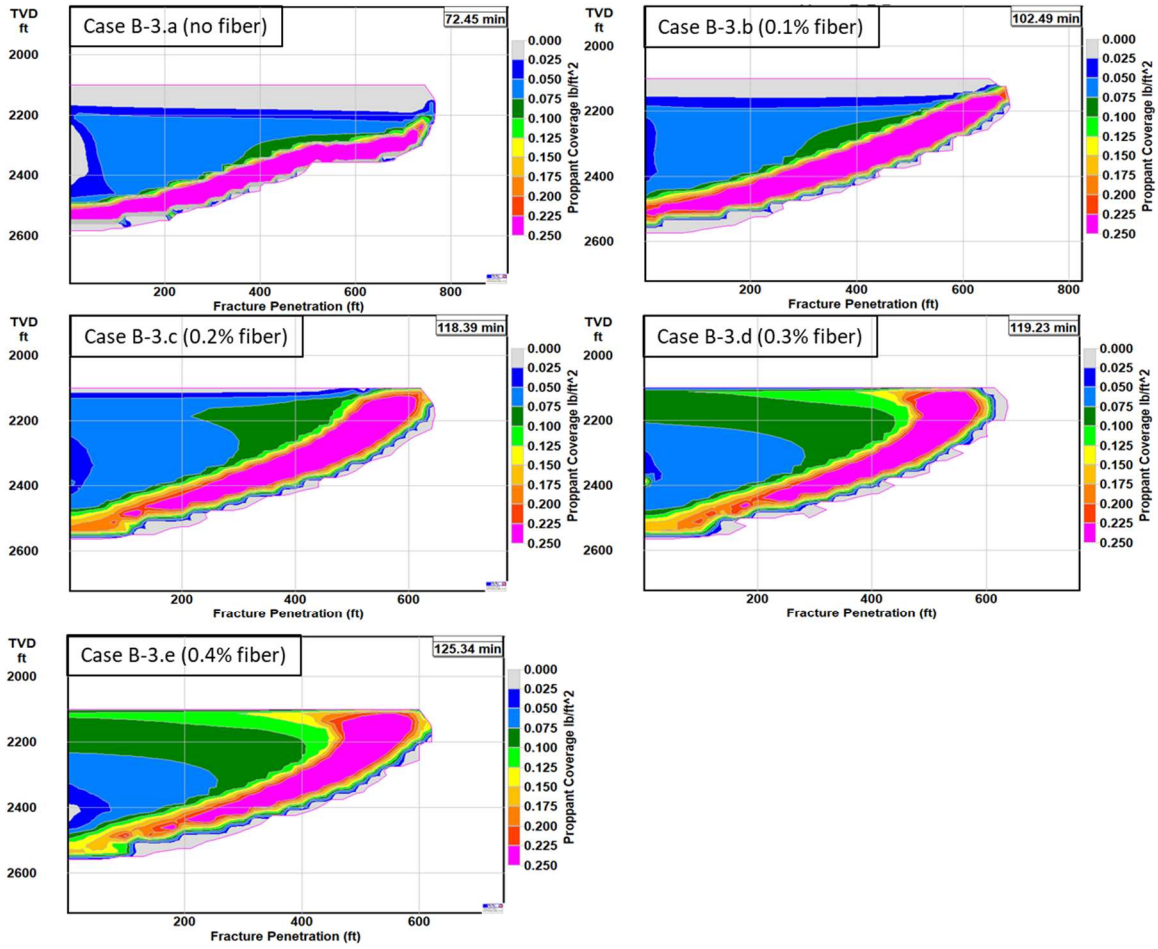**Figure 110. Proppant coverage after fracture closure (Appendix B-3 without fiber, with 3 cp viscosity at the reservoir condition).**
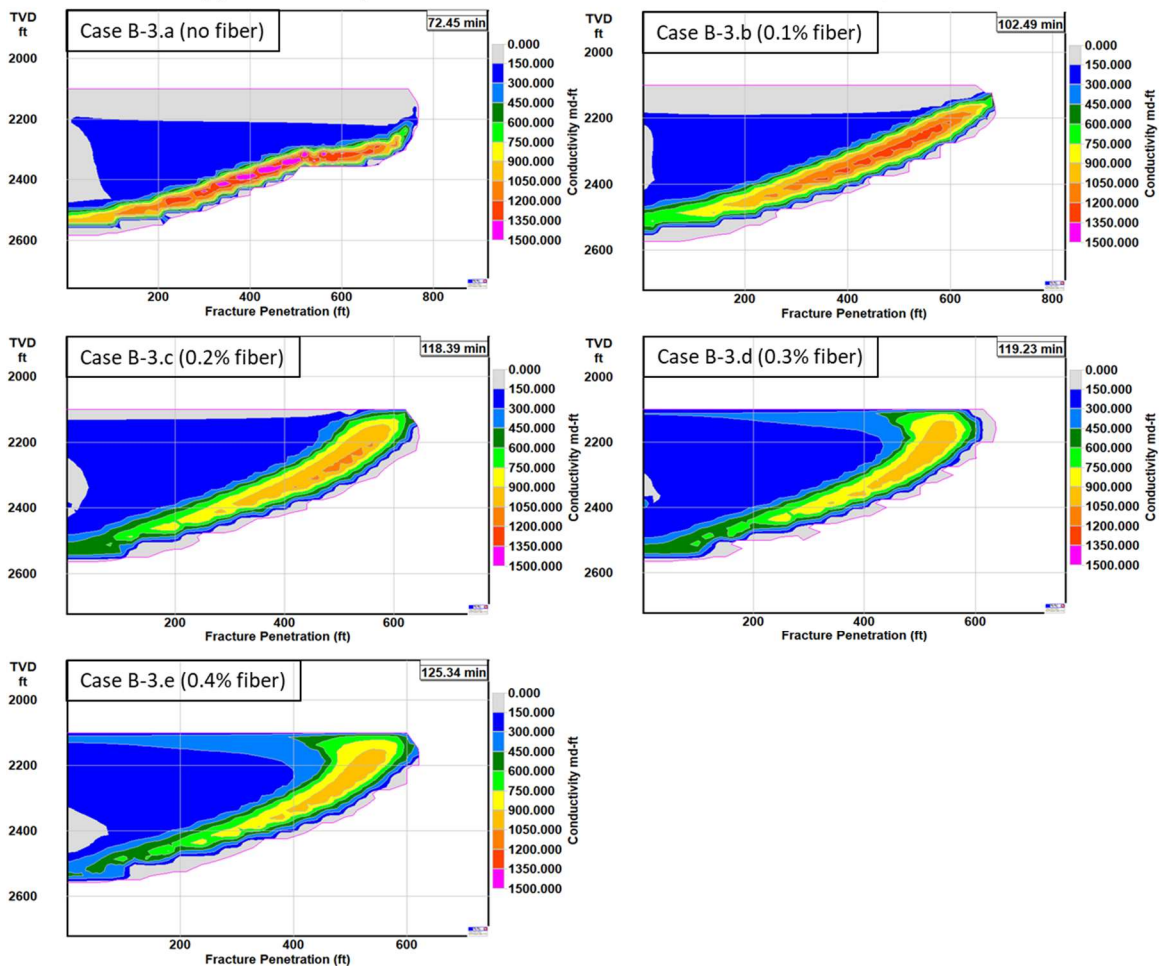
Figure 111. Proppant fracture conductivity after fracture closure (Appendix B-3 without fiber, with 3 cp viscosity at the reservoir condition).

Fig.112 shows the fracture geometry comparison of the fracture at the middle. Due to the stress interference of the multiple parallel fractures, the average width is smaller at 0.08 inch. As the fiber concentration increases, the average width increased to 0.12 inch. The fracture length decreased from 590 ft to 490 ft. The higher fiber concentration leads to the maximum fracture height increase from 500 ft to 556 ft.

The StimPlan can only simulate planar fractures, meaning that it cannot simulate the curved fracture induced by stress shadow effect. Note that if the minimum horizontal in

situ stress is significantly smaller than the maximum horizontal in situ stress, the fractures propagate approximately as planer fractures. However, since the fracturing pressure increase induced by the stress shadow can be simulated accurately, the simulation gives similar results when compared to the published example (Wu and Olson, 2015) on the fracture length and widths. The middle fracture starts breaking the upper stress barrier, therefore, the injection pressure should be slightly reduced for this hydraulic fracture operation.
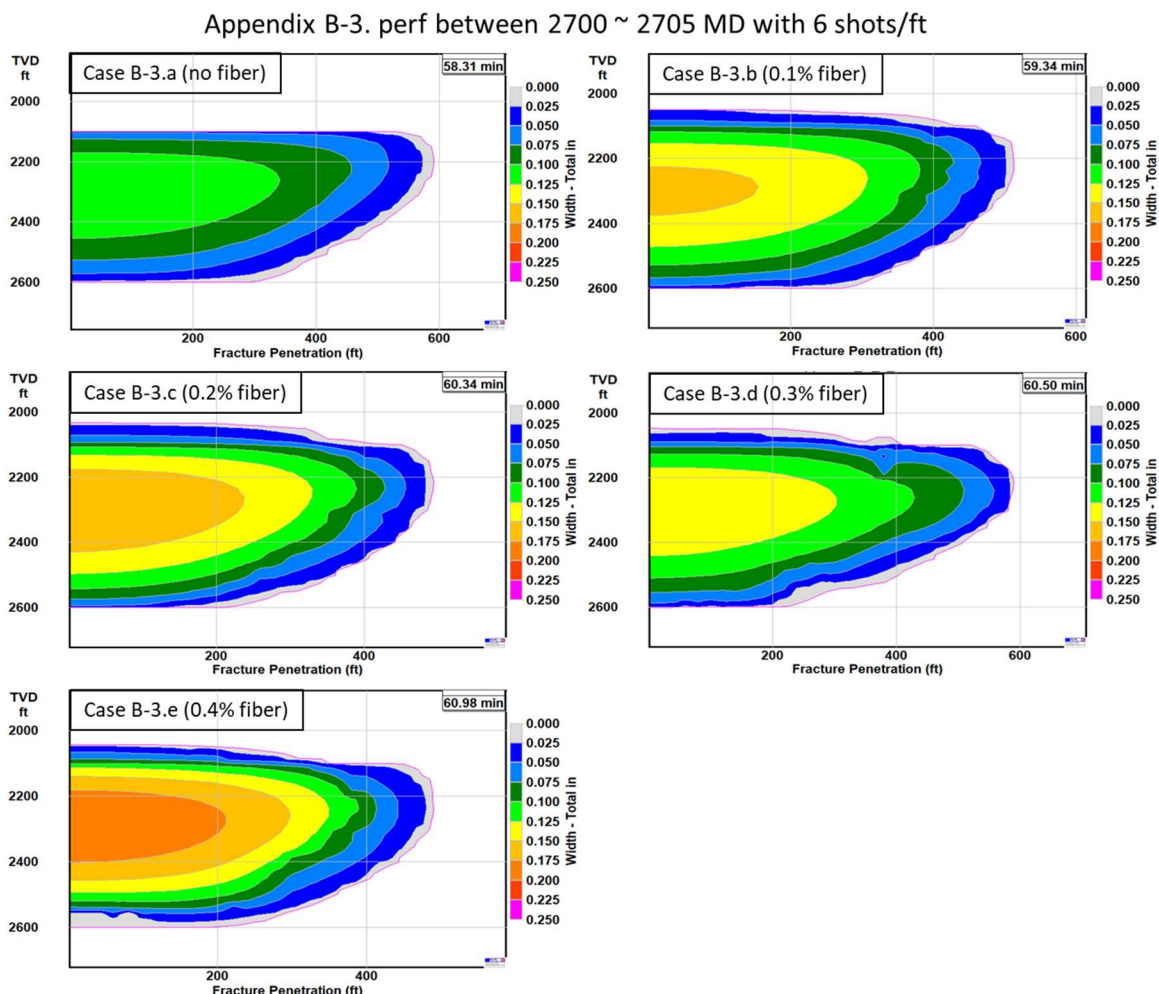

Figure 112. Fracture widths at the end of pumping for the fracture perforated between 2700 to 2705 MD (Appendix B-3 (a to e), with 3 cp viscosity at the reservoir condition).

The next three figures (**Figs. 113** to **115**) compare the proppant volume after proppant settlement. The time of settlement is longer for the case with higher fiber concentration. The increase in fiber concentration leads to even proppant concentration in vertical directions. The center of the injection is around at 2400 ft, where the injection rate is the highest. The dehydration rate of frac fluid due to fluid leak-off is still small within 200 ft radius from 2400 ft MD. Therefore, the proppant concentration is still as low as 1lb/gal within 200 ft around 2400 ft MD, while the proppant concentration is more than 2-4 lb/gal beyond 200ft radius from 2400ft MD due to the frac fluid dehydration (due to leak-off). It causes a higher proppant concentration and coverage beyond 200 ft radius from 2400 ft MD.
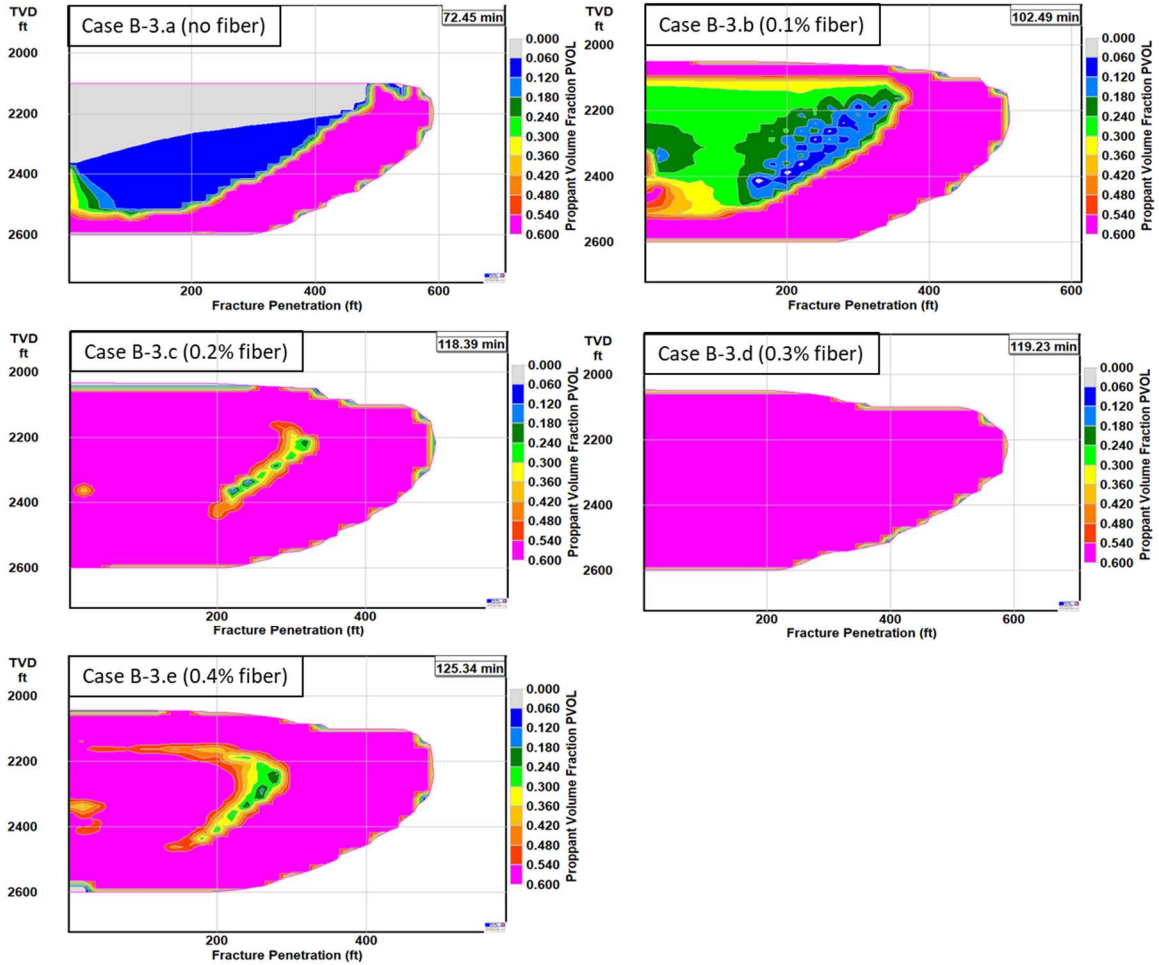
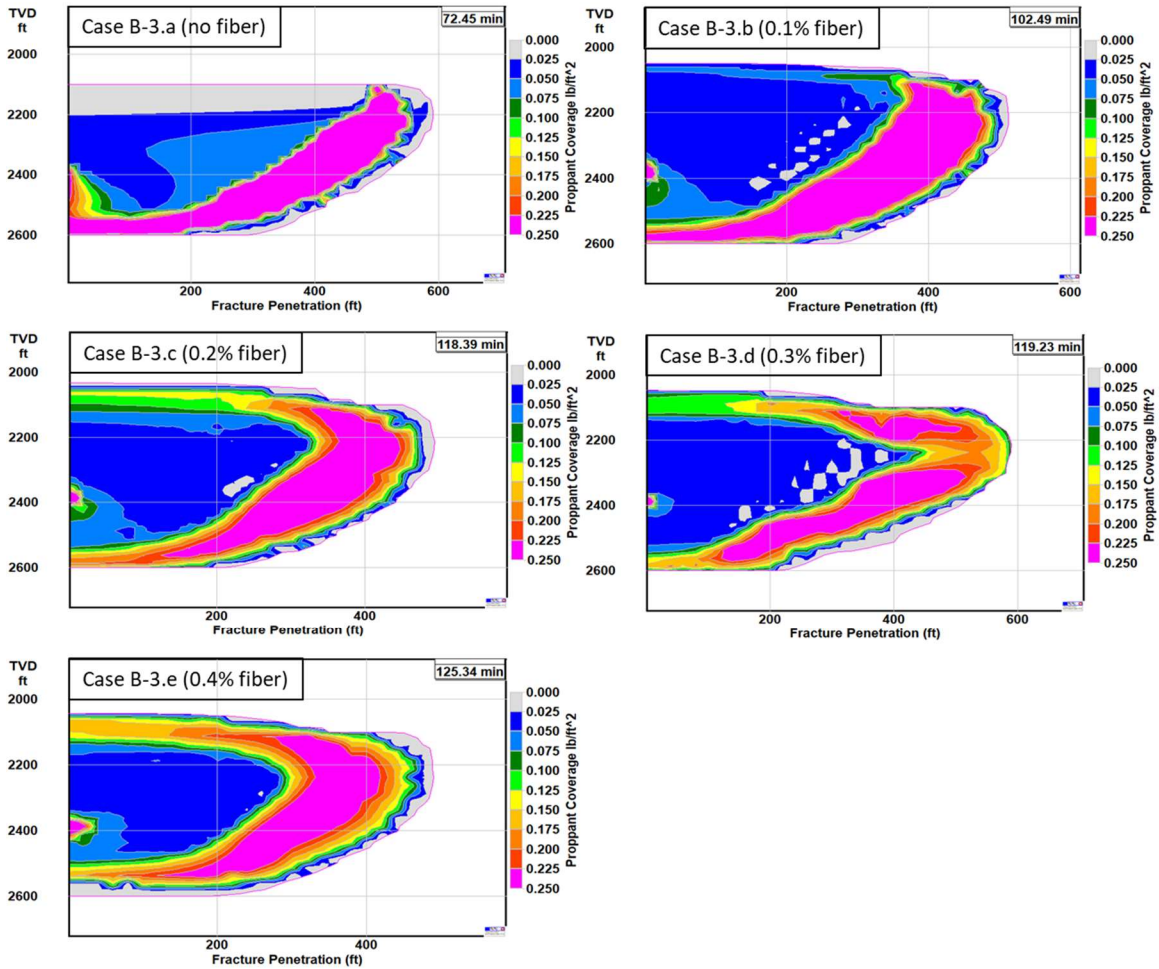**Figure 113. Proppant volume fraction after fracture closure (Appendix B-3 (a to e), with 3 cp viscosity at the reservoir condition).**

Figure 114. Proppant coverage after fracture closure (Appendix B-3 (a to e), with 3 cp viscosity at the reservoir condition).
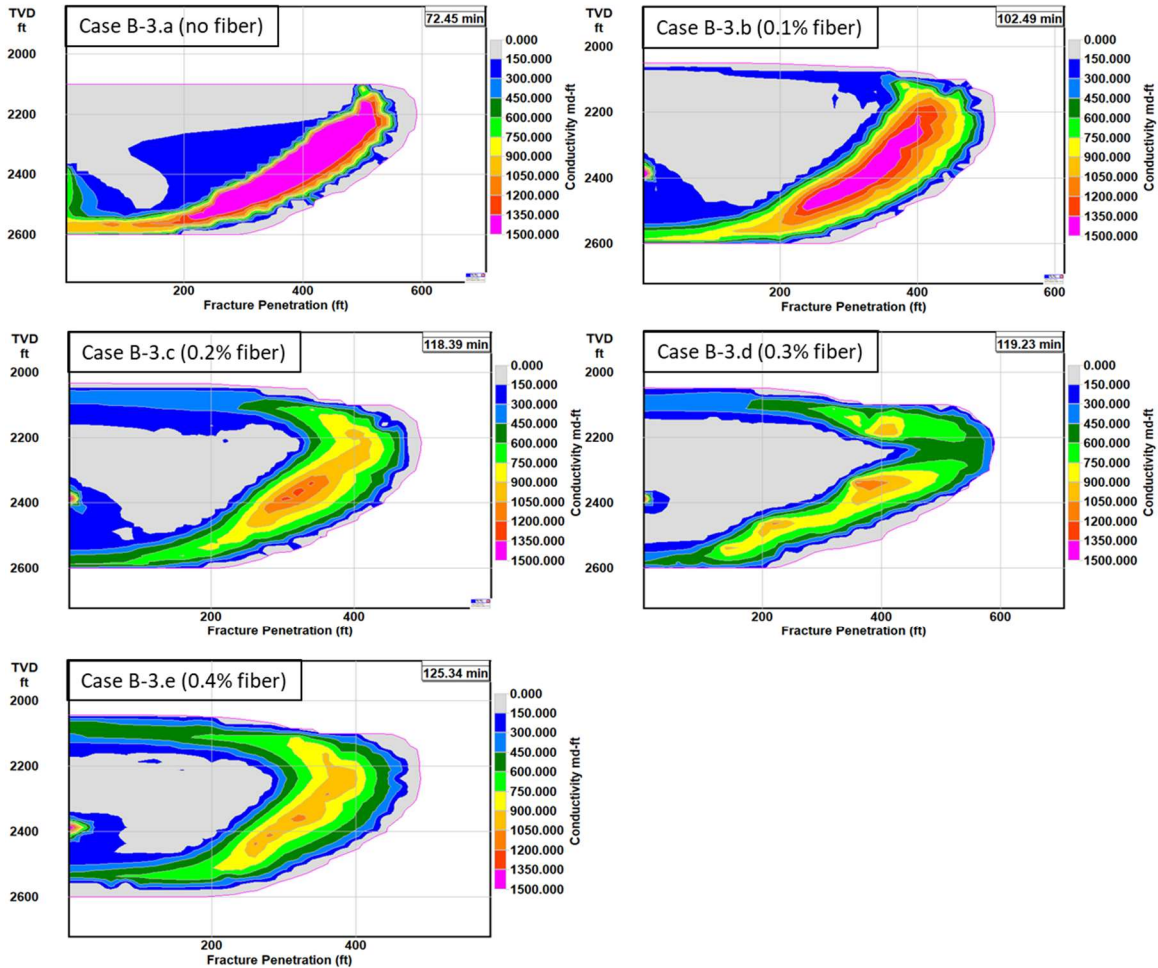
Figure 115. Proppant fracture conductivity after fracture closure (Appendix B-3 (a to e), with 3 cp viscosity at the reservoir condition).

The final comparison is done on the perforation between 2900 and 2905 ft. MD, which is located near the toe of the fracture. As it can be seen from **Fig. 116**, the fracture half-length decreased significantly from 784 ft to 624 ft as the proppant is added, which is about 20 % decrease. The average width increased from 0.09 to 0.14 inches, which is 56 % increase with fibers.
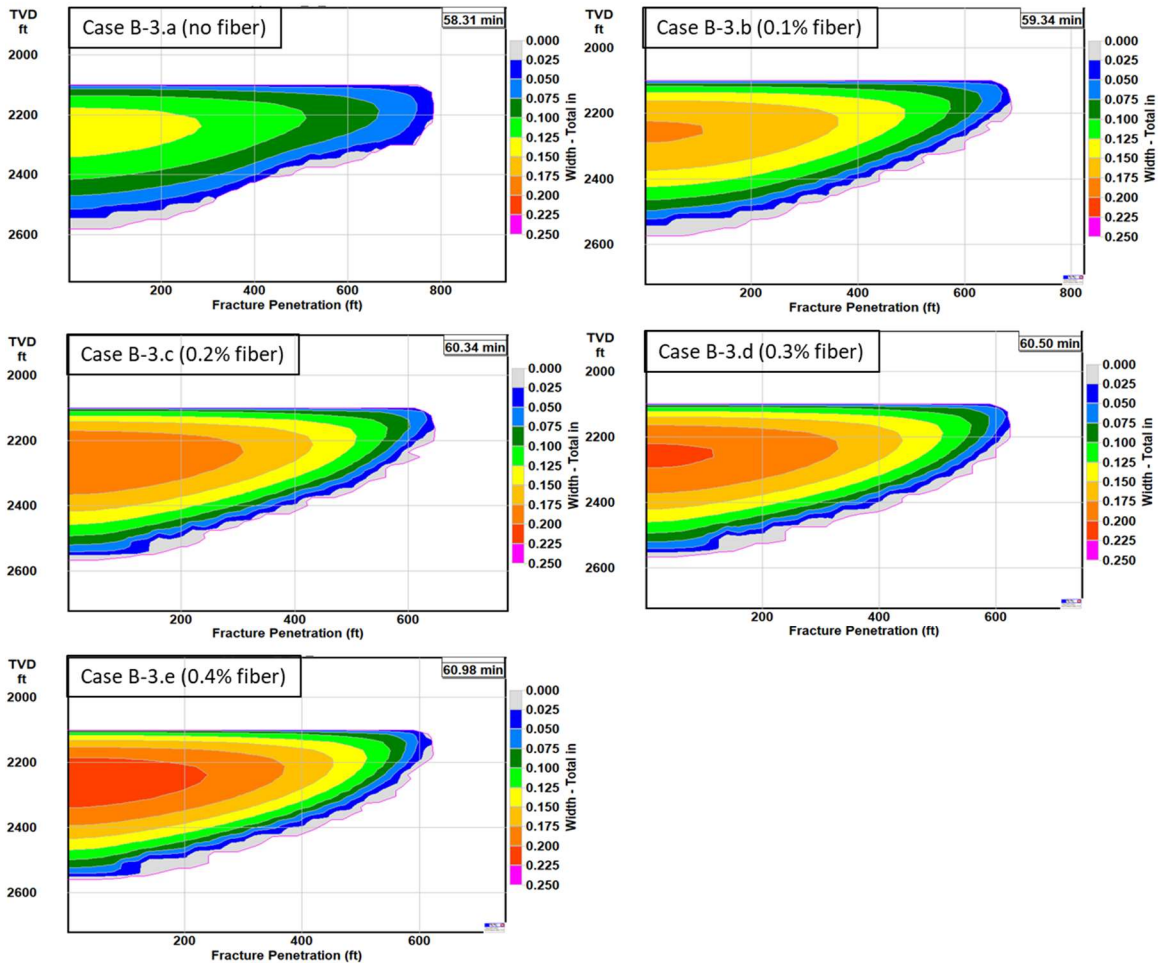
Figure 116. Fracture widths at the end of pumping for the fracture perforated between 2900 to 2905 MD (Appendix B-3 (a to e), with 3 cp viscosity at the reservoir condition).

The next three figures (**Figs.117** to **119**) compare the proppant transport with increase in the fiber concentration for the fracture located near the toe of the fracture. The proppant volume fraction for the case without the fiber shows that all the proppants are settled to the bottom of the fracture as soon as the pump is shut down. This phenomenon changes as soon as fibers are introduced. As more fiber is added, the average conductivity increases significantly, from 229 md-ft to 380 md-ft with fibers which is about 66 %. The average

proppant concentration stayed about the same at $0.1 \frac{lb}{ft^2}$ Again, the proppant coverage

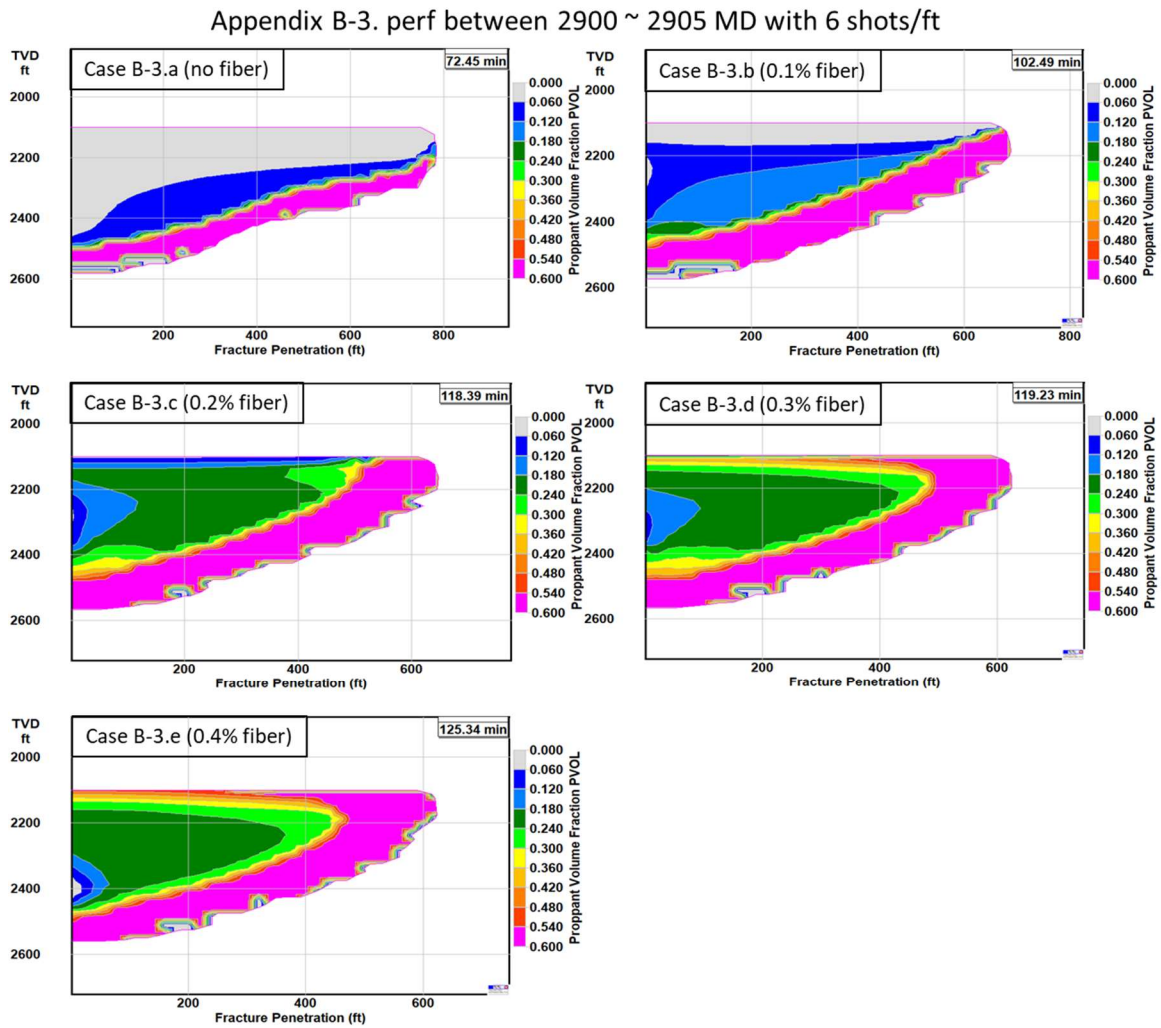within 100 ft from 2400 ft MD is small.

Figure 117. Proppant volume fraction after fracture closure for the fracture perforated between 2900 to 2905 MD (Appendix B-3 (a to e), with 3 cp viscosity at the reservoir condition).
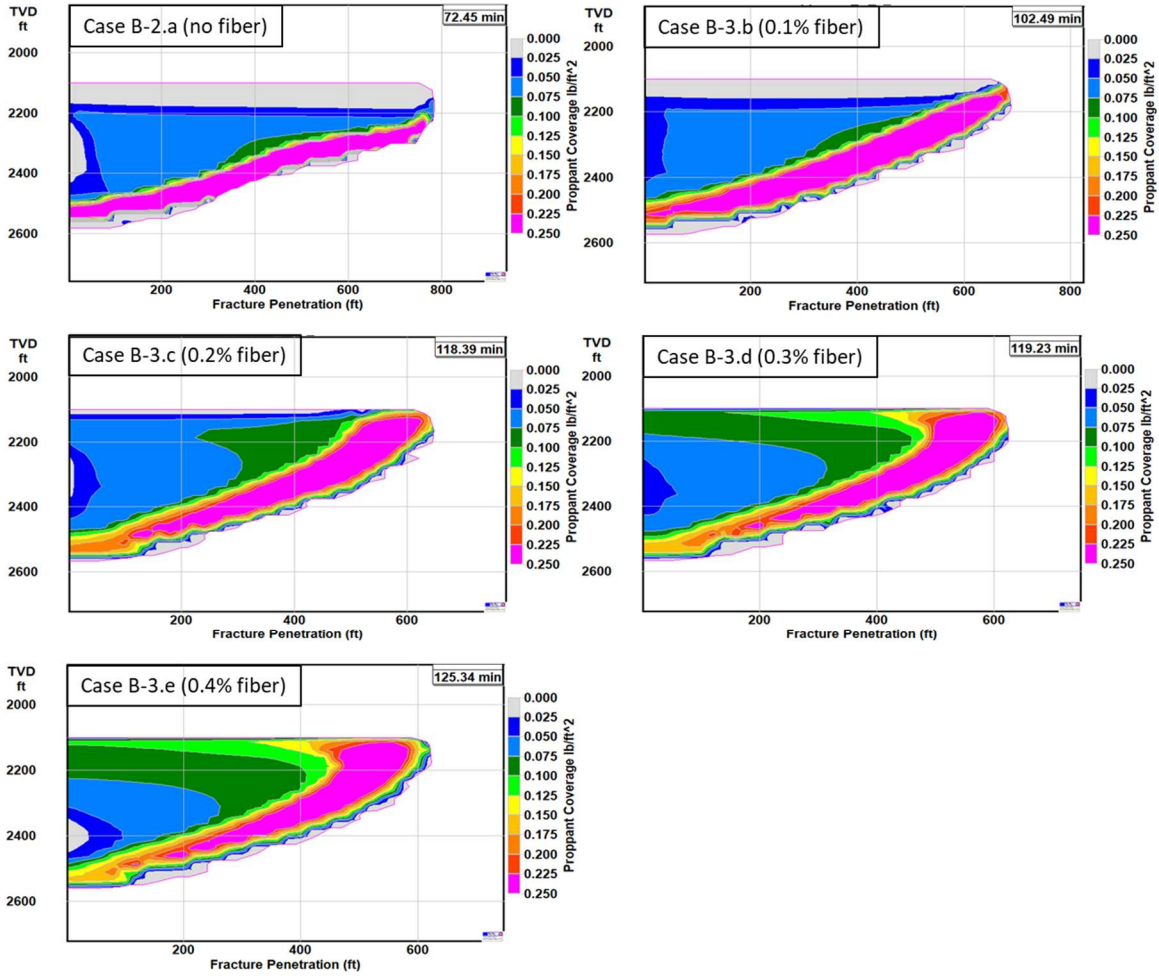
Figure 118. Proppant coverage after fracture closure for the fracture perforated between 2900 to 2905 MD (Appendix B-3 (a to e), with 3 cp viscosity at the reservoir condition).
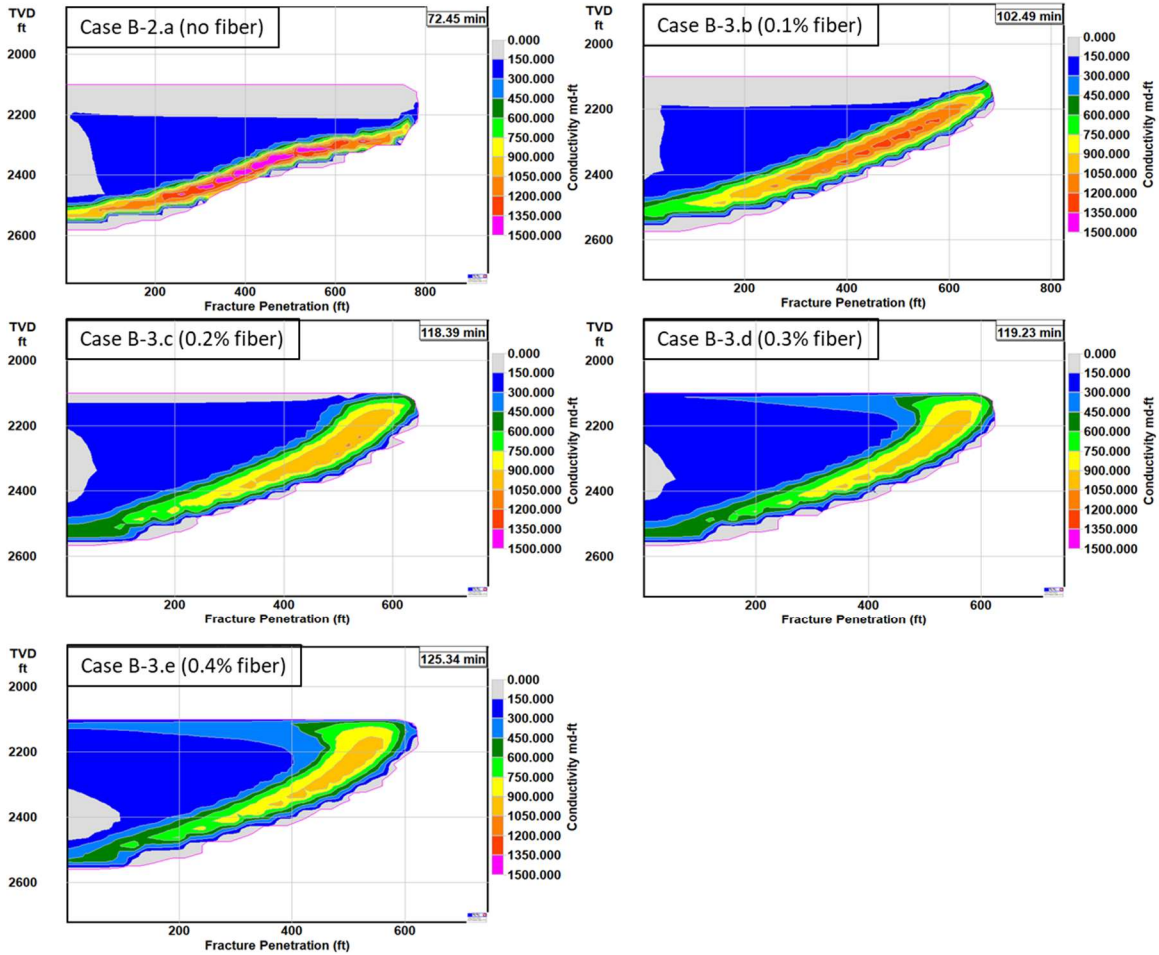
Figure 119. Proppant fracture conductivity after fracture closure for the fracture perforated between 2900 to 2905 MD (Appendix B-3 (a to e), with 3 cp viscosity at the reservoir condition).